4-24-2004

Proceedings of the Thirty-third Annual Biochemical Engineering Symposium

Peter J. Reilly
Iowa State University

Proceedings of the

33rd Annual Biochemical Engineering Symposium

April 24, 2004

Peter J. Reilly
Editor

Department of Chemical Engineering
College of Engineering
Iowa State University, Ames, Iowa

Proceedings of the 33rd Annual Biochemical Engineering Symposium

April 24, 2004

Peter J. Reilly
Editor

Department of Chemical Engineering
College of Engineering
Iowa State University
Ames, Iowa

Preface

This series of Annual Biochemical Engineering Symposia was started in 1971 by Professor Larry E. Erickson of Kansas State University and Peter J. Reilly, then of the University of Nebraska-Lincoln. It is designed for graduate students and occasionally undergraduates and postdoctoral fellows to present the results of their research and directions of their future work to audiences not so familiar as those at their home institutions but not so seemingly intimidating as those at national professional meetings. It also serves as a vehicle for those engaged in similar lines of research to become acquainted with each other and with each other's work. To that end, discussions both during the meeting and at social events attached to it are encouraged. To improve students' skills in writing articles, in general those that follow were first drafted by the students who presented the work reported in them.

The 33 symposia have rotated among the University of Colorado, Boulder; Colorado State University; Iowa State University; Kansas State University; the University of Missouri, Columbia; the University of Nebraska-Lincoln; and the University of Oklahoma. This 33rd Annual Biochemical Engineering Symposium took place on April 24, 2004 at the University of Nebraska-Lincoln with Professor Michael M. Meagher as host.

It should be noted that the 32nd Symposium was held on October 5, 2002. There was no symposium in 2003. Therefore symposium numbering is now in line with the starting year (1971 + 33 symposia = 2004).

Fourteen papers were delivered orally at the symposium and there were a number of posters. These Proceedings present articles from nearly all the oral presentations and from several posters.

Peter J. Reilly
Department of Chemical Engineering
Iowa State University
Ames, IA 50011-2230
Phone: +1-515-294-5968
E-mail: reilly@iastate.edu

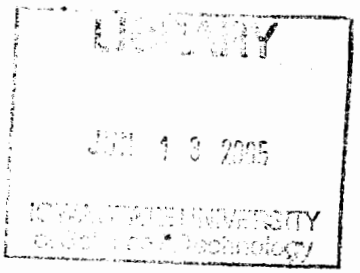

Contents

Novel Pentablock Copolymers as Non-Viral Vectors for Gene Therapy Against Cancer

Ankit Agarwal[1], Robert Unfer[2], and Surya Mallapragada[1]
[1]Department of Chemical Engineering, Iowa State University, Ames, Iowa, USA 50011
[2]Iowa Cancer Research Foundation, Urbandale, IA 50322

Abstract

New cationic pentablock copolymers of poly(diethylaminoethylmethacrylate) (PDEAEM), poly(ethylene oxide) (PEO) and poly(propylene oxide) (PPO) (PDEAEM-b-PEO-b-PPO-b-PEO-b-PDEAEM) synthesized in our laboratory were investigated for their potential as non-viral vectors for gene therapy. Agarose gel studies show that polymers effectively condense plasmid DNA to form polyplexes, and also protect DNA against nuclease degradation. Light scattering and transmission electron microscopy were used to analyze the apparent size, molecular weight and morphology of these polyplexes. Lactose dehydrogenase assay was employed to find the viable concentrations of polymers and polyplexes on various cell lines. These polymers showed much less cytotoxicity than commercially available Ex-Gen (linear PEI). These pentablock copolymers exhibit thermodynamic phase transitions suitable for subcutaneous injections into the body and polyplex release over time. Their pH sensitive protonation helps them in endosomolysis, increasing their transfection efficiency. *In-vitro* transfection efficiency of the polymers using Green fluorescent protein (pEGFP) and Luciferase (pRL-CMV) reporter genes was comparable to the commercially available Ex-Gen (linear PEI).

1. Introduction

Non-viral gene therapy using biocompatible cationic copolymers has recently gained increased interest as a potential cure for cancer and several genetic diseases [1, 2]. It can overcome problems encountered with viral-based therapies, like immunogenicity, toxicity, mutagenicity and potential danger of oncogenicity [2]. A non-viral gene therapy involving polymers provides flexibility to design a carrier having well defined structural and chemical properties on large scale. The positively charged groups of the polycation enable formation of "polyplexes" with the negatively charged phosphates of DNA via electrostatic interactions. This results in DNA condensation, protection from the nuclease digestion and more efficient delivery into a cell [3]. A variety of polycations have been proposed and investigated for polyplex formation [4], such as poly-L-lysine (PLL) [5], polyethylenimine (PEI) [6], polyamidoamine dendrimer [7], (poly(2-dimethylamino)ethyl-methacrylate) (PDMAEMA) [8]. However, these systems are very toxic and they tend to aggregate *in vivo* [9, 10]. Also, they need to be administered repeatedly for sustained gene expression.

Amine methacrylate-based polymers have previously been reported as one of the efficient cationic condensing agents for gene delivery [11, 12]. We have designed novel pentablock copolymers of PDEAEM and Pluronic® [13]. They retain the thermoreversible gelation properties of the triblock Pluronic® [14], while providing a pH-sensitive release profile for self-regulated drug release and endosomolysis [15]. These polymers are positively charged at physiological pH and are protonated at low pH. The polymer can be mixed with the therapeutic gene in an aqueous phase at low temperatures (below 4°C) where it exists as sol and form polyplexes. In this form, the polyplexes are injectable. On subcutaneous injection and subsequent heating to body temperature, the copolymer self-assembles into a gel [13] that can act as a reservoir for sustained release of polyplexes. This has several advantages over common gene delivery systems. First, the

formulation is simple and requires no organic solvent. Second, there is no requirement for a surgical procedure to implant or remove the matrix. Third, the polyplexes can be stored at 0°C in refrigerator in solution before administration. Fourth, the fraction of the cationic polymer in the copolymer can be varied to tailor and minimize the cytotoxicity of the polymer, while still maintaining good transfection efficiency. Last, controlled release of the gene over a period of time circumvents frequent repeated administration required with other polymers.

2. Materials and Methods

2.1 Materials

Dulbecco's modified Eagle medium (DMEM), fetal bovine serum, 0.25% trypsin-EDTA solution and Hank's buffered salt solution (HBSS) were purchased from Invitrogen (Carlsbad, CA). A lactate dehydrogenase (LDH) assay kit was purchased from Takara Bio Inc. (Otsu, Japan). The Renilla luciferase assay system was purchased from Promega (Madison, WI). The Qiagen Maxi Prep kit was purchased from Qiagen (Valencia, CA). FuGene6 non-liposomal cationic lipid transfection reagent was purchased from Roche Applied Sciences (Indianapolis, IN). ExGen-500 linear polyethyleneimine transfection reagent was purchased from Fermentas Life Sciences (Vilnius, Lithuania). DNase I was purchased from Ambion (Austin, TX). All water used in procedures was ultrapure water with at least 18 MΩ resistivity, prepared using a nanopore ultrafiltration unit fed with distilled, deionized water.

2.2 Plasmid DNA

A 4.7-kb plasmid DNA encoding enhanced green fluorescent protein (pEGFP-N1) (ClonTech, Mountain View, CA) under the regulatory control of the cytomegalovirus (CMV) promoter was used as the reporter gene. To measure the levels of protein expression, we used a luciferase transfection assay, employing a 4.1-kb plasmid encoding *Renilla* luciferase (pRL-CMV) (Promega). Plasmids were inserted into DH5α *E. coli*, incubated in selective Luria-Bertani (LB) medium and purified using the Maxi-Prep DNA purification kit from Qiagen. The concentration and purity of the resulting DNA in a buffer of tris-HCl and ethylenediaminetetraacetic acid (EDTA) was measured by measuring the absorbance at 260 nm and 280 nm. All DNA used had a 260/280 ratio of at least 1.80.

2.3 Synthesis of pentablock copolymers

Structure of pentablock copolymer

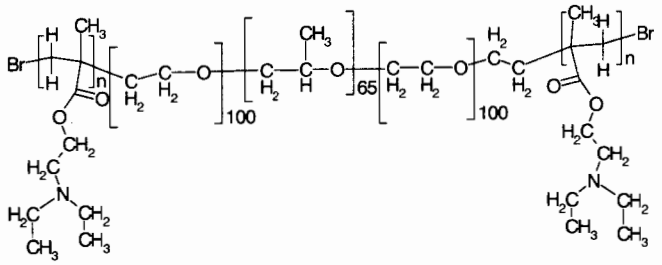

The pentablock copolymers were synthesized using ATRP reaction scheme, which is discussed in detail elsewhere [13]. Pentablock copolymers with different wt% of PDEAEM blocks were synthesized and investigated for gene delivery. Molecular weights of the pentablocks varied from 15 kDa to 22 kDa with polydispersities of up to 1.4.

Table 1: Pentablock copolymers used for study in this paper

Pentablock copolymer	M_n (NMR)	M_n (GPC)	PDI	% PDEAEM
1056A	15,000	40,112	2.36	17
1294A	17,300	23,516	1.235	25
SMC930C	22,000	30,664	1.206	40
1299C	19,973	20,365	1.338	62

2.4 Cell culture

Cell line used for cytotoxicity and transfection experiments was SKOV3 (human ovarian cell carcinoma). Cell cultures were maintained in a humidified environment with 5% CO_2 at 37°C and passaged regularly to remain subconfluent. Cells were fed with Dulbecco's Modified Eagle Media (DMEM) containing 10% fetal bovine serum (FBS), unless otherwise stated. Neither antibiotics nor antimycotics were used, to avoid the possibility of artificial membrane permeabilization effects from these agents.

2.5 Polymer-DNA complexes (Polyplexes)

Copolymer to DNA ratios are expressed as molar ratios of phosphate (P) in DNA to nitrogen (N) in DEAEM, and written as P:N. The molecular weight for the DEAEM monomer is 171 and the average molecular weight of a nucleotide is approximately 308. All polyplexes were formed by the same procedure. The copolymer was dissolved in ultrapure water to achieve a concentration of 1.00 g/L and then diluted with the desired media, buffer or water in a polypropylene tube. After incubating for 5 min at 20°C, this solution was added to the appropriate solution of DNA. This tube was gently agitated and allowed to incubate for 30 min at room temperature.

2.6 Molecular weight analysis and particle size determination

Multi-angle light scattering (MALS) analysis using a DAWN MALS detector (Wyatt, Santa Barbara, CA) was used to analyze the apparent size and molecular weight of the synthesized copolymers and their polyplexes dissolved in water. Samples were filtered three times through 0.22-μm syringe filters from Millipore (Billerica, MA) into clean scintillation vials to prevent particulate contamination. Vials were cleaned by rinsing with triple-filtered ultrapure water followed by rinsing with triple-filtered methanol and, then ethanol, and allowed to dry inverted in a sterile laminar-flow environment.

A JEOL 1200EX2 scanning/transmission electron microscope (Tachikawa, Japan) was used to visualize the morphology of polyplexes, prepared at varying P:N ratios in 0.1 mM phosphate buffer saline. A 10-μL drop of the sample was placed onto a formvar-coated copper grid and allowed to adsorb. After 5 min, the liquid was wicked with filter paper. The grid was then placed immediately into a solution of 4% w/v uranyl acetate in 50% ethanol and allowed to stain for 30 min. The sample was rinsed by repeated immersion in 50% ethanol followed by two rinses in deionized water. After rinsing, the samples were loaded into the vacuum stage of the microscope and visualized at 80 kV under magnifications of 40,000X to 250,000X. Naked DNA (pEGFP-N1) and the copolymer alone were also examined.

2.7 Gel retardation assay

To study the pentablock copolymer condensation with DNA, agarose gel (0.45%) electrophoresis of the polyplexes at different P:N ratios were conducted to compare their mobility. 1 μg of DNA per well was used. After adding 2–6 μL of sucrose loading buffer, 15 μL of each sample

was loaded to the appropriate well in a 0.45% agarose gel with 0.1 μg/mL ethidium bromide. The gel was run in TBE buffer at 60 V for approximately 1 h. Visualization and image capture was accomplished using a UV-transilluminator under a Kodak EDAS 290 digital imaging suite (Fisher, Pittsburgh, PA). A 1-kb+ DNA ladder and pEGFP-N1 DNA served as controls.

2.8 Nuclease resistance assay

To investigate the ability of the pentablock copolymers to protect DNA from enzymatic degradation, polyplexes were exposed to DNase I, and run on an agarose gel. Polyplexes were prepared at different P:N ratios. Appropriate buffers and the enzyme DNase I (RNase-free) were added to yield either 4 or 50 U/μg of DNA. Samples were incubated for 1 h at 37°C and then run on agarose gels. Naked pEGFP-N1 DNA served as a negative control, and naked pEGFP-N1 DNA with DNase I served as a positive control.

2.9 Cytotoxicity assay

Lactate dehydrogenase (LDH) is an integral cytosolic enzyme that is secreted out in the medium on the rupture of cell membrane [16], since its a potential site of interaction of cationic macromolecules [17]. Cells were cultured into 96-well tissue culture plates at a density of approximately 27,500 cells per well. After incubation overnight, the DMEM was removed, and replaced with appropriate polymer solutions in 200 μL fresh DMEM. Cells were allowed to incubate in the presence of the test substances for 24 to 48 h. 100 μL of media was then collected in an optically clear 96-well microtiter plate, and LDH concentration was assayed using a commercial kit (Takara Bio LDH cytotoxicity detection kit, Otsu, Japan). The absorbance at 500 nm was measured for each well using a BioTek (Winooski, VT) EL-340 plate reader. Media alone and media with only cells were used to obtain a background LDH level for normalization. Cells exposed to 0.1% Triton X-100 in DMEM were used as a high control, and set as 100% LDH release. The relative LDH release is defined by the ratio of LDH release over total LDH in the intact cells. Less than 10% LDH release was regarded as nontoxic effect level in our experiments. All samples were run in four replicates, and experiments were repeated twice. After incubation with polymers, changes in morphology and detachment of cells from the dish were also observed using an Olympus (Hamburg, Germany) IMT-2 inverted, phase-contrast light microscope equipped with an objective of 100x magnification.

2.10 In-vitro transfection

2.10.1 Detection of green fluorescent protein. Green fluorescent protein (GFP) was used for the assessment of *in vitro* transfection efficiency of the copolymers in SKOV-3 and NIH-3T3 cell lines. Various formulations of polyplexes were made in OptiMEM with different P:N ratios with fixed amount of pEGFP-N1 (6 μg of DNA per well in a six-well multiwell plate). Cells seeded in six-well plates were incubated overnight up to 70% confluency prior to transfection. The growth medium was then removed and replaced with test solution of polyplexes along with 1 mL OptiMEM. The cells were left to incubate for 4 h at 37°C, after which the transfection medium was replaced with fresh DMEM containing 10% FBS, and cells were incubated for another 44 h to express the reporter gene. The advantage of using pEGFP as a reporter gene is that it can be observed both qualitatively and quantitatively. Cells expressing GFP were visualized directly on an Olympus IMT-2 microscope. Images were recorded using an attached Nikon Coolpix 990 digital imaging system, without disrupting the cells. Flow cytometry was used to obtain the percentage of cells transfected with the pEGFP-N1. Cells were harvested from the plates using

HBSS and trypsin-EDTA treatment, and were suspended in 3 mL HBSS in centrifuge tubes. These were spun at 1200 rpm for 10 min. The supernatant was removed and the cell pellet was again suspended in 3 mL HBSS to remove background fluorescence from the media. After repeating the centrifugation, cells were finally suspended in 0.5 mL HBSS and were transferred to flow cytometry cuvettes for analysis. Flow cytometry was performed using a Beckman-Coulter (Fullerton, CA) Epics ALTRA fluorescence-activated cell sorter. ExGen-500 (linear polyethyleneimine, PEI) was used as positive controls, and was expected to yield high efficiency of transfection. Cells exposed only to DNA (without polymer) were used as negative controls.

2.10.2 Detection of luciferase activity. In order to determine the total protein expressed by a reporter gene per total cellular protein, the luciferase assay was employed, using pRL-CMV as the reporter gene. Cells were seeded in a 96-well plate up to 70% confluency prior to transfection, and were then transfected with various polyplexes solution in 200 μL OptiMEM® using 1.5 μg of DNA per well. After 4 h incubation in OptiMEM, the solution was replaced with fresh DMEM containing 10% FBS, and left for incubation for 44 h. Cells were then lyses using a lysis buffer and the luminescence of the expressed reporter protein was measured on an automated Berthold Mithras (Bad Wildbad, Germany) LB940 multilabel luminometer using the Promega luciferase assay kit. Positive and negative controls similar to those for pEGFP were used. Total cellular protein content of the cells was determined by a modified Bradford assay, using a CB-Protein Assay™ Kit. Bovine serum albumin standards were prepared.

3. Results and Discussion

3.1 Molecular weight analysis and particle size

Zimm plots were obtained from the MALS analysis. For the polymer with 26% PDEAEM, the weight average molecular weight was $(3.118 \pm 0.097) \times 10^6$ g/mol, and the radius of gyration was 18.3 ± 2.0 nm. Light scattering data from polymer solutions in triple filtered nanopure water with concentrations of 0.4, 0.8, 1.0 and 1.2 mg/mL were used for analysis. The second virial coefficient was $(-9.457 \pm 0.387) \times 10^{-5}$ mol mL/g^2. The negative value suggests a poor interaction of polymer and the solvent. This indicates that polymer forms micelles due to hydrophobic interactions with water. This indicates that polymer chains self-assemble into micelles due to hydrophobic interactions with water.

For the polyplexes with P:N ratio 1:5, weight average molecular weight was $(2.151 \pm 0.091) \times 10^7$ g/mol, with radius of gyration of 32.3 ± 1.6 nm. Light scattering data from polyplex solutions with 0.6, 0.8, and 1.0 mg/ml concentrations was used for analyis. The second virial coefficient, which quantifies polymer-solvent interaction, was $(-2.004 \pm 0.147) \times 10^{-6}$ mol mL/g^2. This indicates that polyplexes are formed by the interaction of DNA with polymer micelles.

TEM images were obtained to observe the morphology of polyplexes. Fig. 4 shows an image of polyplexes with 17% PDEAEM and pEGFP. In the image, condensates appear to be in two forms: first, toroidal ring structures, and second, structures with a linear morphology, which usually have loops at either end. Similar structures were obtained irrespective of the ratio of the polymer to DNA. Real-time images of such toroidal and rod-like condensates formed with cationic polymers like PEG-poly(amidoamine) triblock copolymer and plasmid DNA have been reported earlier in other studies also [18, 19]. The average diameter of rings was approximately 50 nm and the average length of rods was approximately 100 nm. This is very much in compliance with the MALS data shown above. However, dehydration of the samples for TEM imaging disrupts the micelles of polyplexes otherwise would have formed in an aqueous environment,

affecting the apparent size and morphology of the condensates. To appreciate the complex architecture of the polymer-DNA condensates, images of uncondensed pEGFP plasmids, and only polymer were also taken (images not shown here). TEM images show distinct differences among the polyplexes, DNA and polymer. DNA was stringy and formed supercoils and larger loop structures. When several loops combined, DNA appeared to clump. The polymer looked like braided strands. It also clumped to form denser structures. We observed different polymer particulates; some appear long and slender while others were nearly spherical.

3.2 Strength of polyplexes

Experiments were performed to investigate whether the pentablock copolymers form complexes with plasmid DNA (pEGFP). Fig. 3 shows the results from the gel retardation assay. DNA was visualized by fluorescence of ethidium bromide. Lane 7 containing naked plasmid DNA shows at least three distinct bands, corresponding to the different states of supercoiling in the double-stranded pEGFP-N1 plasmid DNA. The movement of plasmid DNA was retarded as the amount of pentablock copolymer in a complex increased, suggesting that pentablock copolymer forms a complex with plasmid DNA (lanes 1–6). Lanes 1–3 have pentablock copolymers with 17% PDEAEM and lanes 1–6 have pentablock copolymers with 40% PDEAEM. Almost complete retardation was achieved at P:N ratio of 1:1, which reflects that negatively charged DNA was completely neutralized by the cationic polymer, forming a polyplex via ionic interactions. At P:N ratios of 1:5 and 1:10, the band seems to move slightly upward, suggesting that these polyplexes have an overall positive charge.

3.3 Protection against nuclease degradation

The agarose gel in Fig. 4 exhibits that the pentablock copolymer protects plasmid DNA against DNase I digestion. Naked pEGFP-N1 DNA in lane 14 served as a negative control, and naked pEGFP-N1 DNA with DNase I in lane 13 served as a positive control. Lanes 6 and 12 contain 1kb+ ladder for the control. Lanes 1 to 5 contain polyplexes of pentablock with 17% PDEAEM, and lanes 7 to 11 contain those of 40% PDEAEM. Bright bands of DNA at the top of lanes 3, 4, 9, and 10 reflect that plasmid DNA is still present and is not digested by DNase I. Thus, P:N ratio of 1:5 and above is sufficient to complex the DNA and protect it against nuclease degradation. Lanes 5 and 11 show that at unusually high concentrations of DNase I (50 units per μg of DNA, as compared to 4 units in other lanes) all DNA is digested. Very light bands present on the top of lanes 1, 2, 6, and 7 reflect the fact that even at lower P:N ratios, some of the plasmid DNA is protected by the polymer from nuclease digestion. Lanes 3, 4, 9, and 10 show slightly weaker bands in fluorescence intensity as compared to naked plasmid in lane 14, probably due to the exclusion of the ethidium bromide following formation of complexes.

3.5 *Cytotoxicity*

The pentablock copolymers with different weight percentages of PDEAEM were tested for their toxicity on SKOV3 (human ovarian cancer) cell lines. A cut-off concentration was found for each polymer at which less than 10% cell death was observed. Later, all transfection experiments were performed within these cut-off concentrations of the polyplexes. As shown in Fig. 4, cell viability decreased in polymers with higher weight-percentages of PDEAEM. Microscopic images of cells in Fig. 5 show how the cell morphology changes as polymer concentration increases in toxicity. In the presence of no polymer (Fig. 5A), cell bodies are large, confluent and cover the entire surface of the plate. However, at higher concentrations of the polymer (Fig. 5C), cell bodies are small, sparse and disperse, indicating cell death. At an optimal concentration (Fig.

5B), cells appear to be healthy and sub-confluent. As seen from Fig. 4, this concentration of 40% PDEAEM is close to the cut-off concentration measured by the LDH assay.

3.6 In vitro transfection

3.6.1 Green fluorescent protein assay

Flow cytometry was used to measure the percentage of cells transfected by pEGFP. Transfected cells showed stable expression of the reporter gene over time. Fig. 6 shows the percentage of cells transfected at different P:N ratios using the 26% PDEAEM. Up to 17% transfection was achieved by the pentablock copolymer, which is very much comparable to the 20% transfection obtained from the commercially available and much more toxic Ex-Gen (linear PEI). Also, higher transfection was obtained at higher P:N ratios of the polymer. However, at very high P:N ratios, the toxicity increases due to increased polymer content, and the cells can die before they can get transfected or express the protein from the transfected gene.

3.6.2 Luciferase assay

To determine the total amount of reporter protein expressed by the cells, a renilla luciferase assay was employed. Polymers at different P:N ratios with pRL-CMV plasmid were tested for the amount of transfection obtained. Fig. 7 show the amount of luciferase expressed in terms of relative luminescence units (RLU). The experiments were conducted in a 96-well plate with 1.5 μg of DNA/well. At this DNA dose, the amount of transfection increased with increase in P:N ratio from 1:2 to 1:3. However, at P:N ratios of 1:4 and above, the amount of polymer used surpassed the cut-off concentration at which cells could be viable, and hence the decrease in the protein expressed was observed. Positive control Ex-Gen also shows an increase in transfection with increase in P:N ratio form 1:1 to 1:2. It is appreciable that RLUs obtained from our much more biocompatible pentablock copolymers are of the same order as RLUs from Ex-Gen. Total cellular protein content of the cells was assayed using a Bradford assay kit, and was not significantly different in different cases. On average, the total amount of cellular protein was 3.56 μg in each well.

4. Conclusions

The key challenge for plasmid-based gene therapy is to surmount the limiting steps in intracellular movement including endosomal release, cytoplasmic transport, and nuclear uptake, and to enhance the retention of plasmids in the nucleus.

Our pentablock copolymers show great promise as non-viral vectors for gene therapy. They are water-soluble, pH-sensitive, and have thermoreversible gelation properties. Their ability to effectively condense DNA into polyplexes, and protect plasmid against nuclease degradation is an important first step towards vector for gene delivery. The condensed polyplexes are small enough to allow cellular uptake. MALS show that polymer and polyplexes exist in the form of micelles. TEM images of the polyplexes show that plasmid is condensed into some definite ring (diameter ~ 50 nm) or rod-like structures (length ~ 100 nm). Since samples were dehydrated for obtaining the TEM images, disrupting the micelles formed by polyplexes in an aqueous environment, cryo-TEM studies in the future will preserve the micellar structure of the polyplexes and provide a more accurate image.

Also, these effectively positively charged complexes in the form of micelles improve the cellular uptake via adsorptive endocytosis by the lipid bilayer membrane of the cells. Nuclear trafficking is accomplished by the pH-sensitive proton sponge behavior of the polymer.

The pentablock copolymers are not very toxic and their cytotoxicity can be tuned by changing the percentage of the cationic component. They give good transfection of reporter genes within the toxicity limit. They are much less toxic (up to 50 times) to the commercially available transfecting agent Ex-Gen® (linear PEI). The transfection efficiency of the pentablock is comparable to that of Ex-Gen®. Besides, our pentablock copolymer also offers opportunity to ligand targeting moeties like EGF to its ends, which can significantly increase the cellular uptake by the cancer cells producing excessive EGF receptors on their cell membranes. Nucleus locating signals (NLS) can also be ligated to our pentablock, which would increase the nuclear uptake of the polyplex, overcoming a major black box hindrance in transfection.

In the near future, we will conduct *in vivo* transfection studies on mice, studying the *in vivo* transfection efficiency, and identify pentablock copolymer's ability to avoid activation of the compliment immune systems in the body. When a safe, efficient synthetic gene delivery vector system is developed, we will use it for suicide gene therapy against cancer [20, 21].

Acknowledgments

The authors would like to thank Tracey Pepper and Dr. Jack Horner of the Iowa State University Bessey Microscopy Center for work with transmission electron microscopy, Mike Determan for polymer synthesis and characterization (gel permeation chromatography, NMR), Amanda and Christine at the ISU Cell and Hybridoma facility, and the ISU Office of Biotechnology for use of the Mithras LB940 luminometer and the fluorometer. The authors also acknowledge the financial support of the USDOE Ames Laboratory and a Bailey grant.

References

1. Felgener, P., Hum. Gene Ther., 1997. 8: 511–512.
2. Merdan, T., K.J., Kissel Thomas, Adv. Drug Deliv. Rev., 2002. 54: 715–758.
3. De Smedt, S.D.J., and Hennink, W., Pharm. Res., 2000. 5: 1425–1433.
4. Han S., Sung, Y. K., and Kim, S. W., Molec. Ther., 2000. 2: 302–317.
5. Gondsho, A., Irie, K., Susaki, H., Iwasawa, H., Okuno, S., and Sugawara, T., Biol. Pharm., 1994. 17: 275–282.
6. Boussif, O., et al., Proc. Natl. Acad. Sci. USA, 1995. 92: 7297–7301.
7. Tang, M.X., Fedemann, C.T., and Szoka Jr., F.C., Bioconj. Chem., 1996. 7: 703–714.
8. Van De Wetering, P., Talsma, H., Crommelin, D.J.A,, and Hennik, W.E., J. Cont. Release, 1998. 53: 145–153.
9. Brazeau, G.A., Attia, S., Poxon, S., and Hughes, J.A., Pharm. Res., 1998. 15: 680–684.
10. Dash, P.R., Read, M.L., Barret, L.B., Wolfert, M.A., and Seymour, L.W., Gene Ther., 1999. 6: 643–650.
11. Van De Wetering, P., Schuurmans Nieuwenbroek, N.M.E., van Streenbergen, M.J., Hennink, W.E. Bioconj. Chem., 1999. 10: 589–597.
12. Van De Wetering, P., van Streenbergen, M.J., Crommelin, D.J.A., and Hennink, W.E. J. Cont. Release, 2000. 64: 193–203.
13. Determan, M.D., In preparation, 2004.
14. Kabanov, A.V., Batrakova, E. V., Alakhov, and Valery, Yu., J. Cont. Release, 2002. 82: 189–212.
15. Kristensen, R.A., Clamme, J.P., Vuilleumier, C., and Kurthy, Y. M., Biochim, Biophys. Acta, 2001. 1514: 21–31.
16. Ficher, D., Ahlemeyer, B., Krieglstein, J., and Kissel, T. Biomaterials, 2003. 24: 1121–

1131.
17. Choksakulnimitr, S., Tokda, H., Takakura, Y., and Hashida, M. J Cont. Release, 1995. 34: 223–241.
18. Martin, A.L., Rackstraw, B.J., Roberts, C.J., Stolnik, S., Tendler, S.J.B., and Williams, P.M., FEBS Lett., 2000. 480: 106–112.
19. Rackstraw, B.J., Stolnik, S., Roberts, C.J., Garnett, M.C., Davies M.C., Tendler, S.J.B., Langmuir, 2001. 17: 3185–3193.
20. Aghi, M., Breakfield, X.O., J. Gene Med., 2000. 2: 148–164.
21. Iwai, M., Harada, Y., et al., Biochim. Biophys. Res. Commun., 2002. 291: 48–54.

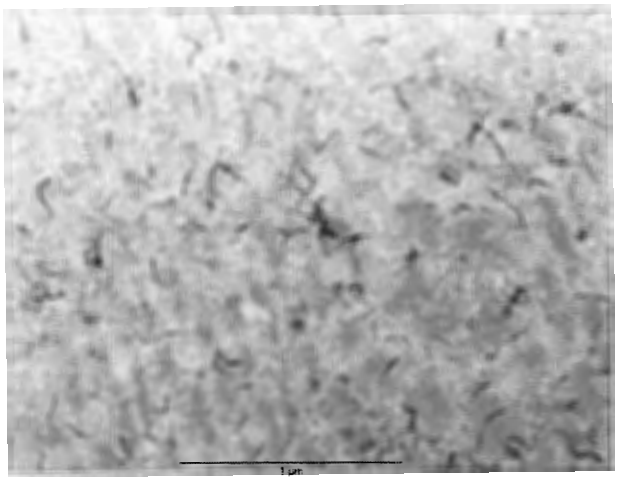

Fig. 1: TEM image of the polyplexes obtained from the condensation of pEGFP by pentablock with 17% PDEAEM at 1:5 P:N ratio.

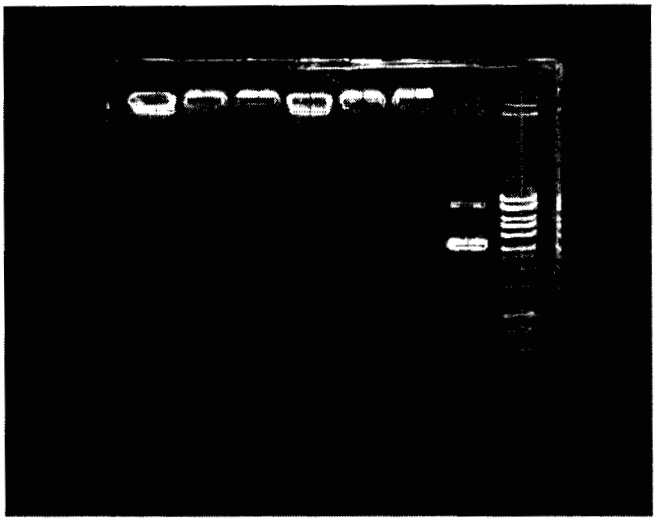

Fig 2: Agarose gel electrophoresis showing DNA complexation.

Fig 3: Agarose gel electrophoresis showing protection of plasmid pEGFP against DNase I digestion.

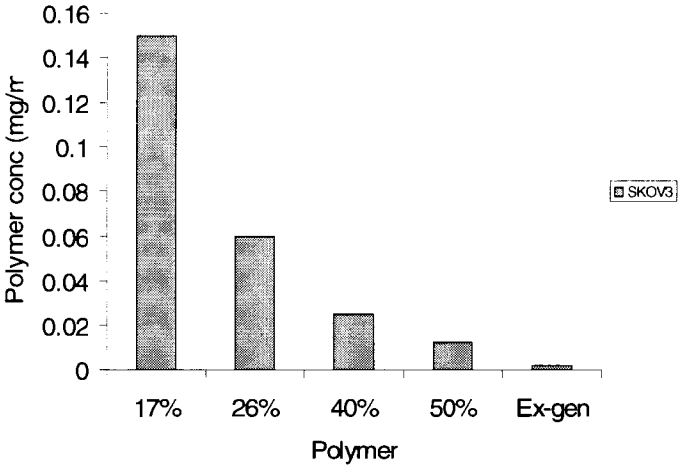

Fig 4: Cut-off concentrations of different polymers under which they are not toxic to SKOV3 cell line for up to 48h.

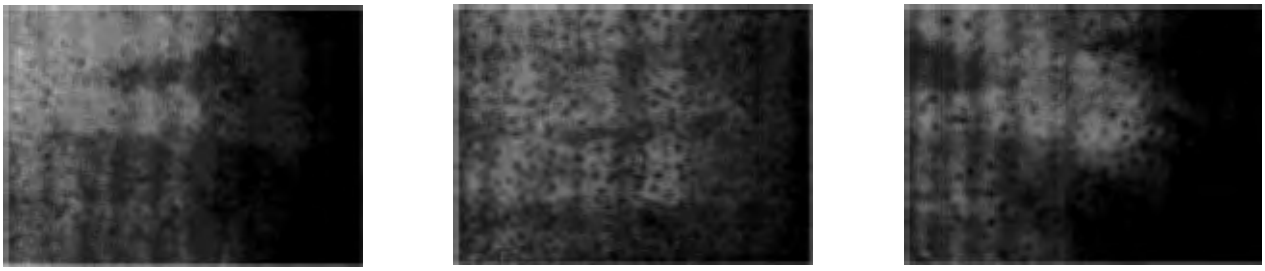

(A) no polymer (B) 0.03 mg/mL (C) 0.05 mg/mL

Fig. 5: Morphology of the SKOV3 cells after incubation for 48 h with pentablock copolymer (40% PDEAEM).

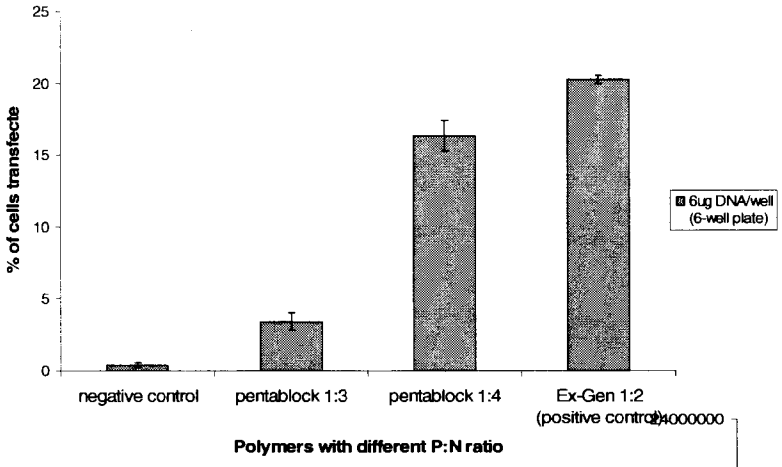

Fig. 6: In-vitro transfection of pEGFP in SKOV3 cells using pentablock (26% pDEAEM).

Fig. 7: In-vitro transfection of pRL-CMV in SKOV3 cell line using pentablock (26% pDEAEM). Effect of P:N ratio on transfection of SKOV3 cells.

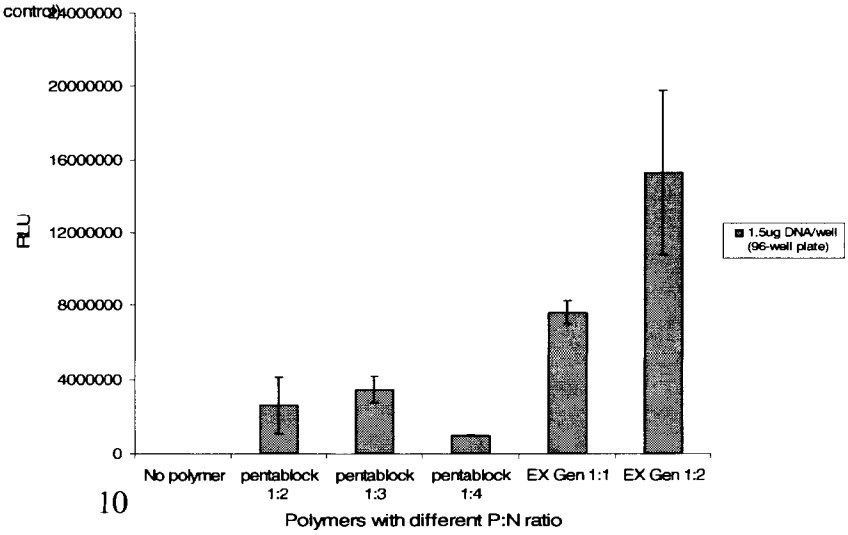

Lipase-Catalyzed Esterification of Geraniol in Ionic Liquid [bmim]PF_6

Donifan Barahona, Peter H. Pfromm, and Mary E. Rezac
Department of Chemical Engineering, Kansas State University, Manhattan, KS 66506

Abstract

The use of non-aqueous media is effective for carrying out enzymatically catalyzed reactions in which the reactants are not water-soluble or in which water is a byproduct that limits conversion. Organic solvents are commonly used for this purpose, yet they are potentially environmentally damaging. Ionic liquids, organic salts that are liquid at room temperature, are a potentially useful alternative. In this work, the direct esterification of geraniol with acetic acid in [bmim]PF_6 has been investigated. Immobilized *Candida antarctica* lipase B has been used to catalyze the reaction. Significant enzymatic activity is observed in [bmim]PF_6 although the reaction rate was slower than in hexane.

Introduction

Enzymatic catalysis of nonaqueous media has been an active area of investigation during the last twenty years. Enzymes are active in media other than water and it has been possible to carry out reactions where water is one of the reaction products, or using non-water soluble substrates [Klibanov, 1997]. Particularly, many enzymes work well in organic solvents: they are thermally more stable than in water. They show enhanced selectivity, stability, and selectivity. It has also been possible to carry out reactions that were prohibited in aqueous media due to equilibrium limitations or where the substrates were not water-soluble. The main chemicals that are produced using this technique are fragrances, flavors, and specialized pharmaceuticals [Krishna, 2002]. However, since most organic solvents are volatile, they have a detrimental effect on the environment, and it is necessary to find synthetic techniques for reducing the level of emissions and the environmental harmfulness [Nara, 2002].

Besides organic solvents, supercritical fluids, gases, and ionic liquids (ILs) have been used as nonconventional media for enzymatic reactions [Krishna, 2002]. The last group of solvents has gained much attention in the last years because of their novel properties. Room-temperature ILs are salts with melting points below 100 °C. Because of their ionic nature, ILs have negligible vapor pressure and are thermostable [Huddleston, 2001]. They are attractive to replace organic solvents in chemical processes since this eliminates volatile organic compound (VOC) emissions. Most ILs are composed of one organic cation and one inorganic or organic anion. The properties of ILs can be adjusted by selecting proper cation-anion combinations [Huddleston, 2001]. Theoretically, it is possible to design a particular IL for any specific application [Nara, 2002]. Different cation-anion combinations are shown in Figure 1.

ILs are good solvents; they are able to dissolve polar and nonpolar organic components. They also have a wide liquid range (usually greater than 300 °C), so are suitable to carry out typical liquid-phase reactions [Seddon, 2000]. Although no studies have been reported on the effects of increasing the IL presence in the environment, they are generally considered environmentally friendly because they are stable towards air and water [Seddon, 2002].

In this work we carry out the direct esterification of geraniol with acetic acid in the IL 1-butyl-3-methyl imidazolium hexafluorophosphate, [bmim]PF_6, catalyzed by immobilized enzyme *Candida antarctica* lipase B (CALB) Novozym® 435. Geranyl acetate is an important chemical used extensively in fragrance and flavor industries [Peres, 2003]. The main goal of this work is to probe the activity of lipases in ILs.

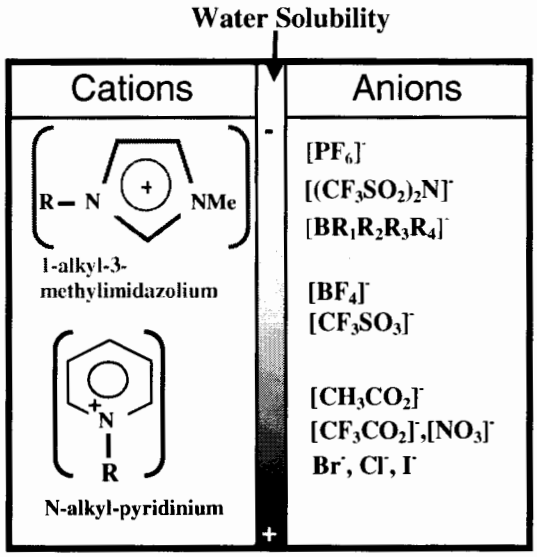

Figure 1. Typical anion-cation combinations in ILs. Water solubility changes as different pairs are selected.

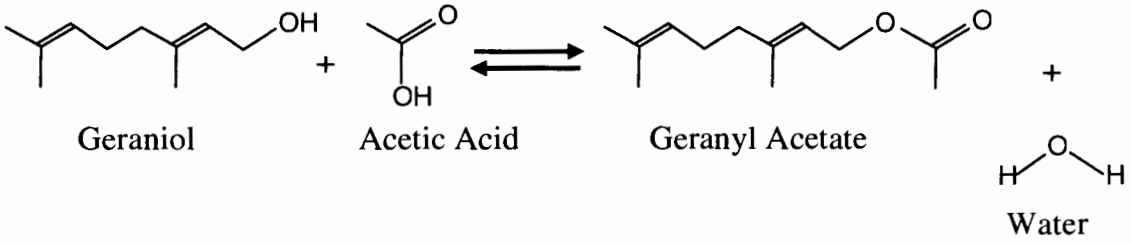

Scheme 1. Direct esterification of geraniol to produce geranyl acetate and water.

Background

Different results have been published on the use of lipases to catalyze esterification reactions in ILs. Kaar et al. [2003] studied the impact of different ILs on the reaction properties of lipases. Transesterification of methyl methacrylate was used as a model reaction. Most of the ILs tested (water-soluble and nonsoluble) showed no activity for free or immobilized enzymes. However, free CALB lipase was 1.5 times more active in [bmim]PF_6 than in hexane, although no activity was reported for immobilized *C. antarctica* lipase B Novozym® 435. Gubicza et al. [2003] carried out the enantioselective esterification of (R,S)-2-chloropropanoic acid with butan-1-ol using free *Candida rugosa* lipase. Although the enantioselective properties of the enzyme were not studied, the activity of the enzyme in [bmim]PF_6 was comparable with that in hexane. Lozano et al. [2001] carried out the butyl butyrate synthesis catalyzed by free *C. antarctica* lipase B using four different ILs. All of the ILs tested were suitable media for the transesterification reaction. The enzyme activity in [bmim]PF_6 was about twice that in hexane. Itoh et al. [2001] have reported a 5-phenyl-1-penten-3-ol conversion of 47% after 5 h for the transesterification reaction with vinyl acetate using Novozym® 435 as catalyst. Husum et al. [2001] reported 90 % butyric acid conversion after 1 h for the esterification reaction with a simple alcohol. Novozym® 435 was used as catalyst. Different results obtained by several groups could be attributed to differ-

ences in IL properties; many of them were synthesized in the laboratory, and as has been reported, many residual solutes from the synthesis process have a strong influence on the properties of ILs [Seddon, 2000].

Although no data were found on geranyl acetate synthesis in ILs, its production has been reported using organic solvents as reaction media. Chulalaksananukul et al. [1992] carried out the transesterification of several acetates to produce geranyl acetate in hexane using lipase from *M. miehei.* There is an optimal level of water content (measured in the solid support of the immobilized enzyme) for which the initial rate has a maximum. Kinetic data obtained by experimentation was fitted using a ping pong bi bi mechanism with substrate inhibition. Akoh and Claon [1994] showed that *C. antarctica* lipases SP382 and SP435 were able to catalyze the direct esterification of geraniol to produce geranyl acetate in *n*-hexane. They studied the influence of the amount of enzyme used, temperature, and water content of the mixture on the reaction rate. Huang and Chang [1999] carried out a kinetic study on the direct esterification of geraniol to geranyl acetate in isooctane using a surface-coated lipase from *Candida cylindracea.* A ping pong bi bi model with competitive and dead-end inhibition by acetic acid was fitted. The water content has a strong influence on the reaction rate. Although these studies addressed the influence of water in the final conversion, no water control was reported. Bartling et al. [2001] used pervaporation to remove water from the reaction mixture to esterify geraniol with acetic acid in hexane. Immobilized enzyme Novozym® 435 was used. The conversion for the reaction mediated by pervaporation was close to 100% and the reaction rate was 1.5 times greater than with no water removal.

Experimental

Chemicals. The reaction was conducted in IL [bmim]PF_6 as solvent (Solvent Innovation, Cl^- <1000 ppm, >99% pure). Geraniol (98% pure) and geranyl acetate (98% pure) were obtained from Sigma. Glacial acetic acid (>99.7% pure, optima), acetone (>99.6% pure), benzyl alcohol (>99.8% pure) and hexane (>99.9% of saturated hydrocarbons) were obtained from Fisher Scientific. Chemicals were used as received.

Enzyme. A nonspecific thermostable lipase from *C. antarctica* as a commercial preparation, Novozym 435® (Novozymes) was used. This enzyme is classified as a tryacylglycerol hydrolase (E.C. 3.1.1.3). The ester synthesis activity of the enzyme expressed in μmol/min propyl laurate produced per gram (PLU/g) is about 10,000 PLU/g. The enzyme preparation consists of the enzyme immobilized on a macroporous acrylic resin consisting of spherical particles with diameter in the range of 0.3 to 0.9 mm (bulk density: 430 kg/m^3, water content < 3% w/w) [Novozymes, 2003]. Enzyme preparation was purchased from Sigma and stored at 4 °C. The enzyme preparation was used as received.

Geraniol determination: To measure the geraniol content in the IL the following method was used: 0.5 ml of the IL containing geraniol and geranyl acetate were mixed with 2.5 ml of hexane in a 4-ml screw-capped vial. Then the mixture was shaken (Fisher Scientific standard mini-vortex) for 20 min to extract part of the reactants to the hexane phase. Afterward, 1 ml of the hexane phase was withdrawn from the vial and mixed with 15 μl of benzyl alcohol. The last mixture was analyzed by gas chromatography using benzyl alcohol as internal standard. The final content of geraniol obtained by GC analysis was correlated with its initial content in the IL. To carry out the GC analysis, 0.5-μl aliquots were injected into a Varian 3800 gas chromato-

graph (FID detector, capillary column DB-5, 30 m length, 0.25 mm i.d., isothermal at 120 °C; J&W Scientific). Injection temperature and pressure were 250 °C and 30 psia. An injection split ratio of 1/200 was used. Retention times at these conditions were 0.9 min, 1.9 min, and 3.3 min for benzyl alcohol, geraniol, and geranyl acetate respectively.

The above-described method allowed us to measure directly the concentration of geraniol in the IL. Internal standardization using benzyl alcohol was used to measure the final concentration in the hexane phase. The initial geraniol concentration in the IL (before the extraction step) was correlated with the final measured concentration in the hexane phase (after extraction). Figure 2 shows the calibration curve and the 95 % prediction interval obtained. Standard deviation for the linear model is 0.018 (in percentage units).

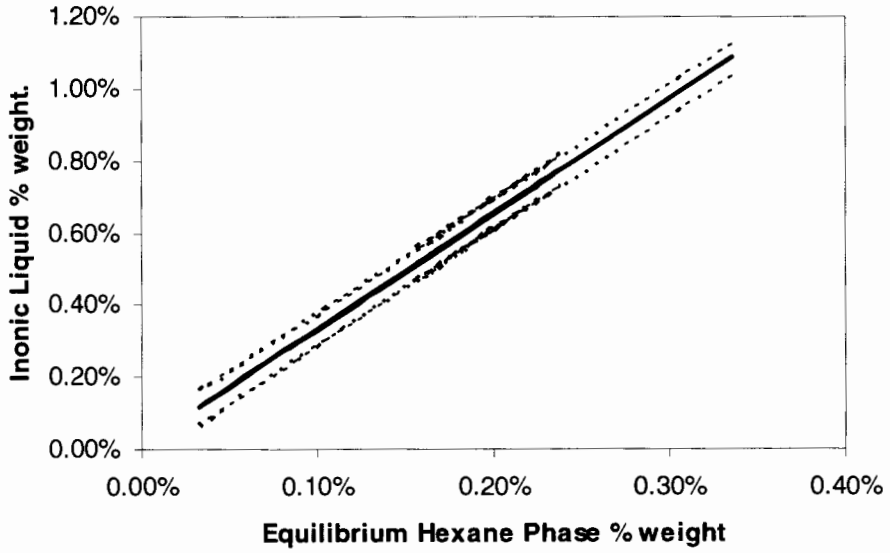

Figure 2. Calibration curve to estimate the geraniol content in IL. —: calculated linear regression. ---: 95% prediction interval.

Reaction Test. Reactor and other hardware were washed with acetone and dried to 105 °C before every experimental run. The IL was placed into the reactor and heated to the reaction temperature (30 °C). Then, geraniol (0.1 mol/l) and acetic acid (0.1 mol/l) were added. Total reaction volume was 100 ml. After the reactants were added, the reactor was sealed and kept at 30 °C using a water bath. Aliquots of 0.5 ml were withdrawn from the reactor every 4 h and the geraniol concentration in the IL was measured. After 24 h geraniol was completely dissolved and the reaction was started by adding the enzyme (0.1 g of enzyme preparation/g reactants) to the reactor. The conversion of geraniol was measured using two independent methods: measurement of the geraniol concentration using the aforementioned method and measurement of the water content by Karl Fischer titration (Denver Instruments model 270). Aliquots of 1 ml were withdrawn periodically from the reactor; 0.5 ml was used for the geraniol analysis and 0.5 ml was used to carry out the Karl Fischer titration.

Results and Discussion

The esterification of geraniol was carried out in IL [bmim]PF6. Reaction conditions were replicated from the literature [Bartling et al., 2001] and were listed before. Initial water activity was about 0.05. Figure 4 shows the conversion of geraniol calculated from data obtained by two

independent methods: measurement of geraniol content using the method mentioned earlier and measurement of the water content by Karl Fischer titration. After 74 h, a geraniol conversion of 70% was achieved; however, equilibrium was not reached up to that point. According to previous data [Kang et al., 2004] a conversion of 50% was achieved after 10 h when the reaction was carried out in hexane with a water activity of 0.1. The enzyme was less active in the IL since only 20% of the conversion was achieved after 10 h.

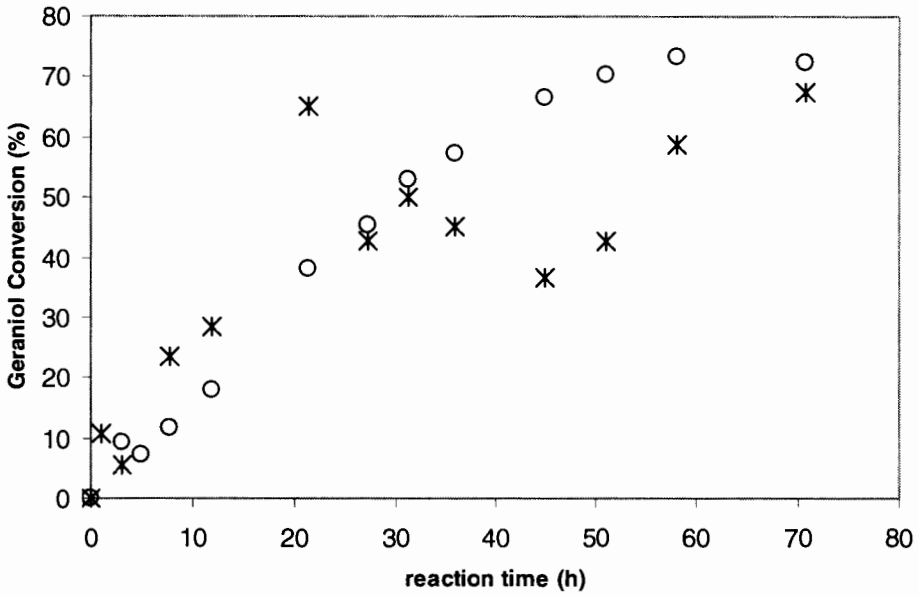

Figure 3. Geraniol conversion vs time. [x] Calculated from geraniol content measurement. [o] Calculated from Karl Fischer measurements of water assuming no side reactions.

Roughly, the data calculated using the two independent measures are in good agreement. However, the data obtained from the measurement of the geraniol content show a big variability with respect to the average. Since this variability is not shown in the data calculated from the other method (Karl Fischer), we conclude that this is variability of the method itself. The sources of variation in the developed method are: (i) variation due to the effect of other components in the mixture, since the calibration curve was built using a mixture of geraniol and geranyl acetate only; (ii) variation due to differences in the extraction method; small differences in the hexane/IL volume during the extraction could be significant in the calculated concentration, and (iii) variation in extraction times and shaking speeds during the extraction so equilibrium is not achieved. Although the method is effective, its accuracy has to be improved by minimizing sources of variation and isolating them from the obtained data by statistical analysis.

Conclusions and Future Prospects

This work has proven that Novozym® 435 is effective in catalyzing the esterification of geraniol with acetic acid when IL [bmim]PF_6 is used as solvent. It helps to support the conclusion that lipases are active in these solvents. Since no previous data has been reported for this system, this work also helps to broad the spectrum of enzyme-catalyzed reactions that can be carried out in ILs. A method to measure the geraniol content in the IL has been developed and tested satisfactorily.

In next steps of the research work the influence of water should be studied so the optimal and minimal water levels can be found. Also the study of the influence of other reactant activities will give light on the reaction mechanism. To scale up the process a method for recovery and reuse the enzyme and the solvent should be developed.

Acknowledgment

The authors are grateful for financial support by USDA Award No. 2001-35504-12970.

References

Akoh, C.C., and Claon, P.A. (1994). Enzymatic synthesis of geranyl acetate in *n*-hexane with *Candida antarctica* lipases. *JAOCS* **71**, 575–578.

Anthony, J.L., Maginn, E.J., and Brennecke, J. F. (2001) Solution thermodynamics of imidazolium-based ionic liquids and water. *J. Phys. Chem. B.* **105**, 10942–10949.

Baker R. W. Membrane Technology and Applications. Menlo Park, CA: McGraw-Hill, 2000.

Bartling, K., Thompson, J.U., Pfromm, P.H., Czermak, P., and Rezac, M.E. (2001) Lipase-catalyzed synthesis of geranyl acetate in *n*-hexane with membrane-mediated water removal. *Biotechnol. Bioeng.* **75**, 676–681.

Berberich, J.A., Kaar, J.L., and Russell, A.J. (2003) Use of salt hydrate pairs to control water activity for enzyme catalysis in ionic liquids. *Bioetchnol. Prog.* **19**, 1029–1032.

Chulalaknanukul, W., Condoret, J., and Combes, D. (1992) Kinetics of geranyl acetate synthesis by lipase-catalyzed transesterification in n-hexane. *Enz. Microb. Technol.* **14**, 293–298.

Eckstein, M., Sesing, M., Kragl, U., and Adlercreutz, P. (2002) At low water activity α-chymotrypsyn is more active in an ionic liquid than in non-ionic organic solvents. *Biotechnol. Lett.* **24**, 867–872.

Elderbinger, M., Mesiano, A.J., and Russell, A.J. (2000) Enzymatic catalysis of formation of Z-aspartame in ionic liquids – An alternative to enzymatic catalysis in organic solvents. *Biotechnol. Prog.* **16**, 1129–1131.

Garcia-Alles, L.F., and Gotor, V. (1998) Lipase catalyzed transesterification in organic media: Solvent effects on equilibrium and individual rate constants. *Biotechnol. Bioeng.* **59**, 684–694.

Gubicza, L., Nemestothy, N., Frater, T., and Belafi-Bako, K. (2003) Enzymatic esterification in ionic liquids integrated with pervaporation for water removal. *Green Chem.* **3**, 236–239.

Halling P.J. (1994) Thermodynamic predictions for biocatalysis in nonconventional media: Theory, tests, and recommendations for experimental design and analysis. *Enz. Microb. Technol.* **16**, 178–206.

Huang, S., and Chang, H. (1999) Kinetic study on the esterification of geraniol and acetic acid in organic solvents using surfactant-coated lipase. *J. Chem. Technol. Biotechnol.* **74,** 183–187.

Huddleston, J.G., Visser, A.E., Reichert, E., Willauer, H.D., Broker, G.A., and Rogers, R.D. (2001) Characterization and comparison of hydrophilic and hydrophobic room temperature ionic liquids incorporating the imidazolium cation. *Green Chem.* **3**, 156–164.

Husum, T.L., Christel, J.T., Christensen, M.W., and Kirk, O. (2001) Enzyme catalyzed synthesis in ambient temperature ionic liquids. *Biocatal. Biotrans.* **19**, 331–338.

Itoh, T.; Akasaki, E.; Kudo, K., and Shirakami, S. (2001) Lipase-catalyzed enantioselective acylation in the ionic liquids solvent system: Reaction of enzyme anchored to the solvent. *Chem. Lett.* **30**, 262–263.

Kaar, J. L., Jesionowski, A.M., Berberich, J.A., Moulton, R., and Russell, A.J. (2003) Impact of ionic liquid physical properties on lipase activity and stability. *J. Am. Chem. Soc.* **125**, 4125–

4131.
Kang, I., Pfromm, P.H., and Rezac, M.E. (2004) Data to be published. Department of Chemical Engineering. Kansas State University.
Klibanov, A. M. (1997) Why are enzymes less active in organic solvents than in water? *TIBTECH.* **15**, 97–101.
Krishna S. H. (2002) Developments and trends in enzyme catalysis in nonconventional media. *Biotech Adv.* **20**, 239–267.
Lozano, P., De Diego, T., Carrie, D., Vaultier, M., and Iborra, J. L. (2001) Over-stabilization of *Candida antarctica* lipase B by ionic liquids in ester synthesis. *Biotechnol. Lett.* **23**, 1529–1533.
Model, M., and Tester J.W. Thermodynamics and Its Applications. Cambridge, MA: Prentice Hall, 1997. 3rd ed.
Nara, S. J., Harjani, J. R., and Salunkhe, M. (2002) Lipase catalyzed transesterification in ionic liquids and organic solvents: a comparative study. *Tetrahedron Lett.* **43**, 2979–2982.
Novozymes Inc. (2003) Technical data sheet 2003-03782-01.
Peres, C., Gomes Da Silva., M.D., and Barreiros, S. (2003) Water activity effects on geranyl acetate synthesis catalyzed by Novozym in supercritical ethane and in supercritical carbon dioxide. *J. Agric. Food Chem.* **51**, 1884–1888.
Schaffer, T., Rodrigues, C.M., Afonso, C.A., and Crespo, J.G. (2001) Selective recovery of solutes from ionic liquids by pervaporation – A novel approach for purification and green processing. *Chem Commun.* **17**, 1622–1623.
Seddon K.R., and Earle, M.J. (2002) Ionic liquids: green solvents for the future. *ACS Symp. Ser.* **818**, 289–308.
Seddon, K. R.; Stark, A., and Torres, M. (2000) Influence of chloride, water and organic solvents on the physical properties of ionic liquids. *Pure Appl. Chem.* **72**, 2275–2287.
Wong, D.S., Chen, J.P., Chang, J.M., and Chou, C.H. (2002) Phase equilibria of water and ionic liquids [emim]Pf_6 and [bmim]PF_6. *Fluid Phase Equil.* **194–197**, 1089–1095.

Conformational Analysis of Gossypol and its Derivatives Using MM3

Chase L. Beisel[1], Michael K. Dowd[2], and Peter J. Reilly[1]
[1]Department of Chemical Engineering, Iowa State University, Ames, IA 50011
[2]Southern Regional Research Center, ARS, USDA, New Orleans, LA 70179

Abstract

Both the configuration and inversion pathways of gossypol, a natural product of cottonseed cited for its toxic effects on non-ruminants, were investigated using MM3(2000). Focus was placed upon thirteen forms of gossypol, including tautomers of gossypol, gossypolone, an amine-substituted form, and anydrogossypol. Gossypol is unique due to its steric hindrance around its central dihedral bond, which produces (+) and (–) enantiomers. These enantiomers are experimentally stable under normal conditions. According to the MM3 calculations, inversion pathways vary for both (+)- or (–)-gossypol in all forms analyzed, and energy boundaries (minimum of 15 kcal/mol) are too high for racemization under normal conditions. Additionally, the different contributions of steric hindrances in the inversion pathways were determined. To validate the MM3 calculations, *ab initio* calculations using GAMESS will be used in the near future.

Introduction

Gossypol, a yellow pigment found in cottonseed, is of modern interest due to its potential applications as a male contraceptive (1,2) and an anticancer agent (3). Gossypol also contributes to the toxicity of cottonseed when used as an animal feed (4), with increased potency in non-ruminants. The toxicity depends upon unique enantiomers formed by steric hindrance around the central bond connecting the two substituted naphthalene rings, where the (–) form (Figure 1A) is more toxic than the (+) form (Figure 1B) (5). The steric hindrance comes as a result of two methyl and two hydroxyl groups *ortho* to the bond, which clash during rotation of the pivot bond These enantiomers are experimentally stable under normal conditions. Racemization experiments conducted to ascertain the energy barrier have been difficult, as dehydration of gossypol to anhydrogossypol (6) significantly occurred before significant racemization could be observed. Therefore, computational experiments can be helpful to understand the nature of this boundary.

Previous groups have used computational techniques to study the energy barrier (6) and the absolute configuration of both the (+) and (–) enantiomers (7). These studies analyzed only one form of gossypol, although many forms exist in nature. We performed a thorough investigation of thirteen forms of gossypol (Figure 2), which include six tautomers of gossypol, three tautomers of gossypolone, three tautomers of an amine-substituted gossypol derivative, and anhydrogossypol. Gossypolone is the oxidation product of gossypol. Tautomers arise from rearrangement around the aldehyde groups in gossypol 1 and gossypolone 1 and the amine group in N-gossypol 1. Even though three rearrangements exist for gossypol and two exist for gossypolone and N-gossypol, the presence of one aldehyde or amine on both sides of the molecule allow for the number of structures used in this study. All computational simulations of molecular structure were done using MM3(2000), which we have used previously, but always with carbohydrates.

Methods

The thirteen forms of gossypol were constructed with the medit program and minimized with the block diagonal minimization method, both contained within the MM3(2000) package. The standard parameter set for the force field was used in all simulations. For each form of gossypol,

the minimized (+) and (–) structures were determined. Upon minimization, the driver algorithm was used to rotate the central dihedral angle in 3.0° steps until a total rotation of 180° was achieved. Steric energies were recorded at each dihedral torsion angle.

Results

All thirteen forms were successfully minimized for both enantiomers, where the naphthalene rings were approximately perpendicular, as has been observed from crystallization data (8). As expected due to their symmetric nature, (+) and (–) enantiomers of all gossypol forms had approximately matching final steric energies and dihedral torsion angles. Using these minimized structures, the central dihedral angle was driven 180° using the driver algorithm included in MM3(2000). Rotation of the angle resulted in increasing energies as the molecule deviated from its preferred conformation, with abrupt energy relaxations once each barrier was crossed. The relaxation was so fast with such an extreme change in structure that it will henceforth be called a break. Figure 3 is a suitable example, where gossypol 1 proceeds through all four energy barriers and one enantiomer lies at each energy trough.

For either enantiomer, the angle could be either increased or decreased to send the molecule through an inversion pathway. Each inversion pathway proceeds through steric clashes of the *ortho* substituents, which primarily contribute to the energy barrier. Each clash can be defined as either a *cis* clash or a *trans* clash, where a *cis* clash occurs when the methyl groups clash and the hydroxyl groups clash, and a *trans* clash occurs when a methyl group clashes with a hydroxyl group. Analysis of the molecular configurations through the inversion pathways shows that both *trans* clashes occur at the same angle, although this exact angle varies from form to form. For the *cis* clash, the clashes occurred either at the same angle, or in a stepwise manner where hydroxyl groups passed first followed by methyl groups. This is expected, for hydroxyl groups occupy much less space than methyl groups and therefore produce less steric hindrance during the inversion. Table 1 includes all of the inversion pathway characteristics for all thirteen forms of gossypol, including the torsion angle for each break and the maximum energy barrier.

All gossypol forms required a significant amount of energy for inversion, where gossypolone 3 required the least (14.5 kcal/mol) (Table 1). This energy barrier is too high to occur under normal conditions, and more energy such as heating, free radicals, or light is required to promote racemization. Additionally, all structures rapidly relaxed at specific angles during the inversion (Figure 3). The angle and maximal energy were not consistent across all forms studied, which reflects the impact of the molecular structure on the inversion.

Energy Barrier Influences

In general, oxygen groups *ortho* to the pivot bond had the greatest influence on the magnitude of the energy barrier, as typified by gossypol 3 versus gossypol 1. The hemiacetal in gossypol 3 pulled the oxygen group away from the pivot bond, thereby decreasing the energy barrier compared to the hydroxyl group in the aldehyde in gossypol 1. Gossypolone 1, which has *ortho* ketone groups instead of hydroxyl groups, had a smaller energy barrier since the ketone group poses less of a steric hindrance than the hydroxyl group. Furthermore, gossypolone is no longer a delocalized structure, allowing greater ring deformation with a smaller increase in energy.

Although the *ortho* substituents have the most impact upon the energy barrier, other factors also provide an influence, as shown with gossyopolone 1. Besides easier ring deformation due to a delocalized structure, the extent of hydrogen bonding appears to influence the energy barrier. For instance, the aldehyde tautomer (gossypol 1) had significantly different energy barriers than

the quinoid tautomer (gossypol 2). Unfortunately, whether hydrogen bonding or easier ring deformation had a more substantial impact is indistinguishable from the results.

As is evident in Table 1, many of the symmetric inversion pathways had very asymmetric energy barriers—even as great as 22 kcal/mol for the *cis* inversion of gossypol 2. The greater the energy barrier, the more asymmetric the barrier was. This implies that the molecule would prefer one enantiomer over another if the correct amount of energy is provided. It is unclear whether these differences are reflections of the actual molecule or are an artifact within MM3(2000).

Steric Contributions of Individual Clashes

As was demonstrated above, the clashes have a tremendous impact on the energy barrier preventing racemization. For each inversion pathway, two sets of the *ortho* substituents clash. Each clash can be isolated to determine its contribution to the overall energy barrier. To isolate an individual clash, the two clashing substituent groups can be maintained while replacing the other substituent groups with hydrogen atoms, thereby removing their steric contribution. By doing so, three clashes can be analyzed: the CH_3-CH_3 clash, the OH-OH clash, and the CH_3-OH clash. The inversion pathways were then simulated for these reduced molecules of gossypol 1, where the results are depicted in Figure 4. The OH-OH clash was overcome at the smallest torsion angle and produced the smallest energy barrier of 20.8 kcal/mol. Both the CH_3-CH_3 clash and the CH_3-OH clash had very similar passing torsion angles of about 36° and energy barriers of approximately 27 kcal/mol.

When comparing these results to that of gossypol 1, an additive nature of the individual clashes is observable for the *trans* clash. This clash, which involves two simultaneous CH_3-OH clashes, also occurred at 36°, the angle of the individual CH_3-OH clash, and an energy barrier of 52 kcal/mol, which is very close to twice that of the individual CH_3-OH clash. For the *cis* clash, the CH_3-CH_3 and OH-OH clashes occurred at different torsion angles, resulting in a stepwise inversion pathway. An additive nature is less clear, for the first and largest energy barrier is more than the sum of the individual CH_3-CH_3 and OH-OH energy barriers. Even the second energy barrier of 35 kcal/mol in the *cis* clash, which involves passing hydroxyl groups, is above the individual OH-OH energy barrier of 20.8 kcal/mol. During the *cis* inversion, the two clashes must alter the molecular structure in a way that requires more energy than the mere summation of the two individual clashes.

Discussion

The simulated inversion of different forms of gossypol has been useful in understanding the factors that influence the inversion. It is important to note that, in a gossypol solution, all tautomers are present, although in varying ratios depending on the solvent characteristics. Under normal conditions, none of the tautomers will racemize, but if the energy is increased, racemization will occur in one tautomer, while the others remain stable. Due to the reversible nature of tautomerization, a solution of gossypol could racemize even if specific tautomers do not. Within a single gossypol form, either the *trans* or *cis* inversion pathway would be preferred due to large differences in energy barriers, although which pathway is preferred varies.

Significant asymmetry for symmetric pathways was predicted by the calculations. This would imply that racemization can occur toward one enantiomer. This has not been reported, although the energy required is beyond what experiment has provided for gossypol (6). Whether or not it is an artifact of MM3(2000) is still unclear, although steps were taken to eliminate this possibility. Even though the torsion angle of the pivot bond was rotated 3°, angles as small as

0.5° were used with very similar results produced. Additionally, minimal structures with rotated hydroxyl groups had similar results compared to the related inversion pathway results.

The very nature of the driver algorithm could be causing artifacts, since the algorithm requires the selection of four atoms that make up the central dihedral angle. These atoms are frozen in space during minimization to preserve the dihedral angle, yet those bond lengths are frozen as well. When the frozen bonds are involved in the clash, the energy barrier and angle of the break may be irrevocably affected. This could contribute to the asymmetry observed. Furthermore, the naphthalene rings bend during the inversion, which means the dihedral angle is not the same for any four atoms selected. Other molecular modeling programs may be required that do not freeze the bond lengths. GAMESS (9), an *ab initio* molecular modeling program, will be used. Besides using quantum mechanics instead of molecular mechanics, GAMESS also can receive internal coordinates instead of Cartesian coordinates, which allows for freezing of dihedral angles without freezing bond lengths. This should provide a better characterization of the different gossypol forms, as well as validate the information presented here.

Acknowledgments

We thank Anthony Hill for his technical assistance with computer use and Mark Gordon for his helpful comments concerning GAMESS.

References

1. Segal, J.S., ed. Gossypol, a Potential Contraceptive for Men. Plenum, New York (1985).
2. Waller, D.P.; Zaneveld, L.J.D.; and Farnsworth, N.R. Gossypol: Pharmacology and current status as a male contraceptive. *Econ. Med. Plant Res.* **1**, 87–112 (1985).
3. Wu, Y.W.; Chik, C.L.; and Knazek, R.A. An *in vitro* and *in vivo* study of antitumor effects of gossypol on human SW-13 adrenocortical carcinoma. *Cancer Res.* **49**, 3754–3758 (1989).
4. Smith, F.H and Clawson, A.J. The effects of dietary gossypol on animals. *J. Am. Oil Chem. Soc.* **47**, 443–447 (1970).
5. Band, V.; Hoffer, A.P.; Band, H.; Rhinehardt, A.E.; Knapp, R.C.; Matlin, S.A.; and Anderson, D.J. Antiproliferative effect of gossypol and its optical isomers on human reproductive cancer cell lines. *Gynecol. Oncol.* **32**, 273–277 (1989).
6. Jaroszewski, J.W.; Strøm-Hansen, T; and Hansen, L.L. Optical stability of gossypol. *Chirality*, **4**, 216–221 (1992).
7. Freedman, T.B.; Cao X; Oliveira, R.V.; Cass, Q.B.; and Nafie, L.A. Determination of absolute configuration and solution conformation of gossypol by vibrational circular dichroism. *Chirality*, **15**, 196–200 (2003).
8. Dowd, M.K.; Thomas, L.M; and Calhoun, M.C. Crystal and molecular structure of an enatiomeric gossypol-acetic acid clathrate. *J. Am. Oil Chem. Soc.*, **76**, 1343–1350 (1999).
9. Schmidt M.W.; Baldridge, K.K.; Boatz, J.A.; Elbert, S.T.; Gordon, M.S.; Jensen, J.H.; Koseki, S.; Matsunaga, N.; Nguyen, K.A.; Su, S.J.; Windus, T.L.; Dupuis, M.; and Montgomery, J.A., Jr. The General Atomic and Molecular Electronic Structure System. *J. Comp. Chem.*, **14**, 1347–1363 (1993).

Table 1. Characteristics of the four inversion pathways for all thirteen forms of gossypol. Breaks occur when *ortho* substituent groups pass each other and the structure abruptly relaxes. If two breaks occur, the first break is when two hydroxyl groups pass, and the second break is when two methyl groups pass. Max E: maximal relative energy needed to cross energy barrier; Angle: torsion angle deviation from either 0° or 180° where the specified break occurs.

	(+) Enantiomer					(-) Enantiomer				
	Cis clash (180°)			*Trans* clash (0°)		*Cis* clash (180°)			*Trans* clash (0°)	
	Max E	Angle		Max E	Angle	Max E	Angle		Max E	Angle
Structure	kcal/mol	Break 1	Break 2	kcal/mol	Break	kcal/mol	Break 1	Break 2	kcal/mol	Break
Gossypol 1	52.6	27	39	51.7	39	58.2	33	39	51.6	36
Gossypol 2	57.8	33		49.2	27	35.2	36		53.5	42
Gossypol 3	31.2	24	33	41.7	36	33.0	15	33	40.6	36
Gossypol 4	37.5	9	39	48.9	36	57.8	33	39	57.1	39
Gossypol 5	40.9	18	33	38.3	27	49.7	27	36	45.5	39
Gossypol 6	48.0	27	33	48.3	33	31.2	33		40.0	30
Gossypolone 1	22.3	15		18.0	0	20.8	18		18.1	18
Gossypolone 2	24.7	15		14.7	18	26.1	18		15.5	0
Gossypolone 3	23.6	15		14.6	3	20.8	9	18	14.5	15
N-gossypol 1	53.6	36		45.7	21	41.1	3	48	47.5	42
N-gossypol 2	55.8	30		53.3	27	39.3	36		57.1	45
N-gossypol 3	56.0	30		51.3	30	38.3	6	36	54.0	42
Anhydrogossypol	30.3	15	33	37.2	33	30.4	33		34.7	30

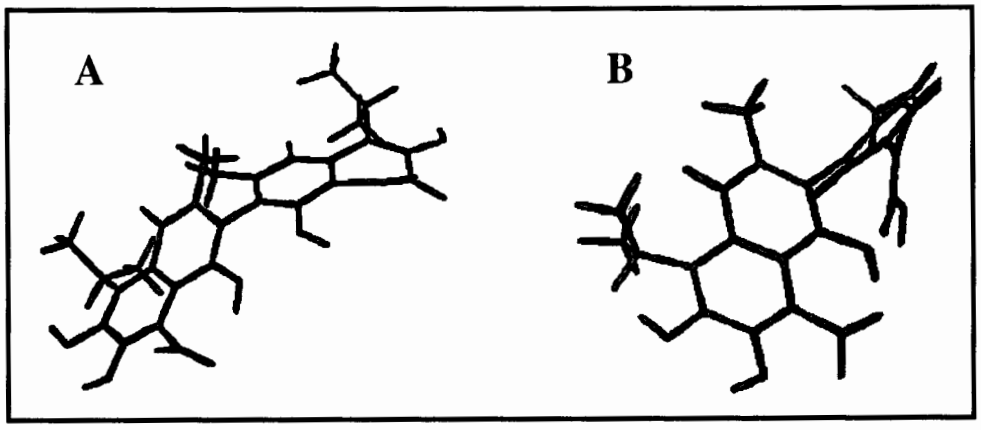

Figure 1. A: (–) enantiomer of gossypol; B: (+) enantiomer of gossypol, as previously assigned (7).

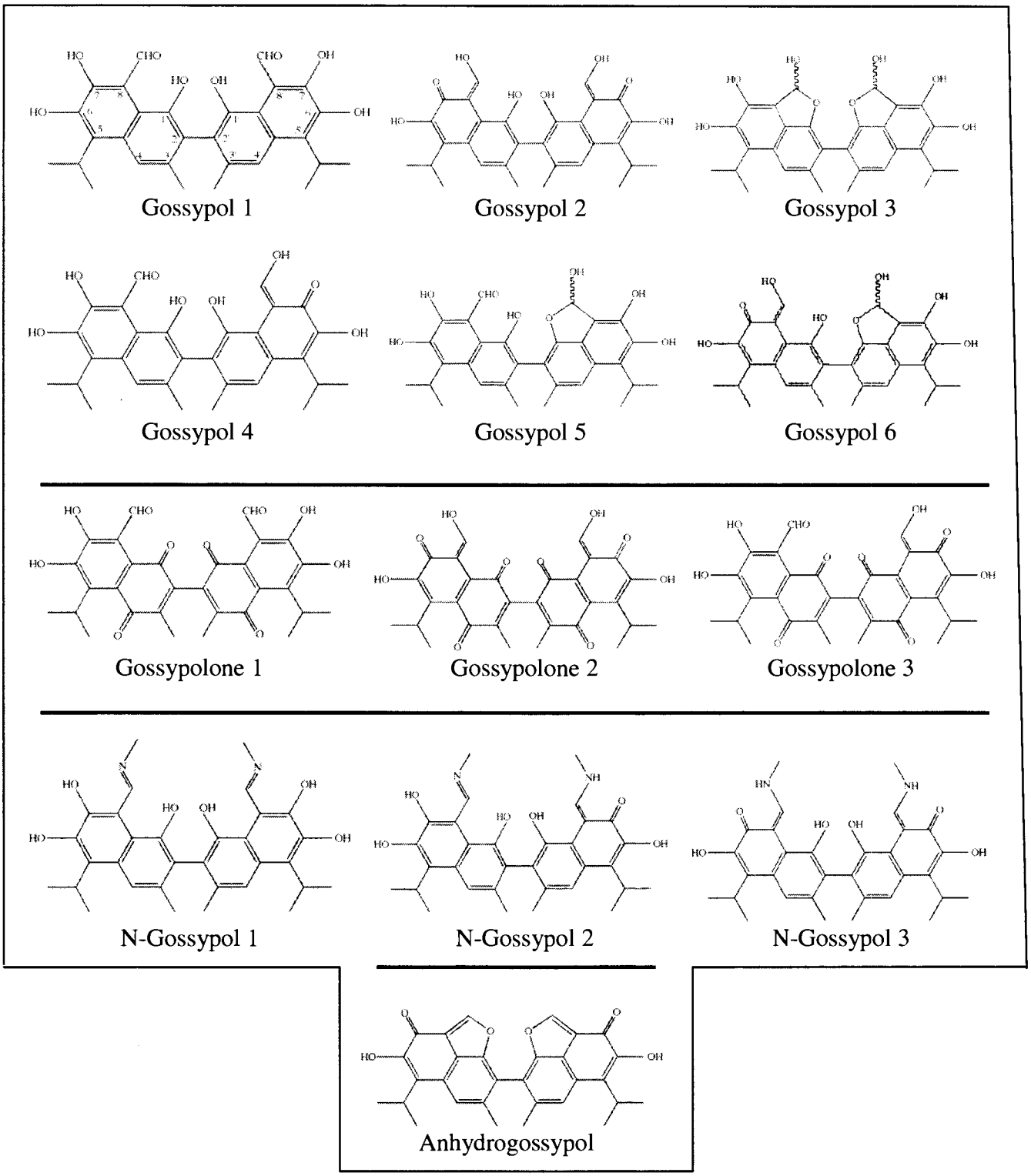

Figure 2. The thirteen forms of gossypol used in this study, which include six tautomers of gossypol, three of gossypolone, three of an amine-substituted gossypol derivative, and the one form of anhydrogossypol. The numbering system displayed with gossypol 1 is used for all other forms.

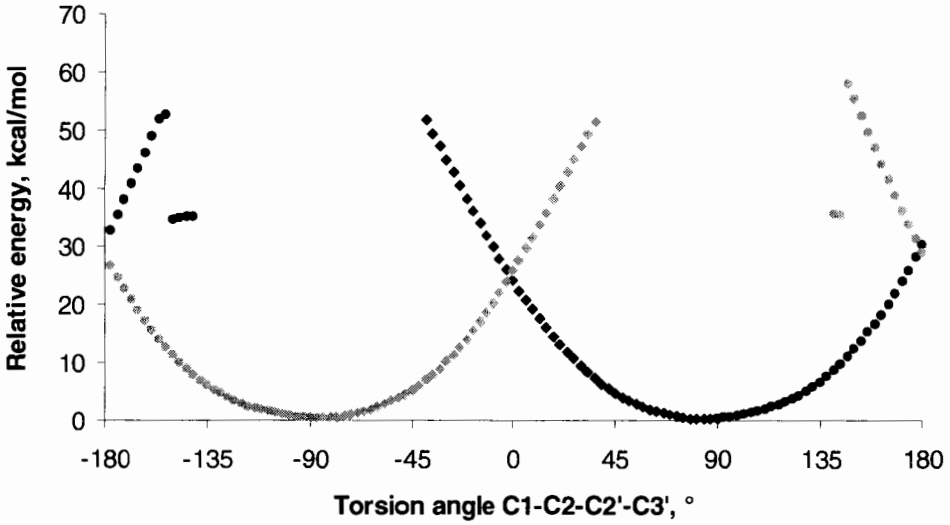

Figure 3. Calculated relative energies of gossypol 1 along all four inversion pathways. The torsion angle C1-C2-C2'-C3' was rotated in both the positive and negative directions starting at each minima, at approximately 90° and –90°. Gray dots represent inversion pathways from the (+) enantiomer to the (-) enantiomer, whereas black dots represent inversion pathways from the (-) enantiomer to the (+) enantiomer.

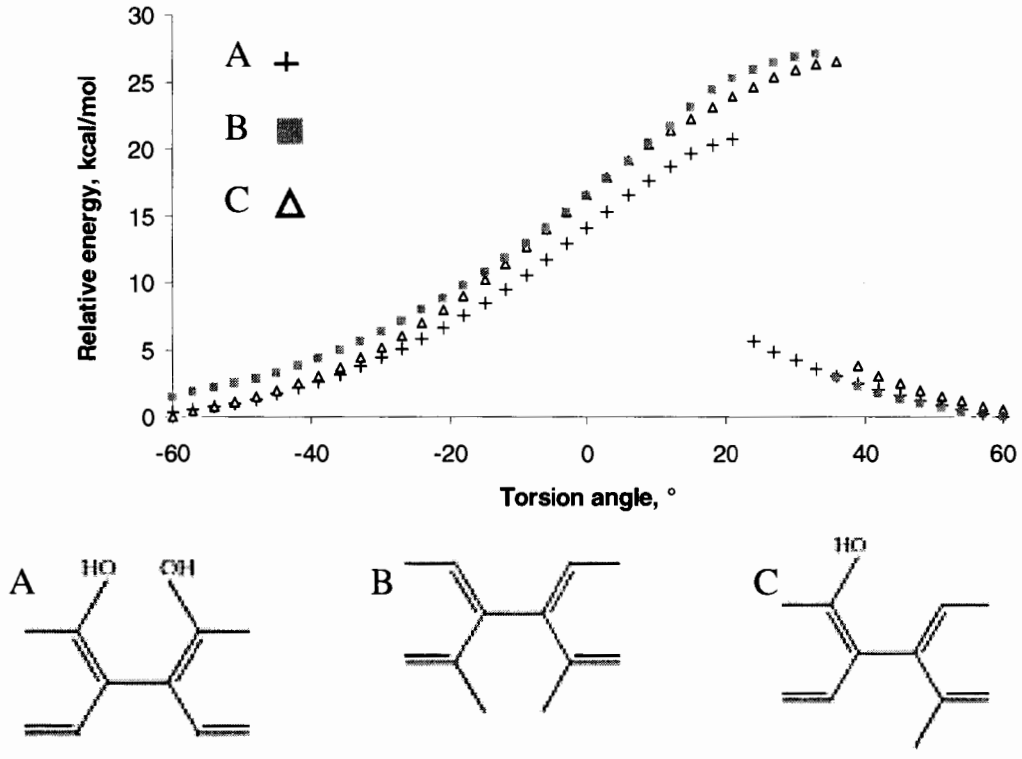

Figure 4. Influence of each clash, as demonstrated by reduced structures of gossypol 1. To focus on each clash, the other groups were replaced by hydrogen atoms. The clashes include OH-OH (A), CH_3-CH_3 (B), and CH_3-OH (C).

Production of Bacterial Cellulose by *Acetobacter xylinum* in Static Culture and Its Properties

Sasivimon Chittrakorn, Charles E. Walker, and Larry E. Erickson
Departments of Grain Science and Industry and Chemical Engineering, Kansas State University, Manhattan, KS 66506

Abstract

Production of bacterial cellulose by *Acetobacter xylinum* subsp. *sucrofermentans* in a medium containing glucose, yeast extract, peptone, citric acid, and mineral salts under static culture conditions was evaluated. Bacterial cellulose was produced as a white pellicle accumulated on the culture surface. The kinetics of *A. xylinum* was studied in test tubes containing 10 ml medium and in flasks containing 350 ml medium. Kinetic studies in 10 ml culture media showed that cellulose concentration increased to a maximum of 0.78 g/l dry basis at seven days of fermentation and the thickness of pellicle increased to a maximum at nine days of cultivation. With 350 ml of medium volume, the amount of cellulose and thickness of the pellicle increased as cultivation time increased. The estimated generation time of *A. xylinum* was 9.52 and 5.65 h for 10 ml and 350 ml of culture medium. The pH of the medium decreased as cultivation time increased in both experiments. Surface to volume ratio (S/V) affects the rate of cellulose production. The S/V ratio of 0.25 cm^{-1} gave the highest cellulose concentration (1.06 g/L). Unpurified *A. xylinum* cells observed by scanning electron microscopy were rods of about 1.6 μm length. Widths of bacterial cellulose ribbon were 24–98 nm. The cell concentration on the surface of the pellicle covered about 2–8 % of the photo area. The bacterial cellulose was produced at initial culture media pHs of of 5.0 and 6.0. Bacterial cellulose suspension prepared using a homogenizer was smooth and odorless. The water-holding capacities of the cellulose suspensions were 92.6 and 97.1 (g/g), respectively, and their viscosities were 193.3 and 220.0 poise, respectively.

Introduction

Cellulose, composed of anhydroglucose units joined by β-1,4 glycosidic bonds, is the most abundant polymer in nature. It is found as a structural component in the cell walls of plants, algae, and some bacterial genera such as *Acetobacter*, *Agrobacterium*, *Rhizobium*, and *Sarcina*. Microbial cellulose displays unique properties compared to plant cellulose. It is pure, without any lignin or other cell-wall contaminating material. Brown (1992) stated that microbial cellulose has much higher mechanical strength than pulp paper and cotton textiles and the cellulose is very hydrophilic, with a water absorption capacity over 100 times its weight.

Acetobacter species produce extracellular bacterial cellulose as a pellicle composed of ribbon-shaped fibrils less than 100 nm wide. *Acetobacter xylinum* is the most productive cellulose-producing bacterium. "A single cell of *A. xylinum* can polymerize 200,000 glucose molecules per second into β-1,4 glucan chains which, when extruded into the surrounding medium, form a single, twisted, ribbonlike bundle of microfibrils. The ribbon elongates in direct association with the cell envelope and remains associated during cell division" (Ross, 1991). Brown (1992) reported that six to eight glucan chains are required to form a crystalline microfibril, and microfibrils then aggregate by hydrogen bonding to form the ribbon secreted into the medium.

The mechanisms of pellicle formation from *A. xylinum* are considered as follows. Initially, bacteria increase their population by growing aerobically and producing cellulose in the entire liquid phase. The increase in the turbidity of liquid phase can be observed during this stage.

When dissolved oxygen is exhausted, cell growth and cellulose production occur in a narrow zone at the air/medium interface. "The cellulose pellicle floats on the top of the liquid, and the cellulose produced is pushed down in the course of time, while new cellulose layers are continually built on top of the older cellulose" (Verschuren et al., 2000; Iguchi, et al., 2000).

A. xylinum is strictly an aerobic organism. Production of cellulose from this strain is affected by the type of sugar, pH, and nitrogen sources. Many carbon substrates can be used for cellulose production. Glucose and sucrose are generally used as carbon sources (Vandamme et al., 1998., Masaoka et al., 1993). The optimal pH range of *A. xylinum* is 4.0–7.0 and the optimal growth temperature is 25–30°C (Jonas and Farah, 1998). Two typical fermentation methods, static and agitated culture, have been used for cellulose production. Cellulose ultrastructure and its mechanical and physical properties vary depending on the culture method (Krystynowicz et al., 2002). The static culture produces cellulose in the form of a gelatinous membrane. In agitated culture, the cellulose is accumulated in a dispersed suspension. The formation of a gelatinous membrane is inhibited by shear stress during the agitation of the culture medium, and this results in the accumulation of small aggregates of cellulose (Toyosaki et al., 1995).

Growth rate of the cells under static culture conditions is slow. The pellicle at the air/liquid interface forms a permeable barrier between the atmospheric oxygen on the upper side and the nutrients on the lower side (Dudman, 1960). Some investigators have tried to improve the production of bacterial cellulose in static cultures. Okiyama et al. (1992) produced bacterial cellulose in a two-stage fermentation process. The first stage accelerates the cell growth using an airlift fermenter and the second stage improves the formation of cellulose by culturing the bacterial cells in static culture. Cellulose synthesis occurs in the logarithmic growth and stationary phases. Einfeldt and Klemm (1997) stated that the generation time of *Acetobacter* species was about 8 h. Cellulose production varies with the dimensions of the culture pans and the culture medium composition. The optimal surface to volume ratio (S/V) also affects cellulose production (Krystynowicz et al., 2002).

The properties of cellulose produced from *A. xylinum* are unique. They include good mechanical strength and high water absorption capacity, high crystallinity, and an ultra-fine fiber network structure. A comparison of the bacterial cellulose produced by the static and agitated culture methods shows that the crystallinity, the cellulose I_α content, and the degree of polymerization of the cellulose in agitated culture are lower than that in static culture (Yoshinaga et al., 1997). Bacterial cellulose produced by static cultivation displays a higher Young's modulus and tensile strength than that from agitated culture. However, the value of water-holding capacity is lower. Bacterial cellulose can be applied in many areas because the product has high purity with a crystalline structure. There are many products that could be manufactured from bacterial cellulose including dessert (nata de coco), sausage and meat casing, wound-care dressings, acoustic diaphragms, and artificial skin substrate (Jonas and Farah, 1998; Yoshinaga et al., 1997). Bacterial cellulose has many potential uses. The objectives of this study were to 1) produce the bacterial cellulose in static culture system, 2) understand the kinetic aspects of bacterial cellulose in static culture, and 3) evaluate the properties of the bacterial cellulose produced.

Materials and methods

Microorganism

A. xylinum subsp. *sucrofermentans* ATCC 700178 was used. The stock culture was grown by transfer of 1 ml of the culture into test tubes containing 9 ml of YGC medium. The YGC media consists of 50 g of glucose, 5 g of yeast extract, and 12.5 g of $CaCO_3$ dissolved in 1 l of distilled

water. The tubes were incubated at 26°C for 72 h. After incubation, a loopful of suspension was streaked onto YGC agar plate. The agar plate was kept at 10°C as a stock culture for bacterial cellulose production.

Culture medium

The culture medium was prepared according to the procedure of Toyosaki et al. (1995). Buffered Schramm & Hestrin's medium (BSH medium), comprised of 2.0 % (w/v) glucose, 0.5 % (w/v) yeast extract, 0.5 % peptone, 0.27% (w/v) Na_2HPO_4, and 0.115% (w/v) citric acid in H_2O was prepared, and the pH of the media was adjusted to 5.0.

Production of bacterial cellulose

Bacterial cellulose was produced by culturing *A. xylinum* in static culture. The seed broth was prepared by adding a loopful of stock culture on the agar plate to a 100-ml Erlenmeyer flask containing BSH medium and incubating at 30°C without shaking for three days. The seed culture was shaken vigorously to remove the cells from the gelatinous membrane, and 1 ml of cell suspension was inoculated into a 25-mm diameter test tube containing 10 ml of BSH media. The culture was incubated at 30°C for 14 days. An inoculum containing 32 ml of cell suspension was transferred into a 300-ml Erlenmeyer flask, which was subsequently filled so that it contained approximately 350 ml of media. The static culture was incubated at 30°C for 17 days. To purify the cellulose, the culture broth was washed three times with distilled water to remove residual medium components and then treated with 0.1 N NaOH at 80°C for 20 min to dissolve the bacterial cells. The cellulose was finally washed three times with distilled water and filtered through filter paper.

The number of viable organisms (CFU/ml), glucose concentration (g/L), pH, and dried cell weight (g/L) of the culture broth were measured. The wet weight of the pellicle and its thickness in mm were also measured. After purification, the cellulose concentration was determined. The specific growth rate constant (μ) and generation time (g) were calculated. The morphology of bacterial cellulose (before purification) produced in 10 ml media at pH 5.0 was studied by using a scanning electron microscope (S-3500 N, Hitachi Ltd.). Bacterial cellulose samples were critical-point dried (Samdri-790B, Tousimis Research Corp., Rockville, MD) and then coated with gold before using the scanning electron microscope.

The effect of medium volume on the properties of cellulose produced

The bacterial cellulose was produced by static culture as described above. An inoculum of 10 % of the culture volume was added to several 25-mm diameter test tubes containing 10, 20, and 30 ml of BSH media and incubated for 7 days at 30°C. The method for purification of the bacterial cellulose was as described above. After harvesting the cellulose from the culture broth, the thickness in mm of the pellicle was measured. The dried weight of the cellulose was analyzed after purification and the surface area per unit volume was calculated.

Properties of bacterial cellulose

The seed broth was prepared by adding a loopful of stock culture to 10 ml BSH culture medium in a test tube. Culture media of pH 5.0 and 6.0 were prepared. The samples were then incubated without shaking at 30°C for three days. The seed culture was shaken vigorously to remove the cells from the gelatinous membrane, and the cell suspension was inoculated into 100 ml of BSH medium in a 110-mm diameter petri dish and covered with a lid. The culture was incubated at 30°C for seven days in the incubator. To prevent contamination, the surface of incubator was

cleaned with 95 % alcohol before incubation of the culture. To purify the cellulose, the culture broth was washed three times with distilled water to remove residual medium components and then treated with 0.1 N NaOH at 80 °C for 20 min to dissolve the bacterial cells. The gelatinous cellulose was finally washed three times with distilled water. The amount and thickness of the pellicle were measured according to the method described above. Three replications of bacterial cellulose were produced.

Preparation of bacterial cellulose suspension and investigation of its properties

Gelatinous cellulose prepared at starting media pHs of 5.0 and 6.0 was added to distilled water at a 1:2 (w/w) ratio of wet weight of cellulose to water. Each sample was disintegrated with a Power Gen 700 homogenizer (Fisher Scientific) at 30,000 rpm for 1 min. The viscosity of bacterial cellulose suspension after disintegration with the homogenizer was measured using a Brookfield viscometer and water-holding capacity of the suspension was determined.

Results and discussion

A. xylinum produces cellulose in the form of a pellicle located at the surface of the culture medium. The kinetics of *A. xylinum* were studied in test tubes containing 10 ml media and in flasks containing 350 ml media. Figure 1 shows the kinetics of *A. xylinum* in 10 ml static culture. The pH of the medium decreased from 4.64 to 3.04 from day 0 to day 14. A cellulose pellicle can be observed after two days of cultivation. During the 14 days of fermentation, the amount of cellulose increased to a maximal amount of 0.78 g/L dry basis at seven days of fermentation and then decreased, which indicates that some of the cellulose may have been hydrolyzed in the later time. The wet weight of the pellicle before purification at seven days was about 0.29 g. The thickness of the pellicle increased up until nine days of cultivation and then decreased with the maximum at 9 days of 1.1 mm.

The bacteria did not synthesize cellulose until they passed through the rapid growth or log phase. After two days of cultivation the growth phase changes to stationary phase and this is maintained until 11 days (Fig. 1). The maximal concentration of cellulose occurred during the stationary phase, and this result agrees with Einfeldt and Klemm (1997), who reported that cellulose formation occurs mainly in the stationary phase where oxygen availability limits growth. The growth rate constant (μ) and generation time (g) of *A. xylinum* in 10 ml test tube were 0.073 h^{-1} and 9.52 h, respectively, for one 24-h period.

Glucose concentration decreased as the fermentation time increased (Fig. 1). It tended to decrease sharply during the first four days of cultivation, with 58% utilization of glucose and a resulting concentration of bacterial cellulose of approximately 0.3 g/L. The results in Figure 1 suggest that cellulose production may have stopped after seven days because of the limited availability of glucose in the upper portion of the pellicle. The cell yield at seven days of cultivation, calculated as a ratio of g dry cell weight per g of glucose consumed, was 0.23 and the product yield, calculated as a ratio of g cellulose per g of glucose consumed, was 0.05.

Figure 2 shows the kinetics of *A. xylinum* in static culture with 350 ml of medium volume. The pH of the culture medium decreased from 4.59 to 3.61 as cultivation time increased. The amount of cellulose and thickness of the pellicle also increased. The wet weight of pellicle before purification at seven days was about 1.77 g. The cell yield and product yield at seven days of cultivation calculated as mentioned above were 1.36 g cell dry weight/g glucose consumed and 0.01 g cellulose per g glucose consumed, respectively.

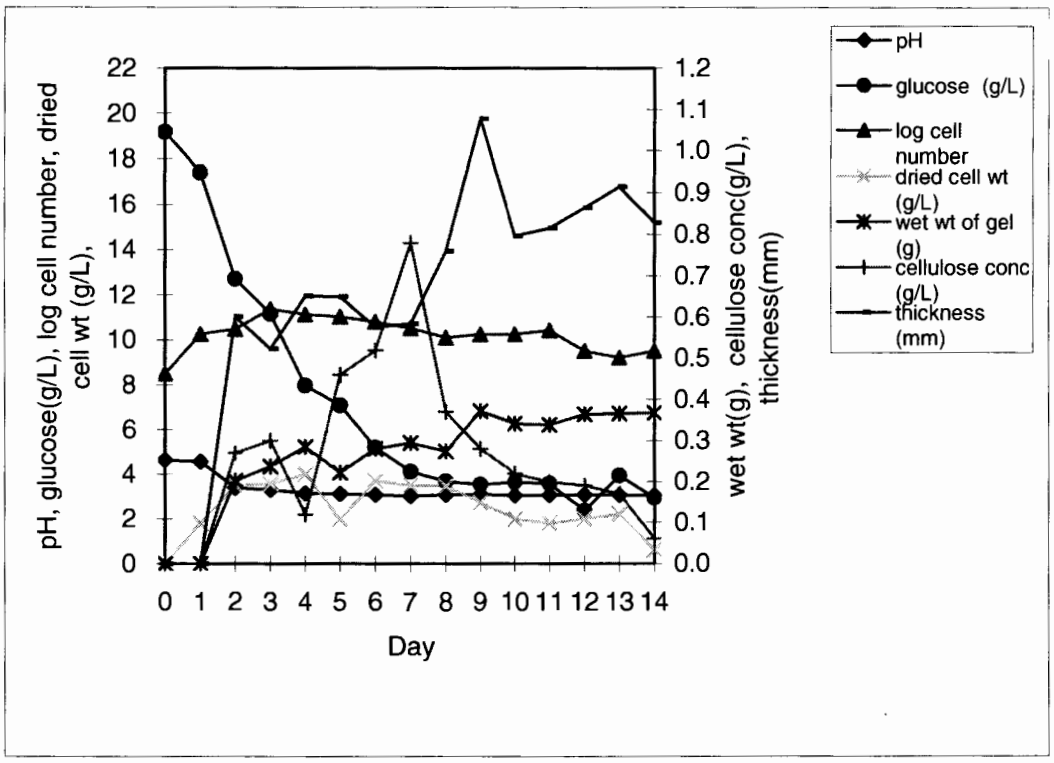

Figure 1. Kinetics of *A. xylinum* in static culture with 10 ml medium volume. Values are the means of duplicate measurements.

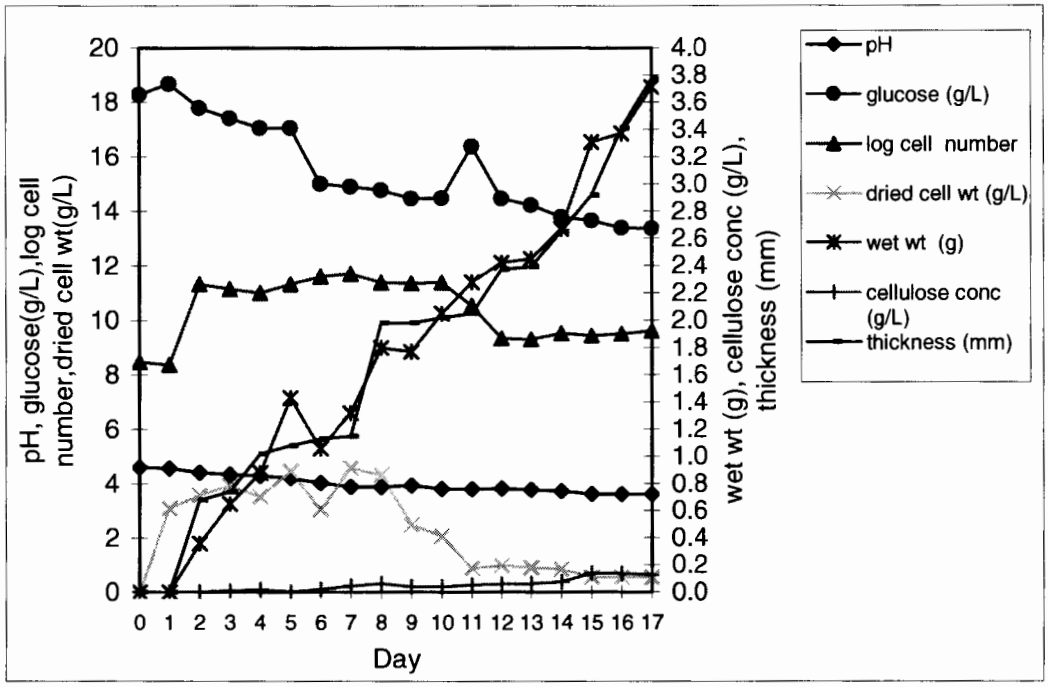

Figure 2. Kinetics of *A. xylinum* in static culture with 350 ml medium volume. Values are the means of duplicate measurements.

Values of μ and *g* of *A. xylinum* in 350 ml culture medium were 0.123 h^{-1} and 5.65 h, respectively. Comparison between the cases of 10 ml and 350 ml culture media shows that the generation time with 350 ml media is less than that for 10 ml of media. Einfeldt and Klemm (1997) reported that generation times of *Acetobacter* species are about 8 h. The result is similar to the values of 9.52 and 5.65 hr for the data in Figures 1 and 2, respectively.

Glucose concentration decreased moderately over time in the 350 ml experiment. At 15 days of cultivation, the amount of cellulose tended to decrease even though the system still had some available glucose (13.38 g/L). Verschuren et al. (2000) stated that when the sucrose concentration at the interface approaches the saturation constant, K_s, the reaction rate as well as the flux will decrease. As a result, the cellulose production rate gradually decreases over time. In the later stage of fermentation, the carbon substrate will become limiting due to the transport distance of sucrose to the 50–100 μm active reaction zone at the top of the pellicle. The final ratio of glucose concentration to pellicle thickness is about 3.3 and 3.5 g/l-mm for Figures 1 and 2. Thus, the diffusion gradient in the pellicle is about the same for both cases at the end of the experiment.

A scanning electron micrograph of unwashed bacterial cellulose (Figure 3) shows the bacterial cells as rods about 1.6 μm long. The ribbon has a reticulated structure composed of ultrafine microfibrils. Ribbon widths are 24–98 nm, agreeing with Yoshinaka (1997), who reported that BC ribbons are about 100 nm wide and 3–8 nm thick, and that each ribbon is composed of a number of microfibrils. It was estimated that the upper layer of the pellicle consists of approximately 10 % wet cells. The corresponding log cell number of viable cells in the oxygen penetrated zone at seven days of cultivation would be about 10 (Verschuren et al., 2000). From this experiment, the scanning electron microscope study of cell concentration at the surface of the pellicle shows that the cell concentration covers about 2 to 8 % of the photo area, which approximately agrees with the previous estimation (Verschuren et al., 2000).

Effect of medium volume on the properties of cellulose produced

The effect of area per unit volume (*S/V*) on the concentration of bacterial cellulose is illustrated by the data in Table 1. The area exposed to the gas phase and the volume of the media in the static culture affects the amount of bacterial cellulose produced. The results show that the best surface area per volume ratio is 0.25 cm^{-1}, which gave the highest concentration of cellulose (g dry cellulose/l medium. The 20 ml volume with $S/V = 0.25$ cm^{-1} also has the highest amount of cellulose produced (21.2 g) compared to 15.6 g and 1.8 g for the 30- and 10-ml cases, respectively. The yield per g of glucose supplied is largest for the 20-ml case. Krystynowicz et al. (2002) reported that surface per volume ratio of 0.71 cm^{-1} gave the best yield of cellulose (3.5 g/L). Masaoka et al. (1993) reported that at constant surface area, culture volume and depth did not influence bacterial cellulose production and the production increased with surface area.

Properties of the cellulose suspension

Bacterial cellulose for food use was prepared at initial culture medium pHs of 5.0 and 6.0. The bacterial cellulose suspension was prepared by homogenizing the cellulose pellicle in distilled water for 1 min at a 1:2 ratio of wet cellulose:water. It was smooth, opaque and odorless. Table 2 shows its concentration, thickness of the bacterial cellulose pellicle, and properties. The concentration of cellulose produced at pH 6.0 is significantly higher than that at pH 5.0 ($p < 0.05$). Water-holding capacity was expressed as the amount of retained water per gram dry solid matter. The water holding capacity produced at pH 5.0 and 6.0 was 92.6 and 97.2 (g/g) respectively. There is no significant difference between the water holding capacity with pH of culture

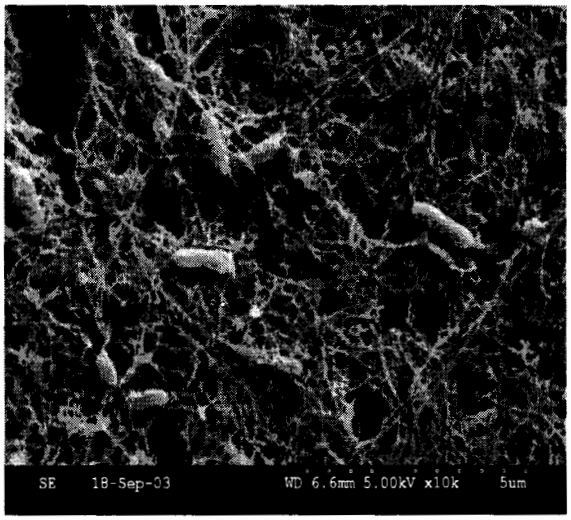

Figure 3. Scanning electron micrograph on the surface of unpurified cellulose pellicle produced by static culture using BSH media with initial pH of 5.0 and cultivated for seven days.

Table 1. Effect of *S/V* on the production of bacterial cellulose in static culture at seven days of fermentation.[a]

Medium volume (ml)	Surface area $(cm)^2$	S/V (cm^{-1})	Gel thickness (cm)	BC concentration (g/L)
10	4.91	0.49	0.059 ± 0.01	0.78 ± 0.18
20	4.91	0.25	0.098 ± 0.15	1.06 ± 0.05
30	4.91	0.16	0.121 ± 0.04	0.52 ± 0.30

[a] Means of three replications ± standard deviation.

media at the 95 % confidence level. The bacterial cellulose suspension for both of the initial values of pH of the culture media exhibited high water holding capacity due to the network structure of microfibrils. The three-dimensional network structure is formed when cellulose microfibrils connect to each other. As a result bacterial cellulose has a good ability to hold water and develop viscosity (Omoto et al, 2000). The viscosity and water holding capacity followed the same trend. The viscosity of cellulose suspensions produced at different values of pH is not significantly different ($p > 0.05$).

Table 2. Cellulose yield, thickness and properties of bacterial cellulose suspension produced with the culture medium pH at 5.0 and 6.0 [a]

pH	Cellulose conc (g/L)	Thickness of gel (mm)	Water holding capacity (g/g)	Viscosity (p)
5.0	0.37 ± 0.08 [a]	0.56 ± 0.09 [a]	92.62 ± 7.0 [a]	193.3 ± 3.0 [a]
6.0	0.63 ± 0.04 [b]	0.57 ± 0.01 [a]	97.17 ± 9.0 [a]	220.0 ± 2.0 [a]

[a] Means of three replications ± standard deviation. Means in columns with the same letter are not significantly different ($p > 0.05$).

Conclusions

In static culture, *A. xylinum* produced cellulose at the upper surface of the culture media after the exponential growth phase. The pellicle could be observed after two days of fermentation and the maximal concentration of cellulose occurred in the stationary phase of growth. Cellulose production decreased at long fermentation times because of the low availability of glucose in the upper part of the pellicle in the later stage of fermentation. The glucose concentration gradients in the pellicle were similar in magnitude at the end of the fermentation in both cases.

Values of *S/V* affected cellulose production. An *S/V* of 0.25 cm^{-1} in the test tube containing 20 ml of culture medium gave the highest concentration of cellulose. The *A. xylinum* cells observed by scanning electron microscopy were rods of 1.6 μm length. Bacterial cellulose ribbons were 24–98 nm long. The cell concentration on the surface of the pellicle covered about 2–8 % of the photo area.

The bacterial cellulose suspension exhibited high water-holding capacity due to the network structure of microfibrils which have a good ability to hold water and develop viscosity.

References

Brown, R.J. 1992. Emerging technologies and future prospects for industrialization of microbially derived cellulose. Harnessing biotechnology for the 21st Century. Proceedings of the Ninth International Biotechnology Symposium and Exposition, Crystal City, VA. 76–79.

Dudman, W.F. 1960. Cellulose production by *Acetobacter* strains in submerged culture. J. Gen. Microbiol. 22: 25–39.

Einfeldt, L., and Klemm, D. 1997. The control of cellulose biosynthesis by *Acetobacter xylinum* in view of molecular weight and molecular weight distribution. Part I. Change of molecular weight of bacterial cellulose by simple variation of culture conditions. J. Carbohydr. Chem. 16: 635–646.

Iguchi, M., Yamanaka, S., and Budhiono, A. 2000. Review: Bacterial cellulose, a masterpiece of nature's arts. J. Mat. Sci. 35: 261–270.

Jonas, R., and Farah, L.F. 1998. Production and application of microbial cellulose. Polymer Degrad. Stabil. 59: 101–106.

Krystynowicz, A., Czaja, W., Wiktorowska-Jezierska, A., Goncalves-Miskiewicz, M., Turkiewicz, M., and Bieleck, S. 2002. Factors affecting the yield and properties of bacterial cellulose. J. Indust. Microbiol. Biotechnol. 29: 189–193.

Masaoka, S., Ohe, T., and Sakota, N. 1993. Production of cellulose from glucose by *Acetobacter xylinum*. J. Ferment. Bioeng. 75: 18–22.

Okiyama, A., Shirae, H.., Kano, H., and Yamanaka, S. 1992. Bacterial cellulose I. Two stage fermentation process for cellulose production by *Acetobacter xylinum*. Food Hydrocoll. 6: 471–477.

Omoto, T., Uno, Y., Asai, I., and Gen, S. 2000. Bacterial cellulose, In Handbook of Hydrocolloids. Phillips, G., and Willium, G.O. (eds.). CRC Press., Boca Raton, FL. pp. 321–330.

Ross, P., Mayer, R., and Benziman, M. 1991.Cellulose biosynthesis and function in bacteria. Microbiol. Rev. 55: 35–58.

Schramm, M., and Hestrin, S. 1954. Factors affecting production of cellulose at the air/liquid interface of a culture of *Acetobacter xylinum*. J. Gen. Microbiol. 11: 123–129.

Toyosaki, H., Kojima, T., Seto, A., Matsuoka, M., Tsuchida, T., and Yoshinaga, F.1995. Screening of bacterial cellulose-producing *Acetobacte*r Strains suitable for agitated culture. Biosci. Biotechnol. Biochem. 59: 1498–1502.

Vandamme, E.J., De Beats, S., Vanbaelen, A., Joris, K., and De Wulf, P. 1998. Improved pro-

duction of bacterial cellulose and its application potential. Polymer Degrad. Stabil. 59: 93–99.

Verschuren, PG., Cardona, T.D. Robert, M.J. Goolier, K.D. and Van Den Heuvel, J.C. 2000. Location and limitation of cellulose production by *Acetobacter xylinum* established from oxygen profiles. J. Biosci. Bioeng. 89: 414–419.

Yoshinaga, F., Tonouchi, N and Watanabe, K.1997. Research progress in production of bacterial cellulose by aeration and agitation culture and its application as a new industrial material. Biosci. Biotechnol. Biochem. 61: 219–224.

A Better Global Resolution Function and a Novel Iterative Stochastic Search Method for Optimization of HPLC Separation

Yandi Dharmadi[1] and Ramon Gonzalez[1,2]
Departments of Chemical Engineering[1] and Food Science and Human Nutrition[2]
Iowa State University, Ames, IA 50011

Abstract

HPLC optimization strategy consists of four elements; experimental design, retention modeling, quality criteria function, and optimal search method. In this paper we present a simple, superior alternative to general classes of classical resolution functions (S function) and a novel optimal search algorithm (ISS, iterative stochastic search) for HPLC optimization. Comparison of S with general classes of quality criteria functions (R_s, R_p, R_{min}) shows superior features such as lower error propagation rates, preservation of individual peak pair contributions, elimination of arbitrary cut-off values, and a unique capability to interpret absolute significance of function values through a simple integer inequality. The proposed ISS algorithm is more robust than standard methods and it is easily applicable to hyperdimensional optimization. ISS also shows clear advantages in its ability to correctly identify the global optimum (instead of the local optimum), with higher precision, with more efficient use of computation cycles, and with easier implementation. Successful application of S and ISS to HPLC optimization was demonstrated in the separation of representative functionalities (sugars, alcohols, organic acids) present in microbial fermentations. Both the optimal and pathological (worst) conditions were successfully predicted and experimentally verified.

1. Introduction

A common objective in HPLC method development is optimization, which is identification of operating conditions (e.g., mobile phase composition, pH, column temperature) that result in the best peak separation. The general strategy for optimization consists of four consecutive but independent elements: design of experiment, retention modeling, quality criteria function, and optimal search method. The use of experimental design allows for efficient sampling of the parameter space, while retention modeling provides a continuous representation of peak positions throughout the parameter space.

Before optimization begins, a quality criteria or objective function must be defined to reflect the quality/desirability of the separation. Many quality criteria functions have been used in HPLC optimization, but the pairwise resolution function is probably the most popular:

$$R_{i,j} = \frac{t_j - t_i}{\left(\frac{w_i}{2} + \frac{w_j}{2}\right)} \tag{1}$$

where t_i is retention time of peak i and w_i is width of peak i in units of time. Assuming peak symmetry, $R_{i,j} = 1$, means peaks i and j are barely separated. As it is not necessary to consider non-adjacent pairs i and j in the chromatogram, the global resolution function is defined as [1]:

$$R_p = \prod_{i=1}^{n-1} R_{i,i+1} \tag{2}$$

where n is the total number of peaks, and $i = 1$ to n is peak index in order of appearance in the chromatogram. The significance of R_p is that it reaches a maximum when all the peaks are most

evenly spaced. In fact, if the t_i's are independent variables and all w_i's are equal, R_p will reach a maximum when all adjacent peaks are exactly equidistant.

Optimal search methods used in HPLC separation can be broadly categorized into graphical and numerical methods. Graphical methods such as the window diagram [2] and overlapping resolution map [3] provide a visual representation of how the quality criteria function changes over the variable domain, from which the optimum is easily identified. In general, this can be achieved by contour (2D) or surface (3D) plots. Optimum identification by visual inspection or "eyeballing" should give rather good accuracy. However, numerical methods offer higher precision, as well as the ability to tackle higher-dimensional optimizations.

In this paper we describe a novel quality criteria function that is simpler but superior to other $R_{i,j}$ -based functions, as well as a novel optimal search algorithm that is more robust than current standards and is easily applicable to hyperdimensional optimization problems. Along with statistical experimental design and retention modeling, these new elements were utilized in the optimization of temperature, flow rate, and mobile phase concentration in HPLC separation of representative functionalities (e.g., sugars, alcohols, organic acids) commonly present in microbial fermentation. Comparison of the new approach to established methods is given. As an aid to method development, a computer program was written for the execution of the search algorithm.

2. Materials and methods

Experiments were run on a Waters (Milford, MA) HPLC system consisting of an in-line degasser AF, gradient pump 1525 with column heater, autosampler 717plus, refractive index detector 2410, and a PC with Empower® software for data acquisition. An HPX-87H column with Aminex® resin (sulfonated divinylbenzene-styrene copolymer) was used with a cation H pre-column cartridge (Bio-Rad, Hercules, CA). Deionized water for the mobile phase and needle wash was purified using a Nanopure II system (Barnstead, Dubuque, IA) to a conductivity of 18 MΩ-cm and filtered through a 0.2-μm membrane (Millipore, Billerica, MA). Isocratic elution for all runs was achieved using dilute sulfuric acid solutions as mobile phase.

Eighteen analytes (glucose, xylose, arabinose, glycerol, 1,2-propanediol, ethanol, acetic acid, formic acid, lactic acid, succinic acid, malic acid, fumaric acid, citric acid, oxaloacetic acid, α-ketoglutaric acid, pyruvic acid, phosphate, and LB medium) were included in the analyses, representing sugar, alcohol, organic acid functionalities and growth medium ingredients commonly present in microbial fermentation broths. Injection volume was 10 μl for all runs. The column was equilibrated for at least 2 h every time changes are introduced in temperature, flow rate, or mobile phase composition. The chromatogram of LB medium contains many small peaks and four major peaks – these four peaks are treated as separate compounds, bringing the total to 21 compounds for analysis.

An orthogonal, central composite design is used to formally define the parameter space with temperature (T), flow rate (F), and sulfuric acid concentration in the mobile phase (C) as independent variables. Boundaries of the experimental domain are defined by instrument ratings and practical considerations. (T_{min} = 25 °C, T_{max} = 60 °C, C_{min} = 0.5 mM, C_{max} = 30 mM, F_{min} = 0.3 ml/min and F_{max} = 0.6 ml/min).

Scaled variables x, y, and z are normalized temperature, flow rate, and concentration:

$$x = 1.2872 \cdot \left(\frac{2T - T_{max} - T_{min}}{T_{max} - T_{min}} \right) \tag{3}$$

$$y = 1.2872 \cdot \left(\frac{2F - F_{max} - F_{min}}{F_{max} - F_{min}} \right) \quad (4)$$

$$z = 1.2872 \cdot \left(\frac{2C - C_{max} - C_{min}}{C_{max} - C_{min}} \right) \quad (5)$$

Eqs. (3) to (5) show that the scaled variables take on values in the range of −1.2872 to 1.2872 according to orthogonal design ($\alpha = 1.2872$).

Retention time for each compound (in min) is modeled directly as a function of x, y, and z with a quadratic model:

$$t_k(x, y, z) = a_k + b_k x + c_k y + d_k z + e_k xy + f_k xz + g_k yz + h_k x^2 + i_k y^2 + j_k z^2 \quad (6)$$

where k is the compound index, and a_k to j_k are coefficients for linear (x, y, z), quadratic (x^2, y^2, z^2), and interactions effects (xz, yz, xz) of / among temperature, flow rate, and concentration. Values for the coefficients (a to j) were obtained by model fitting using JMP 5.0.1 software (SAS Institute, Cary, NC).

3. Results and discussion

3.1. Introduction and characterization of a novel quality criteria function

In this work an alternative to the classical global resolution function is proposed. The function is based on the pair-wise resolution $R_{i,j}$ described in Eq. (1), only that the reciprocal is used:

$$R_{i,j}' = \frac{\left(\frac{w_i}{2} + \frac{w_j}{2} \right)}{t_j - t_i} \quad (7)$$

Accordingly, the global resolution function here is defined as the sum of $R_{i,j}'$:

$$S = \sum_{i=1}^{n-1} R_{i,i+1}' \quad (8)$$

where i = 1 to n is peak index in order of appearance in the chromatogram. To our knowledge, such global resolution function has never appeared in the literature on HPLC optimization and therefore merits thorough evaluation. It should be noted that many quality criteria functions based on the sum of $R_{i,j}$ (not $R_{i,j}'$ as used here) have been reported [3, 4]. In the simplest case, these functions take the following form:

$$R_s = \sum_{i=1}^{n-1} R_{i,i+1} = \sum_{i=1}^{n-1} \frac{t_{i+1} - t_i}{\left(\frac{w_{i+1}}{2} + \frac{w_i}{2} \right)} \quad (9)$$

It is obvious that in the special case where all w_i's are equal, R_s collapses to $(t_n - t_1)/w$, i.e., the inner peaks totally lose their significance. Therefore, we believe that such functions should not be used for HPLC optimization.

With R_s-based functions, there is a need to limit the contribution of very well-separated pairs. This is not necessary for S, as well-separated pairs actually contribute the least. Each term in Eq. (8) can be thought of as punitive. If a pair is well-separated, its contribution is insignificant compared to the penalty due to an overlapping pair. There is no need for an arbitrary 'cut-off'

value; peak pair contributions nicely balance themselves due to hyperbolic decay with respect to peak separation/distance.

Comparing S with R_p shows that the characteristic property is retained, i.e., S also reaches an extremum (a minimum in this case) when all the peaks are most evenly spaced. Unlike R_p, however, information on individual pair-wise contributions is conserved in S. This is because each additive term in Eq. (8) is a positive number, whereas if the logarithm is applied to R_p in Eq. (2),

$$\log R_p = \sum_{i=1}^{n-1} \log R_{i,i+1} \tag{10}$$

the additive terms could be positive or negative, hence the "masking" effect. As mentioned before, this problem could be avoided by only considering the worst-separated pair ($R_{\min}$ [5] or $\alpha_{\min}$ [6]) at the risk of losing critical information. Such sacrifice is not necessary with S, as all peak pairs do contribute without the masking effect.

It is instructive to compare S and R_p from the standpoint of error propagation. Suppose there are only two terms in Eq. (2), x and y, and standard deviations for x and y are known, i.e., σ_x and σ_y (these can be obtained from error estimates in the model fitting). Thus $R_p = xy$ and $S = 1/x + 1/y$. The standard deviation of a general function $f(x, y)$ is given as

$$\sigma_f = \sqrt{\left(\frac{\partial f}{\partial x}\right)^2 \sigma_x^2 + \left(\frac{\partial f}{\partial y}\right)^2 \sigma_y^2} \tag{11}$$

Accordingly, error propagation in each case can be assessed by comparing the coefficient of variations, σ_{Rp}/R_p and σ_S/S:

$$\left(\frac{\sigma_{Rp}}{R_p}\right)^2 = \frac{\sigma_x^2}{x^2} + \frac{\sigma_y^2}{y^2} \tag{12}$$

$$\left(\frac{\sigma_s}{s}\right)^2 = \frac{\dfrac{\sigma_x^2}{x^4} + \dfrac{\sigma_y^2}{y^4}}{\left(\dfrac{1}{x} + \dfrac{1}{y}\right)^2} \tag{13}$$

As both x and y are nonnegative, it can be shown that the coefficient of variation for S in Eq. (13) is never greater than that for R_p in Eq. (12), i.e., error propagation is more rampant in R_p (multiplicative function) than in S (additive function). This result can be generalized to any number of terms as well.

These comparisons show how S is superior to general classes of quality criteria functions (R_s, R_p, R_{min}), albeit having the same classical resolution function $R_{i,j}$ as its basis. The preservation of individual peak pair contributions, elimination of arbitrary cut-off values, and lower error propagation rate clearly make S an attractive choice for a quality criteria function.

At first glance, the switch from Eq. (1) to (7) seems to introduce a problem when $t_i = t_j$, as now $R_{i,j}$' would go to infinity. This is true. In fact, if there are n compounds in the sample, there could be $n(n-1)/2$ surface loci where S becomes infinity, effectively creating impenetrable barriers in the x-y-z domain. However, this should not hinder visualization of S, as explained below.

Fig. 1 shows a progression of three chromatographic peaks from overlapping to well-separated. The middle state is a hypothetical situation ("limiting overlap") in which all of the peaks

are barely separated, one appearing right next to another. In this case $S = n - 1$ exactly, assuming peak symmetry. If the system evolves from limiting overlap to a better separation, then $S \leq n - 1$. By the same token, if $S > n - 1$, then the separation must be worse than the limiting overlap (unacceptable). Therefore, $S > n - 1$ can be used as a rejection criterion when visualizing S. In other words, $n - 1$ is effectively set as the upper limit of S, thereby ignoring singularities when $t_i = t_j$ in Eq. (7). Note however, that $S < n - 1$ does not necessarily mean that the separation is better than limiting overlap. Also, $S \leq n - 1$ might not be feasible at all if there are too many compounds present in the sample (overcrowding of peaks in the chromatogram), in which case a less stringent rejection criterion may be chosen.

Revisiting the limiting overlap (Fig. 1), it is clear that the inequality $S < n - 1$ is a result of inherently simple peak series geometry. A direct consequence of this nice feature is that given the number of compounds n, the absolute significance of S values can be readily assessed. That is, if $S > n - 1$, one knows that there is peak overlap.

Fig. 2 shows a surface plot of S for a hypothetical sample containing glucose, xylose, pyruvic acid, malic acid, formic acid, fumaric acid, and glycerol ($n = 7$) such that all peak widths are 1 min at fixed $F = 0.3$ ml/min. For ease of visualization, the direction of the S axis is inverted. A global optimum ($S = 5.90$, $T = 25$ °C, $C = 3.33$ mM) and eleven local optima are shown. Also evident in the figure is a rejection criterion $S < 16$, which is a less stringent criterion than $S < n - 1 = 6$ based on the limiting overlap. For this set of compounds, $S < 6$ is only true in a small neighborhood around the global optimum. Therefore, based on absolute interpretation, there is peak overlap elsewhere throughout the domain.

3.2. Development and characterization of a novel optimal search algorithm

The challenge for any optimal search method is to identify a global optimum. Success highly depends on the nature of the function evaluated, and for non-analytical functions, absolute confidence in identifying the true global optimum is generally not possible. If a function can be visualized by contour or surface plots, the global optimum can be identified by inspection (precision is a separate issue). However, a numerical approach is necessary for optimization problems in more than two dimensions.

Here we have developed an iterative stochastic search (ISS) method for the search of the global optimum. To our knowledge, the method has never appeared in the literature on HPLC optimization, and global optimization in general. The proposed algorithm is outlined as follows:

1. Generate a random point in the x-y-z domain. This is initialization for 'best point'.
2. Generate m more random points in the domain. Each time, update the best point if the new point is better (has lower S value). m should be a small number, just big enough to generate meaningful statistics.
3. Sort the m points from best to worst (lowest to highest S) to form a list. This is initialization for 'storage points'.
4. Generate N uniformly distributed random points in the domain, updating the best point as before (N should be several orders of magnitude greater than m). Each time, compare the new point to the worst point in the list (with highest S). If the new point is better, update the worst point in the list, and sort the list again (equivalent to insertion of the new point). If this is the first iteration, instead of N use N_{first} (one or two orders of magnitude greater than N).
5. If the best and worst points in the list are equally good (S values within a predetermined tolerance criterion ε), stop the search. The best point in the list is identified as the global optimum. If not, continue.

6. Calculate the mean and standard deviation for the x, y, z coordinates of the points in the list.
7. Generate a new (smaller) domain as the mean ± three standard deviations for the x, y, z coordinates. The new domain must satisfy two requirements: it must be a subset of the old domain, and it must contain the best point. Otherwise, adjust the ranges accordingly.
8. Go back to step 4.

Each iteration in the ISS algorithm essentially identifies m best points out of N points. This can be achieved simply by sorting the N points directly, but such implementation would be computationally demanding and require large storage memory. The 'on-demand' sorting algorithm operating on a small list (m elements) minimizes CPU and memory load while achieving the same result.

The first iteration is the most critical. In this step, more points (N_{first}) are generated to ensure that the whole domain is sampled more thoroughly. At the end of the first iteration, the m best points should already cluster around the neighborhood of the global optimum. Statistical measures of the m best points (center of mass, standard deviation) are then used to define a new, smaller domain for the second iteration (the choice of a $\pm 3\sigma$ span is conservative in a sense that if m sample points come from a normally distributed population, the entire population is represented within $\mu \pm 3\sigma$). As such, subsequent iterations are done over smaller (and shrinking) domains surrounding the global optimum, until finally all of the m best points are within a small tolerance ε, at which point the global optimum is identified.

The shrinking domain is analogous to serial dilution of a concentrated liquid sample. By serial dilution, the same degree of dilution can be achieved using less amount of diluent. In this case, the same degree of precision can be achieved by generating fewer points total. Therefore, N should not be too large as to cause oversampling (because only a fraction of the generated points are accepted), but also not too small as to cause unrepresentative sampling.

If only tracking of the best point is used in ISS, the algorithm would be similar to grid search (GS). However, homogeneous sampling of the x-y-z domain is achieved here through the generation of N random points instead of grid construction. This requires N to be large enough, and the points must be uniformly distributed.

To compare GS and ISS, consider the point density ρ (defined as N/domain volume) for the last iteration (n_{iter}) where convergence is obtained. For GS to have the same precision as ISS, it must have the same point density, but applied to the whole original domain volume V_0. Therefore, the ratio of points generated (and evaluated) in GS to ISS is calculated as

$$r = \frac{\rho V_0}{(n_{iter}-1)N + N_{first}} = \frac{N\left(V_0 / V_{iter}\right)}{(n_{iter}-1)N + N_{first}} = \frac{\left(V_0 / V_{iter}\right)}{(n_{iter}-1) + \left(N_{first} / N\right)} \tag{14}$$

Although it is not possible to obtain a general value for n_{iter}, our experience with the current system shows that it is normally below 100, even for the most difficult case (all compounds included in optimization). As N_{first} is also about two orders of magnitude higher than N, the denominator of Eq. (14) should be in the order of 100 or less. However, the numerator V_0/V_{iter} is very large because the upper and lower bounds of each dimension (x, y, or z) becomes asymptotically close at the end of iteration, and often within machine precision (10^{-8}). This would make the ratio r (and thus computation time) prohibitively large, proving that GS can never achieve the same degree of precision as ISS. In fact, the GS algorithm itself cannot provide any estimates of precision/confidence on the global optimum, as it only uses one storage point. In ISS, the use of m

storage points allows for identification of a small convergence neighborhood around the global optimum such that precision is defined by ε, and confidence intervals by the smallest and largest storage point coordinates.

From a convergence (precision and confidence) standpoint, the simplex search (SS) is analogous to ISS in that the $k + 1$ vertices also serve as storage points. SS is a sequential algorithm (path-dependent) that climbs downhill in the quality criteria function field. Although SS is a fast algorithm, by design it converges to the nearest local optimum, instead of to the global optimum. This problem is overcome in ISS by thorough sampling (N_{first} points) of the entire domain in the first iteration.

The simulated annealing (SA) method was used in a recent example of HPLC optimization [7]. SA is a widely used global optimization technique that mimics the metallurgical process of annealing (slow cooling). The algorithm consists of a random walk within the simulation domain, with each trial move accepted with probability of 1 if it is downhill (criteria function improves), but follows the Maxwell-Boltzmann distribution otherwise [8]. A nonzero probability of accepting uphill moves allows the optimization path to climb out of local optima. However, as the Boltzmann factor vanishes with gradual lowering of system 'temperature', uphill moves become less likely and eventually the path only goes downhill near the global optimum.

Although ISS bears a resemblance to SA in that both rely on a stochastic factor in the progression toward the global optimum, the two algorithms are fundamentally different. The optimization path in SA is a Markov chain, in which the next position in the path is dependent on the current position [9]. Thus when the path encounters a local optimum, it cannot escape immediately but rather oscillates until the ridge is reached, resulting in futile cycles. At early stages of the simulation, such wasteful oscillations may even occur around the (then indistinguishable) global optimum. In ISS, the next position in the optimization sequence is independent of the current position (random search, not random walk). Progression toward the global optimum is therefore not subject to spatial restrictions governing a path / chain, but allowed to explore the entire domain freely and uniformly. Within a Markov chain of length N, a fraction will be wasted in SA due to futile cycles, but all N points will contribute to the uniform sampling of the simulation domain in ISS, resulting in identification of m best points for the next iteration.

For a successful implementation of SA, many parameters such as length of Markov chain, initial step size and temperature, as well as threshold criteria and coefficients for temperature and step size decrement (cooling schedule) [9, 10] need to be fine-tuned to best suit the behavior of the quality criteria function and volume of the simulation domain. In contrast, ISS implementation only involves N_{first}, N, and m. Furthermore, as m is known to be a small as to facilitate fast sorting, fine tuning is only needed for N_{first} and N. From a practical standpoint, ISS is clearly an easier algorithm.

3.3. Implementation of the proposed optimization method

A computer program (OPTIMIZE) was written in Visual Basic 6 (Microsoft, Redmond, WA) for automated optimum identification, based on the alternative global resolution function S, search algorithm ISS, and model coefficients for retention times as described previously. Execution of the overall optimization strategy (experimental design, modeling, scoring, and optimum identification) is demonstrated on a sample containing representative substrates and products found in microbial fermentation processes. The sample contained 0.1 g/l each of potassium phosphate (KH_2PO_4), glucose, xylose, arabinose, malic acid, succinic acid, lactic acid, formic acid, acetic acid, and ethanol (10 compounds). Using OPTIMIZE, optimal operating conditions were T

= 28.6 °C, V = 0.3 ml/min, and C = 9.807 mM, with analysis time = 42 min based on ethanol as the last eluting compound. The optimized run is shown in Fig. 3a. The elution times are in excellent agreement with the predicted values according to the retention model (all within 0.6%, except for acetic acid at 2.4%). The same is true for the quality criteria function S, which is 5.94 versus the predicted value of 5.96 (0.4% deviation), assuming all peak widths are 1 min.

The retention model allows us not only to predict the optimal condition, but also to avoid pathological conditions. For this set of compound, there are two coelution loci at V = 0.3 ml/min, i.e., phosphate-glucose and xylose-malic acid. These two loci/lines cross at T = 56.5 °C and C = 15.537 mM, at which phosphate would coelute with glucose and xylose would coelute with malic acid. The sample was run at this condition, and the coelutions occur as predicted (Fig. 3b). Comparison of Fig. 3a and 3b demonstrates that even at the same flow rate, the choice of temperature and solvent concentration can produce strikingly different results. The optimized run still has minor overlaps (solvable through deconvolution using chromatogram analysis packages), but the pathological run has two complete overlaps, which means that not only two, but four (40%) compounds are unquantifiable. All the same, this shows how the retention model used was able to accurately predict both the best and worst operating conditions for a particular sample.

3.4. Application of iterative stochastic search method to higher dimensional problems

From the algorithm description, it is evident that ISS can be easily generalized to more than three dimensions. The method can be tested using a periodic, hyperdimensional function with many optima:

$$F_1(\mathbf{x}) = \prod_{i=1}^{d} \frac{\cos x_i}{e^{0.01x_i^2}} \tag{16}$$

and also the non-periodic version:

$$F_2(\mathbf{x}) = \prod_{i=1}^{d} \frac{1}{e^{0.01x_i^2}} \tag{17}$$

where $\mathbf{x}$ is the vector of independent variables and d is the number of dimensions/independent variables. Both F_1 and F_2 assume a global optimum value of 1 at $\mathbf{x}$ = [0].

Correct identification of the global optimum is achieved in all trial runs ($\varepsilon = 10^{-5}$, r = 10). Reasonable simulation time (under 1 min) is achieved up to d = 7 for F_1. Optimization of F_2 is much faster because of the simpler form of the function. At d = 7, F_2 is optimized within 0.2 s.

Although hypothetical functions F_1 and F_2 are different in form compared to real quality criteria functions (e.g., S), they are representative of "difficult" and "easy" hyperdimensional functions. F_1 is certainly as difficult as any real quality criteria function, so robust performance of ISS up to seven dimensions here looks promising, suggesting potential application in HPLC optimization in larger dimensional spaces (i.e., temperature, flow rate, pH, ionic strength, tertiary mobile phase composition).

4. Conclusions

The alternative global resolution function S for HPLC optimization proposed in this work shows superior performance when compared to general classes of quality criteria functions (R_s, R_p, R_{min}), including lower error propagation rate, preservation of individual peak pair contributions, elimination of arbitrary cut-off values, and a unique capability to interpret absolute significance of function values through a simple integer inequality. The novel global optimization algorithm (iterative stochastic search, ISS) also developed in this work shows clear advantages

over existing algorithms for HPLC optimization (grid search, simplex search, simulated annealing) in its ability to correctly identify the global optimum (instead of local optimum), with higher precision, with more efficient use of computation cycles, and with easier implementation. Based on a case study using a hyperdimensional function with many optima, robust performance of ISS also suggests its possible application in simultaneous, higher-dimensional HPLC optimizations. Successful application of S and ISS to HPLC optimization was demonstrated in the separation of ten representative substrates and products found in microbial fermentation. Excellent agreement was found between actual and predicted values for the optimized (best) and pathological (worst) conditions. The overall optimization strategy successfully implemented in this work can be generalized to any HPLC optimization problem.

Acknowledgments

This project was funded by the NSF / DOE / USDA. The authors wish to thank Mr. Ganesh Sriram of the ISU Department of Chemical Engineering for help in running the simulated annealing routine and suggestions in constructing periodic functions.

References

[1] P.J. Schoenmakers, A.C.J.H. Drouen, H.A.H. Billiet, L. Degalan, Chromatographia 15 (1982) 688.
[2] S.N. Deming, M.L.H. Turoff , Anal. Chem. 50 (1978) 546.
[3] J.L. Glajch, J.J. Kirkland, K.M. Squire, J.M. Minor, J. Chromatogr. 199 (1980) 57.
[4] J.C. Berridge, J. Chromatogr. 244 (1982) 1.
[5] Y. Guillaume, E.J. Cavalli, E. Peyrin, C. Guinchard, J. Liq. Chromatogr. Relat. Technol. 20 (1997) 1741.
[6] V. Harang, A. Karlsson, M. Josefson, Chromatographia 54 (2001) 703.
[7] Y.C. Guillaume, E. Peyrin, Talanta 51(2000) 579.
[8] W.H. Press, B.P. Flannery, S.A. Teukolsky, W.T. Vetterling. Numerical Recipes in Fortran, second ed., Cambridge University Press, New York, 1992.
[9] P.J.M. van Laarhoven, E.H.L. Aarts, Simulated Annealing: Theory and Applications, D. Reidel Publishing Company, Dordrecht, Netherlands, 1987.
[10] B. Hajek, Math. Oper. Res. 13 (1988) 311.

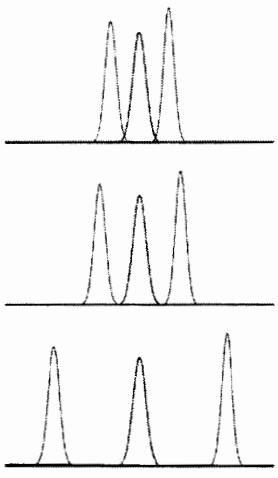

$S > n - 1$

$S = n - 1$

$S < n - 1$

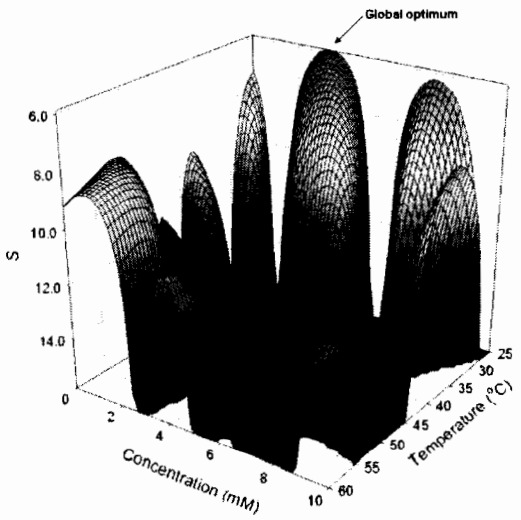

Fig. 1. Progression of peaks from overlapping to well-separated, with a limiting overlap as a hypothetical state. At this state the peaks are barely separated, and individual peak pairs contribute to $S = n - 1$. As separation is better when $S \leq n - 1$, $S > 1$ is rejected because it is worse than limiting overlap.

Fig. 2. The quality criteria function S at a fixed $F = 0.3$ ml/min for a hypothetical sample containing glucose, xylose, pyruvic acid, malic acid, formic acid, fumaric acid, and glycerol ($n = 7$) such that all the peaks are 1 min in width. The direction of the S axis is reversed for ease visualization. A rejection criterion $S < 16$ is shown, which is less stringent than limiting overlap ($S < n - 1 = 6$). Topology of S exhibits disconnected regions with many local optima.

(a)

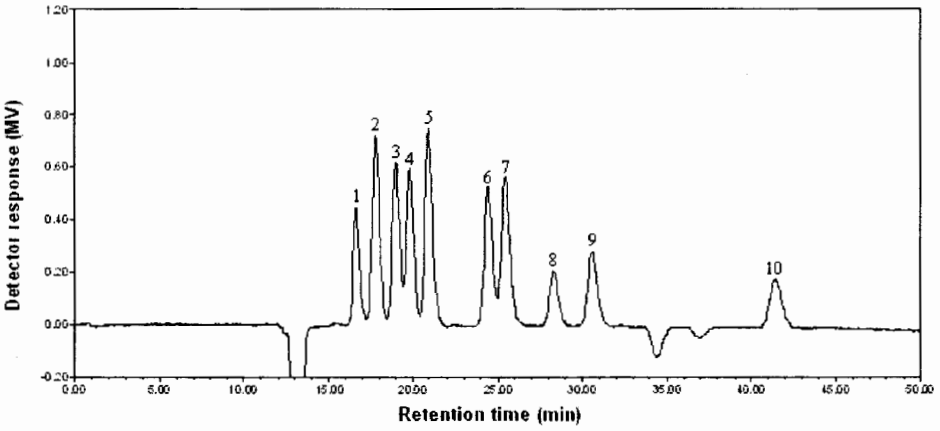

(b)

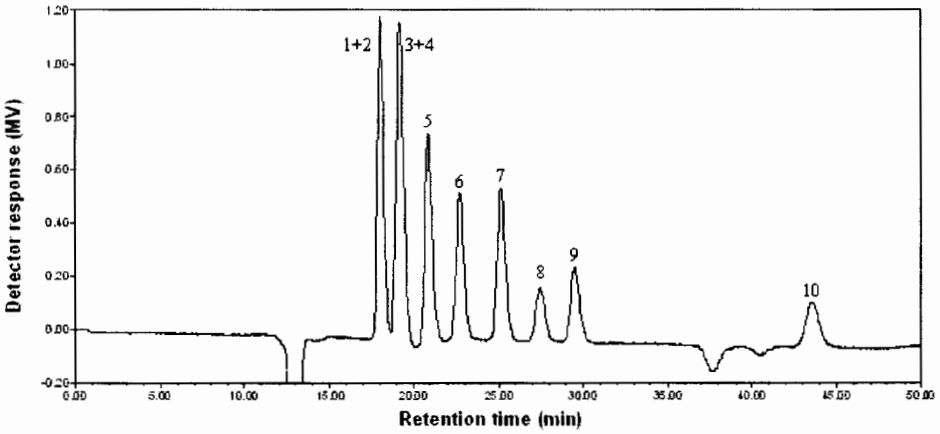

Fig. 3. HPLC separation of a sample containing 0.1 g/L each of (1) potassium phosphate (KH_2PO_4), (2) glucose, (3) xylose, (4) malic acid, (5) arabinose, (6) succinic acid, (7) lactic acid, (8) formic acid, (9) acetic acid, and (10) ethanol, in the order of elution times ($F = 0.3$ ml/min). (a). Optimized / best condition at $T = 28.6$ °C and $C = 9.807$ mM. (b) Pathological/worst condition at $T = 56.5$ °C and $C = 15.537$ mM. Here phosphate coelutes with glucose and xylose coelutes with malic acid.

Synchrotron Fourier Transform Infrared Microspectroscopy as a Tool to Monitor the Fate of Organic Contaminants in Plants

Kenneth M. Dokken[1], Lawrence C. Davis[1], Larry E. Erickson[2], Nebojsa Marinkovic[3], Departments of Biochemistry[1] and Chemical Engineering[2], Kansas State University, Manhattan, KS 66506; Albert Einstein Center for Synchrotron Biosciences[3], Beamline U2B, National Synchrotron Light Source, Brookhaven National Laboratory, Upton, NY 11973

Abstract

The use of phytoremediation as a tool for cleaning sites contaminated with aromatic and heterocyclic organic compounds has gained much recognition over the past decade. It is obvious that plants are a more cost-effective, environmentally friendly, and aesthetically pleasing alternative to older, conventional methods. It is well documented that many plants can biotransform organic contaminants. However, the ultimate fate and transport of these organic compounds are unknown within most plant systems. Major issues in the field are whether transformed contaminants are still bioavailable and whether they may have greater toxicity than the parent compound. We are studying the potential of Fourier transform infrared (FTIR) microspectroscopy to determine the fate of aromatic and heterocylic organic compounds within the roots of plants. Currently, we are studying how benzotriazole and its derivatives are taken up and metabolized by sunflowers and maize. Previously we found changes in the root structure in sunflowers treated with benzotriazole due to uptake, incorporation, and/or transformation of benzotriazole. These changes were predominantly found in the lignin portion of the root, specifically in the xylem region. We were able to map out the location of benzotriazole sequestration using synchrotron FTIR microspectroscopy at Brookhaven National Laboratory. Our working hypothesis is that the peroxidatic system responsible for lignification ultimately incorporates benzotriazole into a polymeric material that is no longer bioavailable. Studies using isotopically labeled benzotriazole have shown that a large fraction is unextractable after several days of exposure, with a significant amount remaining in the root. The technique of FTIR microspectroscopy has the potential be used as a tool in phytoremediation to study changes of plant structure induced by the presence of organic contaminants in soil and water. This in turn may help in determining what plants can be used to remediate certain organic compounds when developing phytoremediation schemes.

Introduction

When determining which plant or plants are needed for a certain phytoremediation scheme, there are two important issues to consider. The first issue to consider is the fate and transport of the organic contaminant within the plant. The second deals with understanding how the uptake of organic contaminants affects the plant structure and development. One such technique that can provide this information is Fourier transform infrared (FTIR) microspectroscopy. FTIR spectroscopy provides highly specific chemical characterization revealing type, distribution, and the relative quantity of chemical components in a system. It has been used successfully for decades to analyze agricultural products **[1]** and in cellulose **[2]** and lignin **[3]** chemistry.

The combination of a microscope accessory with FTIR spectroscopy allows for chemical imaging of biological samples at the level of several tens of microns with good spectral quality **[4]**. FTIR microspectroscopy has been significantly employed for the study of the anatomical development of plants **[5–7]**, plant cell walls **[8–10]**, and distinguishing cell wall mutants from wild types **[11,12]**. This provided the potential for our laboratory to use this technique to study how uptake of organic contaminants affects plant structure and development as well as deter-

mining how the plant dealt with the organic contaminants. However, access to a benchtop FTIR microspectrometer was limited and did not provide sufficient spatial resolution needed to conduct such a study.

The National Synchrotron Light Source (NSLS) at Brookhaven National Laboratory in Upton, NY provides a synchrotron source coupled to a FTIR microspectrometer allowing the proper spatial resolution at the diffraction limit. The synchrotron source is 100–1000 times brighter than a benchtop source **[4]** allowing chemical imaging at a cellular level **[13]**.

This paper will focus on determining the effect and fate and transport of benzotriazole (BT), a corrosion inhibitor used in antifreeze and airplane deicing fluids, in sunflower plants using synchrotron FTIR microspectroscopy. Experiments with sunflowers grown in ^{14}C radiolabeled BT have shown that a large fraction is unextractable after several days of exposure, with a significant amount remaining in the root **[14]**. Thus, this study will be particularly concentrated on the roots of the BT-treated sunflower plants. Also, previous studies showed changes in the root structure in sunflowers treated with BT due to uptake, incorporation, and/or transformation of BT **[15]**. Chemical group maps of the sections of root tissue from BT-treated sunflower plants reveal changes in the lignin structure and sequestration of the BT in the xylem region.

Experimental

Sunflower seeds were germinated in vermiculite moistened with sterilized tap water for five days and then transplanted to 600-mL amber stock jars containing full strength Hoagland's solution for a period of two days. Hoagland's solution was prepared as previously reported by Castro *et al.* **[16]**. The sunflower plants were then grown hydroponically in full-strength Hoagland's solution containing 0, 10, 20, and 30 mg/L 1H-BT for two weeks. After a two-week growth period, the sunflower plants were removed from their respective hydroponic solutions and washed with deionized water prior to dissection and cryomicrotome sectioning. Samples of root tissue were taken in 1-cm sections from the tip. The root tissues were frozen onto specimen blocks surrounded by Tissue Tek (Sakura Finetek USA, Inc.) at –40°C, in preparation for sectioning at –20°C. The 4-μm-thick frozen sections were thaw-mounted onto infrared reflecting "E" glass microscope slides (SensIR® Technologies). The slides were then stored at room temperature until analysis.

FTIR microspectroscopy was conducted at the NSLS using a Nicolet NicPlan IR microscope on beamline U2B. The narrow-range, internal mercury cadmium telluride (MCT/A) detector was used, covering a range of 7000–650 cm^{-1}. The spectra were recorded in absorption mode at a resolution of 4 cm^{-1} with 128 scans co-added to reduce signal to noise ratio. Each spectrum is ratioed to a reference which was recorded with the same parameters and conditions. A 30-μm aperture size was used for scouting potential specimens for mapping and taking individual spectra. A 12-μm aperature with 10-μm steps was used for generating an IR map using the Atlμs software (Thermo Nicolet). Spectra were baseline corrected and normalized using Omnic 5.1a software (Thermo Nicolet).

Results and Discussion

The sunflower plants grown in BT solutions display obvious growth and developmental differences, especially at the highest treatment concentration (Figure 1). The plants at the 30 mg/L BT treatment display stunted growth and crinkling and darkening of the leaves. Also, they have one less set of true leaves. This suggests that BT depresses plant development at higher concentrations. As the BT concentration is increased, the amount of root growth decreases. At the highest concentration, it can be seen that the root system exhibits less growth with a high

production of small, thick adventitious roots. However, the sunflower plants can withstand up to 60 mg/L BT and still maintain growth and solution uptake **[15]**.

After physical examination, the roots of the plants were sectioned and prepared for FTIR microspectroscopy at the NSLS. There was particular focus on the roots because previous work showed that a significant fraction of the BT taken up by the plant was unextractable and present in the roots **[14]**. Also, previous macro-FTIR analysis of BT-treated root ground in KBR pellets exhibited infrared peaks commonly found in BT **[15]**.

Initially, we conducted scouting experiments on the root sections of the untreated and BT-treated plants using a 30-μm aperture on the IR microscope. Our intention was to determine the botanical part in which the BT may be transformed/metabolized and/or stored within the roots. We found the presence of peaks common to BT as well as the most significant structural changes to be in the xylem tissue of the root. Figure 2 shows the spectra for the xylem tissue from sections of the untreated control and 30 mg/L BT-treated sunflower plants. The most significant BT peak appears at 745 cm^{-1} in the xylem tissue of the BT-treated plant. This is the most intense peak in BT due to aromatic C-H out-of-plane bending, commonly found in unsubstituted heterocyclic aromatic compounds **[18]**. The other significant differences that can be seen in the spectrum of xylem tissue from BT-treated roots are related to lignin. The huge increase of the peak at 1250 cm^{-1}, which represents carbonyl stretching, may be due to an increase in the guaiacyl-syringyl subunits **[3,19]**. This is confirmed by the appearance of a shoulder at 1735 cm^{-1}, which also represents carbonyl stretching due to unconjugated ketone and carboxyl groups commonly found in lignin **[19]**. Also, the appearance of a peak at 1635 cm^{-1}, due to aromatic stretch in lignin, in the BT-treated root xylem suggests an increase in lignin production or a different type of substitution of the subunits in lignin. The xylem of plant roots is the conduit in which nutrients are transported from the roots into the upper tissues of the plant. It is also the site of abundant lignin production. Lignin is a highly-substituted polymer composed of monolignols produced by the phenylpropanoid pathway, which is produced as reinforcement for vascular tissues in herbaceous plants and grasses **[17]**. The biosynthesis of lignin takes place by coupling of monolignol subunits through a free radical, nonenzymatic process **[19]**. With this in mind, it is very significant that the most prominent changes in the roots of BT-treated plants are found in the xylem tissue, and it is the area where the intense BT peak is found. This may confirm a previous speculation that BT is sequestered in the xylem and then incorporated into lignin via the phenylpropanoid pathway, rendering BT no longer bioavailable **[15]**.

To further support that the xylem tissue is the location in which BT is sequestered and transformed, extensive IR mapping was conducted. False color intensity maps of the root sections from untreated and BT-treated plants were created using a 12-μm aperture and 10-μm steps. Figure 3 shows the area of the root sections that were mapped. The area covered the epidermis, cortex, and xylem tissue of the root sections. The false color intensity maps are generated to show the highly intense bands as blue or green, the less intense bands as red, pink, and very little or no intensity represented as white. Figure 4 shows the maps of untreated and BT-treated root sections at 745 cm^{-1}, representing the highly intense aromatic BT peak. These peaks were not observed in the untreated control root tissue. However, this peak can be observed throughout the root tissue from the BT-treated plants, with the highest intensity (green color) seen in the xylem region. In Figure 5, the IR maps for the carbonyl stretch for lignin subunits can be observed for each plant treatment. Both IR maps have highly intense carbonyl stretches for lignin in the xylem region, but the BT treated root tissue shows this peak to be more intense throughout all the regions of the root as compared to the control. This could signify that the plant is adjusting to the

presence of BT by producing more lignin. Figure 6 provides more evidence that the plant produces more lignin in the presence of BT. The high intensity for the 1735 cm^{-1} carbonyl stretch in the xylem region of the BT-treated root tissue shows lignin deposition not observed in the untreated control tissue. Both have some peak intensity in the outer region of the root tissue because of lignin found in the epidermis. Both control and treated plants have the carbonyl stretch at 1259 cm^{-1} in the xylem, but only treated contains the 1735 cm^{-1} carbonyl stretch. This suggests that incorporation of BT into lignin may have led to a different type of substitution of monolignol subunits and BT.

Conclusion

Using synchrotron FTIR microspectroscopy, we were able to show that BT is sequestered in the xylem region of sunflower plant roots and possibly incorporated into the plant structure by lignification. Spot analysis and false color intensity maps displayed high intensities for the major lignin and BT peaks in the xylem root tissue of sunflowers treated with BT. Currently, we are studying the effects of BT on maize and grasses. Future work will include studying the effects of 2,4,6-trinitrotoluene and its major breakdown products on these plants. We are going to employ principal component analysis of the spectral data in order to develop a rapid method for determining what type of organic contaminants have been taken up by the plant. Thus, FTIR microspectroscopy may be used as a tool in phytoremediation to study changes of plant structure induced by the presence of organic contaminants in soil and water.

Acknowledgments

Funding for experimentation at the NSLS at Brookhaven National Laboratory was provided the Department of Energy. Further support was provided by the U.S. Environmental Protection Agency under assistance agreement R-825550 through the Great Plains/Rocky Mountain Hazardous Substance Research Center and the Kansas Agricultural Experiment Station. The authors would also like to thank the staff at the NSLS at Brookhaven National Laboratory and the Kansas State University Veterinary Diagnostic Laboratory, supervised by Cindy Chard-Bergstrom, for the use of their cryomicrotome.

References

1. Messerschmidt, R.G. and M.A. Harthcock, Eds., *Infrared Microspectroscopy: Theory and Applications*, 1988, Marcel Dekker, New York.
2. Liang, C.Y., Ed.: R.T. O'Connor, Infrared spectroscopy and physical properties of cellulose, in *Instrumental Analysis of Cotton Cellulose and Modified Cotton Cellulose*, 1972, Marcel Dekker, New York, pp. 59–91.
3. Faix, O., Fourier Transform Infrared Spectroscopy, in *Methods in Lignin Chemistry*, 1992, Springer-Verlag, Berlin, pp. 83–109.
4. Marinkovic, N.S., R. Huang, P. Bromberg, M. Sullivan, J. Toomey, L.M. Miller, E. Sperber, S. Moshe, K.W. Jones, E. Chouparova, S. Lappi, S. Franzen, M.R. Chance, Center for Synchrotron Biosciences' U2B beamline: An international resource for biological infrared spectroscopy, J. Synchrotron Radiat. (2002) 9, 189–197.
5. Zeier, J., L. Schreiber, Chemical composition of hypodermal and endodermal cell wall and xylem vessels isolated from *Clivia miniata*, Plant Physiol. (1997) 113, 1223–1231.
6. Zeier, J., L. Schreiber, Fourier transform infrared-spectroscopic characterization of isolated endodermal cell walls from plant roots: Chemical nature in relation to anatomical development, Planta (1999) 209, 537–542.

7. McCann, M.C., K. Roberts, Changes in cell wall architecture during cell elongation, J. Exp. Bot. (1994) 45, 1683–1691.
8. Zeier, J., L. Schreiber, Comparative investigation of primary and tertiary endodermal cell walls isolated from the roots of five monocotyledoneous species: Chemical composition in relation to fine structure, Planta (1998) 206, 349–361.
9. McCann, M.C., M. Hammouri, R.H. Wilson, P. Belton, K. Roberts, Fourier transform infrared microspectroscopy is a new way to look at plant cell walls, Plant Physiol. (1992) 100, 1940–1947.
10. McCann, M.C., M. Bush, D. Milioni, P. Sado, N.J. Stacey, G. Catchpole, M. Deferenez, N.C. Carpita, H. Hofte, P. Ulvskov, R.H. Wilson, K. Roberts, Approaches to understanding the functional architecture of the plant cell wall, Phytochem. (2001) 57, 811–821.
11. Chen, L., N.C. Carpita, W.-D. Reiter, R.H. Wilson, C. Jeffries, M.C. McCann, A rapid method to screen for cell-wall mutants using discriminant analysis of Fourier transform infrared spectra, Plant J. (1998) 16, 385–392.
12. Ha, M-A., I.M. MacKinnon, A. Sturcova, D.C. Apperley, M.C. McCann, S.R. Turner, M.C. Jarvis, Structure of cellulose-deficient secondary cell walls from the *irx3* mutant of *Arabidopsis thaliana*, Phytochemi. (2002) 61, 7–14.
13. Jamin, N., P. Dumas, J, Moncutt, W.-F. Fridman, J.-L. Teillaud, G.L. Carr, G.P. Williams, Highly resolved chemical imaging of living cells by using synchrotron infrared microspectrometry, Proc. Nat. Acad. Sci. USA, (1998) 95, 4837–4840.
14. Castro Diaz, S., Experimental study on phytotransformation of benzotriazole in hydroponic culture of sunflowers, Ph.D. Dissertation, Kansas State University, July 24, 2003.
15. Dokken, K.M., L.C. Davis, L.E. Erickson, S. Castro (2002) Fourier transform infrared spectroscopy as a tool to monitor changes in plant structure in response to soil contaminants. Proceedings of the 2002 Conference on Application of Waste Remediation Technologies to Agricultural Contamination of Water Resources, Kansas City, MO, 2002, pp. 250-256, http://www.engg.ksu.edu/HSRC.
16. Castro, S., L.C. Davis, L.E. Erickson, Plant-enhanced remediation of glycol-based aircraft deicing fluids, Pract. Period. Hazard. Tox. Radioact. Waste Management, (2001) 5, 141–152.
17. Waisal, Y., A. Eshel, U. Kafkafi, Eds., *Plant Roots: The Hidden Half*, 1996, Marcel Dekker, New York.
18. Mohan, S., K. Settu, Vibrational spectra and analysis of 1,2,3-benzotriazole. Ind. J. Pure Appl. Phys. (1993) 31, 850–854.
19. Sarkanen, K.V. and C.H. Ludwig, *Lignins: Occurrence, Formation, Structure, and Reactions*, 1971, Wiley, New York.
20. D. Lin-Vien, J. G. Grasselli, N.B. Colthup, W. G. Fateley, *The Handbook of Infrared and Raman Characteristic Frequencies of Organic Molecules*, 1991, Academic, New York.

Figure 1. Sunflowers grown in nutrient solutions containing various BT concentrations for 14 days.

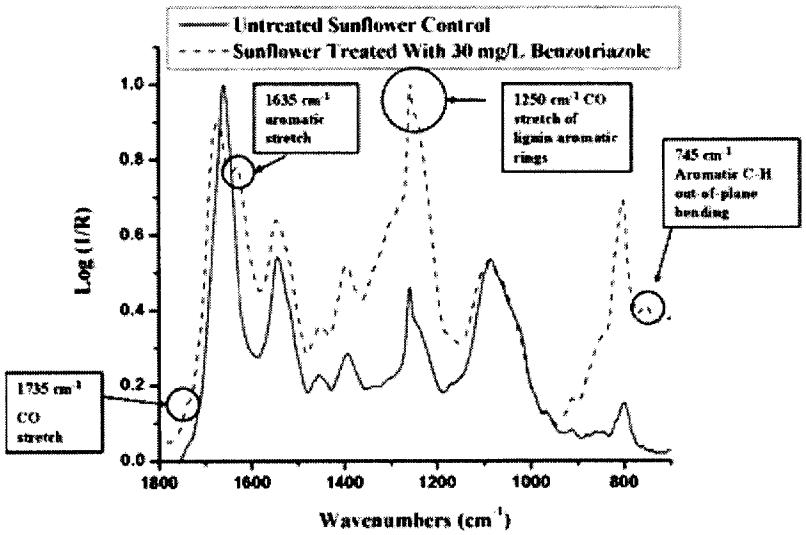

Figure 2. IR spectra of root xylem of untreated and treated sunflower using a 30-μm diameter aperture.

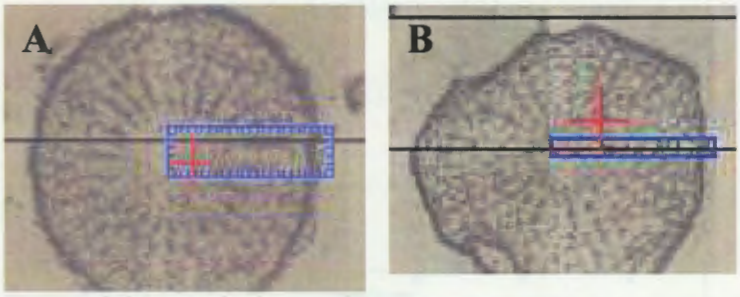

Figure 3. Pictures of the root sections from A. untreated control and B. 20 mg/L BT-treated plants taken at 32X magnification by the NicPlan IR microscope. The rectangular box shows the area mapped.

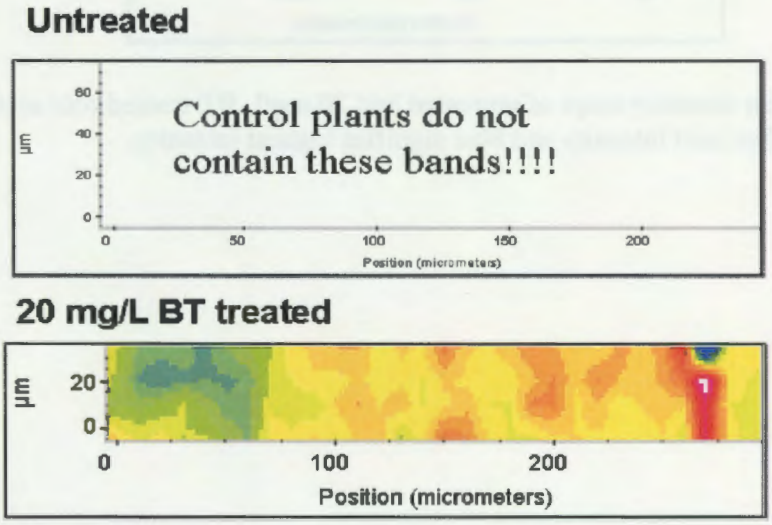

Figure 4. False color intensity maps of untreated and 20 mg/L BT-treated root sections at 745 cm^{-1}. White signifies least intensity and blue signifies highest intensity.

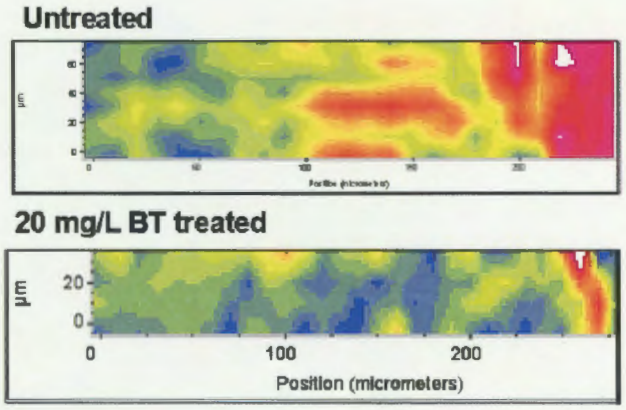

Figure 5. False color intensity maps of untreated and 20 mg/L BT-treated root sections at 1250

cm^{-1}. White signifies least intensity and blue signifies highest intensity.

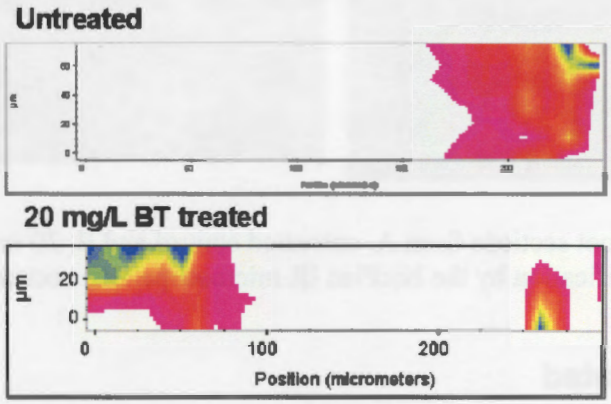

Figure 6. False color intensity maps of untreated and 20 mg/L BT-treated root sections at 1750 cm^{-1}. White signifies least intensity and blue signifies highest intensity.

Ranque-Hilsch Vortex Tube Thermocycler for Fast DNA Amplification and Real-Time Optical Detection

Ryan J. Ebmeier[1], Scott E. Whitney[2], Amitabha Sarkar[2], Michael Nelson[3], Nisha V. Padhye[3], George Gogos[1], and Hendrik J. Viljoen[2]
Departments of [1]Mechanical and [2]Chemical Engineering, University of Nebraska – Lincoln, Lincoln, NE 68588,[3] Megabase Research Products, 4711 Huntington Ave., Suite 2W, Lincoln, NE 68504

Abstract

An innovative polymerase chain reaction (PCR) thermocycler capable of performing real-time detection is described below. This device utilizes the hot and cold gas streams produced from pressurized gas passed through a Ranque-Hilsch vortex tube to efficiently and rapidly cycle three 20-μL samples between the denaturation, annealing, and elongation temperatures. The reaction progress is displayed real-time by measuring the size of a fluorescent signal emitted by SYBR Green/double-stranded DNA complexes. This device can produce significant reaction yields with very small amounts of initial DNA. For example, it can amplify 0.25 fg (~5 copies) of a 96-bp bacteriophage λ-DNA fragment 2.7 x 10^{11}-fold by performing 45 cycles in less than 12 min. The observed PCR amplification yield corresponds to an overall efficiency of 80%. The optical threshold (150% baseline value) was passed 8 min into the reaction at cycle 34. Quantitative PCR is demonstrated by comparison of the number of cycles necessary to reach the optical threshold value for a range of increasing initial DNA concentrations. Potential applications for the Ranque-Hilsch vortex tube thermocycler include point-of-care diagnostic testing, biological warfare agent detection, and virology, microbiology, and oncology research. Also, the compact design and limited dependence on electricity allows this machine to operate as a portable device.

Introduction

The polymerase chain reaction (PCR) is a powerful and sensitive enzymatic technique used to exponentially increase the number of copies of a specific sequence of template DNA. The PCR process includes three steps: sample preparation, DNA amplification, and detection. After preparation, the sample mixture (includeing DNA, primers, and polymerase) is allotted into a desirable sample size (typically 1 to 100 μL) for amplification. The amplification step consists of thermally cycling the sample for N cycles (~35) between specific denaturation, annealing, and elongation temperatures; typically 90-95°C, 50-65°C, and ~72°C, respectively. Theoretically, one cycle will double the existing amount of DNA, but in practice the PCR process can be described in terms of overall efficiency (Y), where $X = (1 + Y)^N$ is the DNA amplification yield. Typical PCR amplification has an efficiency of 70% and requires approximately 35 cycles for 10^8-fold amplification. Gel electrophoresis is the standard for product detection. However, real-time detection can be achieved by measuring the fluorescence of dye/DNA complexes throughout the amplification stage of the reaction. This drastically reduces total assay time by eliminating the need for an individual step for product detection. Real-Time PCR also provides the required optical measurements used in quantitative PCR analysis.

There are many types of PCR machines used in practical applications. However, these devices may generally be classified into two categories: *robotic devices*, which move the DNA samples to the heat; and *thermocyclers*, which bring the heat to the samples. Robotic devices, such as Stratagene's ROBOCYCLER™ (Strategene, La Jolla, CA), move tubes containing PCR

reaction samples to and from a series of water baths, which are heated to different temperatures. Although robotic thermocyclers can be useful in certain applications, they are incapable of high-speed PCR due to their rates of heating and cooling (approximately 2 min/cycle). The two basic types of thermocyclers are programmable heat blocks and forced hot-air thermocyclers. In commonly employed heat block thermocyclers, the amplification stage consists of cycling the temperature of the samples using computer-controlled heat blocks. These devices typically require hours of operation time due to the slow heating and cooling processes. Forced hot air thermocyclers, such as the LightCycler™ (Roche Diagnostics Corporation, Germany) have drastically reduced typical amplification time by eliminating the large thermal mass of heat blocks and using convection heat transfer between air and thin-walled capillary tubes. PCR amplification consisting of 30 cycles can be performed in as little as ~10 to 30 min.

Some of the most recent publications describe PCR results using natural convection processes. For example, Krishnan *et al.* [1] used a Rayleigh-Benard convection cell to amplify 315 ng of DNA in a 35-μL sample with a reaction time of 1.5 h. The amplification and reaction time reported is comparable to standard PCR thermocyclers. Braun *et al.* [2] amplified 500 pg of bacteriophage λ-DNA in a 20-μL sample 10^5-fold within 25 min of assay time. Evidence of a successful reaction was noticed using real-time detection after 8 minutes of amplification.

The heating and cooling performance is the primary concern in all automated thermocyclers. The innovation of the thermocycler described in this paper relies on taking advantage of the natural heating and refrigeration capacities of the Ranque-Hilsch vortex tube. A vortex tube is a device that produces two gas streams of significant temperature difference from a single source of compressed gas. An attractive feature of the vortex tube is its reliability – it operates without any moving parts or electrical components. The inlet gas pressure is typically in the range of 2 to 11 atm and enters a cylindrical container tangentially through one or more ports. After entering the cylinder, the gas spirals down the length of the tube (Figure 1) where it meets a control valve. According to the valve setting, a fraction of the gas (x) will exit the tube at an outlet temperature up to about 110°C warmer than the inlet temperature of the gas. The remaining gas fraction ($1 - x$) exits at the other end with a maximal temperature difference of about 70 °C lower than the initial gas temperature. The outlet temperatures can be varied according to the absolute pressure drops across the tube, the type of gas used, and with the control valve that changes the fraction of gas exiting at each end. Figure 1 illustrates vortex tube operation for one set of flow conditions.

The vortex tube was discovered by George Ranque [3], and a systematic explanation of its performance was achieved by Rudolph Hilsch [4]. However, since that time there has been dispute over the numerous theoretical and experimental approaches used to describe the physical aspects of the vortex tube, now called the Ranque-Hilsch Effect. More recently, these explanations vary from the effects of acoustic streaming in swirling flow researched by Kurosaka [5] to the characterization of the vortex tube as a natural heat pump due to a secondary circulation [6]. Ahlborn *et al.* [7] proposed a mathematical model to predict the outlet temperatures given inlet flow conditions while Frohlingsdorf and Unger [8] have published a numerical investigation of flow within the vortex tube. Ahlborn and Gordon [9] have quantified the performance of the vortex tube as a thermodynamic machine and identified practical application problems in systems with two-phase flow.

The majority of vortex tube applications are associated with the tube's refrigeration capacity. The Ranque-Hilsch vortex tube thermocycler presented in this paper is novel in that it uses computer control and pneumatic flow valves to use both the hot and cold exhaust streams as necessary to heat/cool the PCR samples. This device is based on the simplicity and reliability of the

vortex tube and effectively cycles three 20-μL sample capillaries within the range of PCR typical temperatures.

Experimental

Real-Time DNA Detection Using SYBR Green Dye: The PCR reaction was performed using a 96-bp λ-DNA amplicon of varying initial DNA concentrations in the Ranque-Hilsch vortex tube thermocycler. Reaction progress was monitored real-time by measuring the fluorescence emitted at 520 nm by SYBR Green bound to double-stranded DNA complexes upon excitation at 470 nm. This dye binds to all double-stranded DNA and cannot distinguish between a specific PCR amplicon and primer-dimer artifact. Therefore, careful design of primers, optimal reaction conditions, and a Hot-Start PCR technique is very crucial when using SYBR Green for real-time PCR.

The oligonucleotide primers described by Braun *et al.* [2] were used to amplify the target λ-DNA fragment. The primer sequences were 5'-GATGAGTTCGTGTCCGTACAACTGG -3' and 5'-GGGCAATCAGTTCATCTTTCGTCATGG-3' with melting temperatures of approximately 61°C and 62°C, respectively. The reaction mix (20 μl) consisted of 600 nanomolar of each primer, 100 fg to 0.25 fg of λ-DNA (Fermentas Inc., Hanover, MD), 5 mM magnesium sulfate, 200 μM dNTPs, 1X SYBR Green I (S7563, Molecular Probes), 600 μg/mL BSA, and 0.8 unit of KOD hot start polymerase (Toyobo Co. Ltd., Japan) in 1X KOD hot start polymerase buffer.

The speed of the Ranque-Hilsch vortex tube thermocycler is best used in combination with a fast enzyme, such as KOD hot start polymerase. This enzyme requires an initial 30-s hot start at approximately 90°C to fully activate the polymerase. During this period, thermolabile antibodies bound to the DNA polymerase are inactivated, as described by Mizuguchi *et al.* [10].

Real-Time PCR was achieved by initial activation of the enzyme at 95°C for 30 s, followed by 45 cycles of 95°C for 0 s, 62°C for 0 s, and 72°C for 0 s. There are no holding times required for the denaturation and annealing steps since they happen almost instantaneously. Elongation occurs within a temperature range surrounding 72°C. Therefore, a large portion of the ramp time from the annealing to the denaturation temperature is utilized for elongation. If a fast enzyme such as KOD polymerase is used (approximately 300 nt/s at 72°C), it is possible to copy up to 1,000 bp during the heating stroke, without pausing at 72°C. The amplification consisted of 45 cycles to demonstrate machine sensitivity to 0.25 fg of bacteriophage λ-DNA (~5 copies). Photon counting was carried out once per cycle using a 500-m integration time when the sample reaches 80°C while heating to the denaturation temperature. Samples were also analyzed by 2.5% agarose gel electrophoresis in TAE buffer. The DNA fragments were visualized using 312 nm UV light and photographed with Polaroid Type 667 film.

Ranque-Hilsch Vortex Thermocycler: The basis for the thermal cycling device is the vortex tube (Exair Corporation, Cincinnati, OH). The vortex tube is most commonly used in industry for cooling applications where the exit streams are at atmospheric pressure. The thermal cycling device is novel in that it uses the vortex tube within a system to provide both the heating and refrigeration needed for the necessary thermal cycling of the sample. Since the device is entirely dependent on the performance of the vortex tube, its operational parameters were optimized.

The compressed air supply used is capable of delivering room temperature air at a flow rate of approximately 3.2×10^{-3} m^3/s (6.8 SCFM) at a gage pressure of approximately 5.9 bar (85

psi). The first step in optimizing the vortex tube is to size the generator, a flow restriction device, to correspond with the available air supply. The appropriate generator should maximize the volumetric flow rate, while providing enough resistance to create a large pressure drop across the tube. The tube operates most efficiently at inlet pressures of about 5.5–7.5 bar (~80–110 psi).

The vortex tube is also most effective when the exit streams are near atmospheric pressure. The performance of the vortex tube decreases dramatically with the addition of back-pressure on the cold side. The cold gas temperature will be higher by approximately 2.8°C with 0.345 bar (5 psi) of back-pressure. Accordingly, the hot gas temperature will decrease with increasing back pressure on the cold side. This is important for the thermal cycling device since it is using the vortex tube within a system where back-pressure is present and is dependent on the vortex tube exit temperatures. The amount of back-pressure is minimized by using appropriate fittings and valve orifices.

The gas introduced to the vortex tube inlet produces two exit streams with significant temperature differences. The exit temperatures are variable according to the ratio of gas exiting at each end. Typically, the exit temperature difference at each end is inversely related to the mass fraction of gas exiting. For this application, experimentation concluded that the hot gas temperature must exceed 100°C to ensure the sample can still reach the denaturation temperature after experiencing minimal heat loss throughout the system. To obtain the minimal increase in hot gas temperature of 80°C, the vortex tube must be set so the fraction of hot gas exiting is low, approximately 20% of the inlet flow. The resulting cold flow has a much larger flow rate and exits the vortex tube at about 0°C. Accordingly, the tube becomes more effective during the cooling process and sample heating becomes the rate-limiting step.

The setup of the thermal cycling device is designed around the vortex tube to optimize the convective heat transfer to the sample capillaries during both the heating and cooling processes. The temperatures of the PCR samples are indirectly measured via a thermal sensor placed in an additional capillary tube. This signal is continually recognized within the computer programming, which in turn controls the status of two electronically actuated pneumatic valves. Both of these valves are used to direct the cold air flow within the system according to the sample temperature change required. The hot air flows continuously into the chamber to eliminate excess heat loss through valve hardware. During sample cooling, the hot and cold gas streams are combined in the vortex flow conditioner, a mixing chamber, to produce a net cooling effect on the samples.

The system heats the samples by only allowing the hot air to pass through the sample chamber as shown in Figure 2. The three-way cold flow valve is closed, while the two-way cold release valve is open. This valve configuration forces all of the cold air exiting the vortex tube to be exhausted into the atmosphere while minimizing back pressure. The two-exhaust system allows the vortex tube to operate with less than 0.1 bar (1.5 psi) of back-pressure during sample heating. Meanwhile, the air exiting the hot end of the vortex tube flows through the vortex flow conditioner and across the samples located in the sample chamber. It then exits the system via the sample chamber exhaust. The vortex tube is adjusted so the hot gas temperature is approximately 115°C and the corresponding volumetric flow rate of hot gas produced is about 6.4×10^{-4} m^3/s (1.4 SCFM). The machine can heat the samples at an average rate of about 3.2°C/s.

The transition from heating to cooling must be performed without interrupting the operating vortex tube by stopping flow on the cold side. Therefore, the cold flow valve is opened before closing the cold release valve. The new flow pattern is shown in Figure 3. Adequate cooling is achieved under this configuration where all of the cold and hot gases mix in the vortex flow

conditioner before reaching the sample chamber. Since the mass flow rate of cold gas is about four times greater than the hot gas, it is overwhelming and the resulting stream works to cool the samples to the annealing temperature. The cold gas is approximately 5°C before reaching the two valves and the cold/hot gas mixture is typically around 30°C. The samples are cooled at an average rate of 16°C/s.

Many rapid PCR protocols include temperature holds at the denaturation, annealing, or elongation temperatures. These are achieved via computer-controlled cold gas valve programming for the specified time durations. The machine design allows hot gas to continually flow into the sample chamber, so fine cool air control is used to neutralize its effect on the samples and minimize temperature fluctuations during holds. The fine control is achieved by opening the cold release valve whileswitching the cold flow valve between the open and closed positions. Under these configurations there is always cold gas exiting the system, however, a fraction of the cold gas is occasionally routed into the chamber to provide near isothermal sample conditions. The programming logic uses set temperature limits and temperature vs. time slope measurements to control the status of the cold flow valve. The typical temperature deviation within the chamber during these holds is shown in Figure 4. When there are no holds required at the denaturation or annealing temperatures, overshooting and undershooting is minimized through feedback control from the previous thermal cycle. This enables the machine to make heating/cooling transition adjustments within a PCR amplification to maximize performance by accurately reaching the desired target temperatures. Figure 4 also shows the difference in the rates of temperature change between the heating and cooling process as described earlier.

Thermal control of the sample chamber, measured via a thermal sensor, is achieved using the valve logic and computer programming described earlier. Another major concern is the temperature deviation between the samples. The vortex flow conditioner is the first step in minimizing sample temperature discrepancy by effectively mixing the hot and cold gases to provide nearly isothermal inlet flow conditions. The arrangement of sample capillaries then becomes the primary concern. The staggered arrangement (shown in Figures 2, 3) reduces the effect of the first capillary shadowing the subsequent ones. Also, the sample spacing is minimized to reduce the effect of heat loss to the chamber walls. The thermal sensor is placed in the downstream capillary position to ensure the other three capillaries have reached the desired temperatures. The temperature variance is most important at the denaturation and annealing temperatures. When these are set at 90 and 56°C respectively, the maximum temperature a sample reaches is 91.5°C while the minimum is 55°C. The other capillaries are between these limits and the desired temperature.

The real-time detection is conducted by monitoring the fluorescence in one of the capillaries as the reaction progresses. The reading is taken once per cycle during the heat to denaturation step at a specified read temperature. Ideally, the optical measurements will be taken at a temperature after elongation is completed and primer-dimer artifacts have separated, but before newly formed target DNA denatures. When the capillary reaches the user designated temperature a blue light source (LS450, Ocean Optics, Dunedin, FL) shines light at 470 nm into the capillary where it reacts with the dye/double stranded DNA complexes. When bound to double-stranded DNA, the SYBR Green dye emits light at a wavelength of approximately 520 nm. This optical signal is recorded by the CCD array based spectrometer (USB2000, Ocean Optics). Information from the spectrometer is converted to give intensity vs. wavelength data. The user can use this data directly to plot the intensity for the whole spectrum or select a specific wavelength for a plot of intensity vs. cycle number. The sensitivity of the optical measurements can be adjusted according to the user specified integration time, the duration in which the spectrometer collects intensity data.

The Ranque-Hilsch vortex tube thermocycler is capable of operating as a portable device. The compact design of the thermocycler gives it overall dimensions of approximately 12 in x 8 in x 6 in. It also has very limited dependence on electricity and can be controlled using a laptop computer. In portable applications compressed gas is the limiting necessity, which needs to come from a bottle with enough capacity that the machine is capable of performing multiple runs.

The performance of the Ranque-Hilsch vortex tube thermocycler is demonstrated using a 96-bp λ-DNA amplicon. The sensitivity of the machine and the ability to monitor a PCR reaction real-time was tested by varying the initial DNA concentrations from 0.25 to 100 fg. Each reaction consisted of a hot start to activate the polymerase followed by 45 cycles between the denaturation, annealing, and elongation temperatures (95°C, 62°C, and 72°C, respectively) and had a total reaction time less than 12 min. Figure 5 shows the temperature vs. time profile for the hot start and initial three cycles of the PCR reaction.

Figure 6 shows that positive results were obtained for each initial concentration of λ-DNA while the negative controls (no initial λ-DNA) remained negative. This gel picture was used to conduct amplification and efficiency calculations to demonstrate machine sensitivity. An initial DNA amount of 0.25 fg produced an amplification of 2.7×10^{11}-fold, which corresponds to an overall efficiency of 79.5%.

The corresponding Real-Time PCR spectrometer data is shown in Figure 7. The PCR reaction is deemed successful when the intensity increases beyond an established threshold value defined as 150% of the baseline intensity. The number of cycles necessary to reach the threshold value increases as the initial DNA concentration is reduced and in the absence of primer-dimer artifacts, the negative control should not exceed the threshold value. Quantitative PCR is possible by calculating the initial concentration of DNA using the number of cycles necessary for the intensity to surpass the threshold value. The 0.25 fg DNA sample surpassed the threshold value 8 min into the reaction at cycle number 34.

The Ranque-Hilsch vortex tube thermocycler is capable of performing rapid PCR with real-time fluorescence-based DNA detection. It produces significant reaction yields with very small amounts of initial DNA. Positive results have been obtained from numerous tests amplifying a wide variety of DNA sources. Fluorescence data obtained throughout the reaction minimizes total assay time and can be used for quantitative PCR. Potential applications include point-of-care diagnostic testing, biological agent warfare detection, and virology, microbiology, and oncology research.

Financial support for this study from ARO under the supervision of Dr. James Gillespie is gratefully acknowledged.

References

[1] M. Krishnan, V. M. Ugaz, and M. A. Burns, Science **298**, 793 (2002).
[2] D. Braun, N. L. Goddard, and A. Libchaber, Phys. Rev. Lett. **91**, 158103 (2003).
[3] G. Ranque, J. Phys. Radium **4**, 112–114 (1933).
[4] R. Hilsch, Rev. Sci. Instrum. **18**, 108–113 (1947).
[5] M. Kurosaka, J. Fluid Mech. **124**, 139–172 (1982).
[6] B. K. Ahlborn, J. U. Keller, and E. Rebhan, J. Non-Equilib. Thermodyn. **23**, 159–165 (1998).
[7] B. K. Ahlborn *et al.*, J. Phys. D: Appl. Phys. **27**, 480–488 (1994).
[8] W. Frohlingsdorf and H. Unger, Int. J. Heat Mass Transfer **42**, 415–422 (1999).
[9] B. K. Ahlborn and J. M Gordon, J. Appl. Phys. **88**, 3645–3653 (2000).
[10] H. Mizuguchi *et al.*, J. Biochem. **126**, 762–768 (1999).

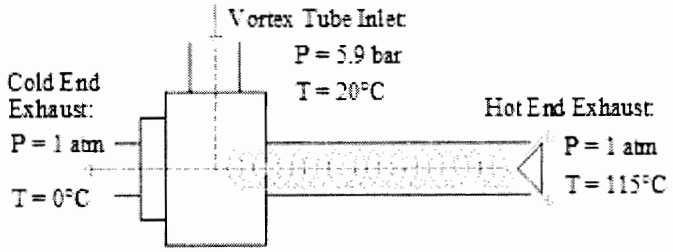

Figure 1: Ranque-Hilsch vortex tube conditions for basic thermocycler operation.

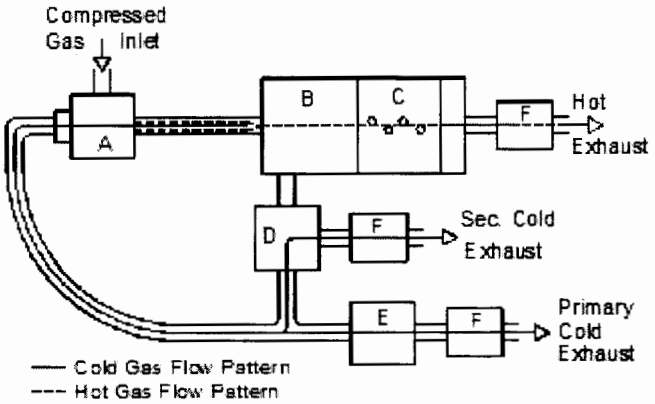

Figure 2: Flow pattern for sample heating: A. Ranque-Hilsch vortex tube, B. Vortex flow conditioner, C. Sample chamber, D. Cold flow valve, E. Cold release valve, F. Exhaust muffler.

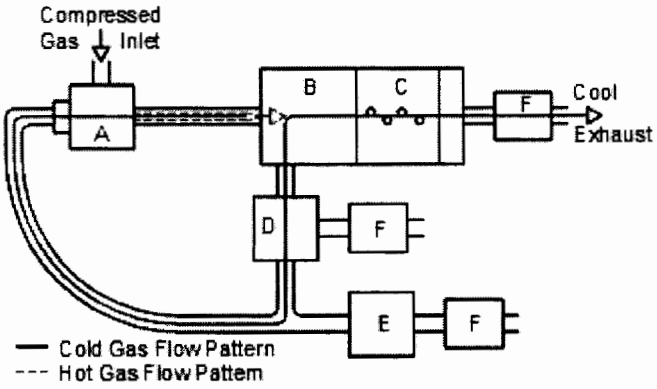

Figure 3: Flow pattern for sample cooling: A. Ranque-Hilsch vortex tube, B. Vortex flow conditioner, C. Sample chamber, D. Cold flow valve, E. Cold release valve, F. Exhaust muffler.

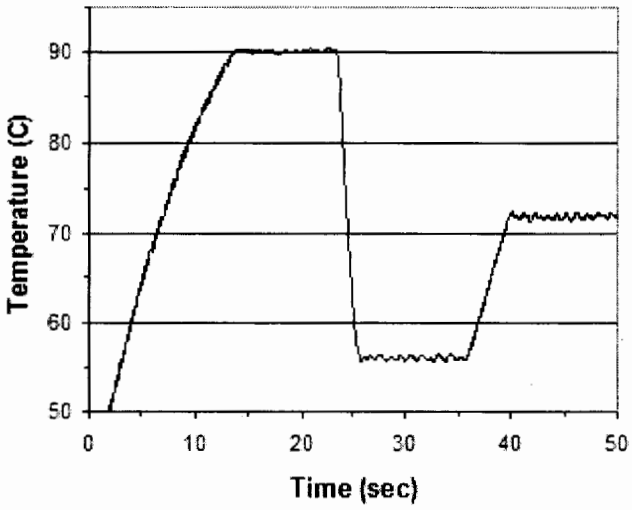

Figure 4: Typical PCR temperature holds: 90°C, 56°C, and 72°C for 5 s.

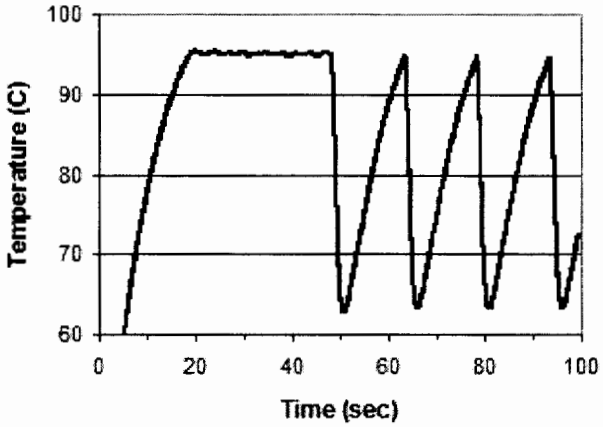

Figure 5: Temperature vs. time profile for PCR reaction: includes 30-s hot start followed by initial three cycles of the total 45 cycles programmed for 95, 62, and 72°C without temperature holds at these temperatures.

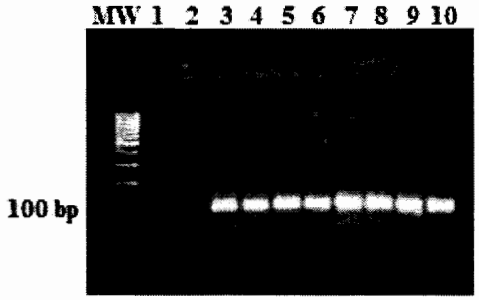

Figure 6: PCR amplification of 0 to 100 fg of 96 bp λ-DNA amplicon. MW: 100-bp molecular weight marker, 1 & 2: negative control, 3 & 4: 0.25 fg DNA, 5 & 6: 1 fg DNA, 7 & 8: 10 fg DNA, 9 & 10: 100 fg DNA.

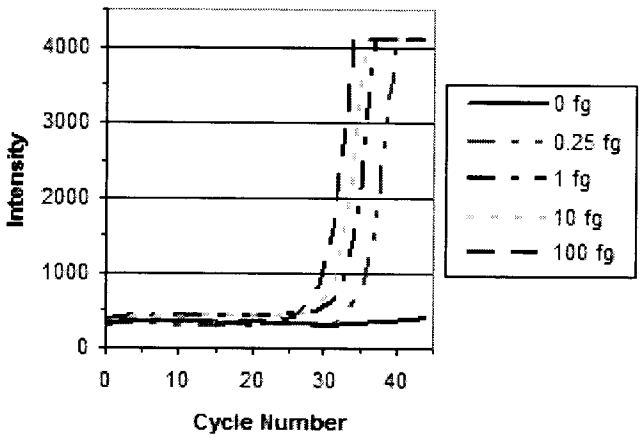

Figure 7: Spectrometer intensity vs. cycle number for increasing initial DNA concentrations.

^{1}H-NMR Study of the Structure of *C. antarctica* Lipase B in Hexane–Water Mixtures

Yvonne Hoffmann[3], Yu-Xi Gong[2], Om Prakash[2], Peter H. Pfromm[1], Mary E. Rezac[1], and Peter Czermak[3]

Departments of Chemical Engineering[1] and Biochemistry[2], Kansas State University, Manhattan, Kansas; University of Applied Sciences Giessen[3], Giessen, Germany

Abstract

Lipases can be used in nonaqueous solvents to catalyze esterification reactions. There are many reports in the literature that the small amounts of water dissolved in organic solvents like hexane have a significant influence on the reaction rates and enantioselectivity of lipase-catalyzed reactions in these solvents. However the molecular reasons for this have rarely been investigated. In this work a solubilized lipase in hexane at three water concentrations was investigated by ^{1}H-NMR. The purpose is to obtain first-hand information on the enzyme molecule exposed to different water concentration levels. Ultimately one would hope to discover the molecular-level reasons for significant differences in the initial rate of esterification catalyzed by a lipase in hexane at different water saturation levels. Solubilization of *Candida antarctica* lipase B in hexane was achieved. ^{1}H-NMR spectra of the surfactant coated lipase in hexane-d14 for nearly water-saturated hexane were gathered. Besides the peaks for the solvent and the surfactant, lipase peaks could be assigned. Peaks for the solvent and the surfactant could be found from 0 to 5.5 ppm. Lipase related peaks can also be found between 6 and 7.5 ppm where solvent and surfactant peaks do not interfere. Two spectra were acquired below water saturation at $a_W = 0.60$ and $a_W = 0.28$. Surfactant peaks are not clearly visible in the spectra. It was possible to assign some peaks to the lipase molecules, but an interpretation of the difference in signals at the different water activity levels investigated here appears premature.

Introduction

Initially it was proposed that enzymes need "essential water" to show catalytic activity in organic solvents [1]. It was shown later that enzyme activity depends on the thermodynamic water activity a_W (see below for definition) in organic solvents. Ducret et al. [2] showed that the enantioselectivity of *Candida antarctica* lipase B (CALB) in the esterification of (R,S)-ibuprofen ester depends on the water activity in the organic solvent. Kang et al. [3] have shown that the initial reaction rate for the esterification of geraniol to geranyl acetate catalyzed by Novozym 435 (immobilized *C. antarctica* lipase B on a macroporous acrylic resin) in hexane depends strongly on the thermodynamic water activity a_W in the system. There have been attempts to study the three-dimensional structure of enzymes in organic solvents via solubilization with surfactants [4]. Other approaches are to measure the enzyme hydration of enzymes suspended in organic solvents [5,6]. Attempts have been reported to quantify the hydration of the enzyme depending on the water activity in an organic solvent [7].

The motivation for this work presented here was to investigate the differences in the molecular arrangement in the enzyme molecule, when the enzyme molecule is exposed to hexane con-

taining dissolved water at different saturation levels.

Theoretical background

Nuclear Magnetic Resonance (NMR) spectroscopy

In a NMR experiment the molecule of interest is placed in a permanent magnetic field B_0 (Figure 1). This field polarizes the nuclear spins along the z-axis, resulting in a net macroscopic magnetization M. Another magnetic field B_1 applied in direction of the x-axis rotates M into the y-axis. As B_1 is turned off, the magnetization M decays with time and the system returns to the thermodynamic equilibrium situation with the magnetization orientated parallel to B_0 [8]. This relaxation (M_y) is acquired over time and is called free-induction decay (FID). The NMR spectrum is obtained by Fourier transformation (FT) of the FID. The chemical shift (Figure 1, frequency spectrum) of a proton depends on its environment. That means that nuclei, e.g. H, can be separated in the spectrum by their chemical environment. The different environment leads to different shielding constants for the protons and that causes different resonance frequencies (chemical shift in ppm).

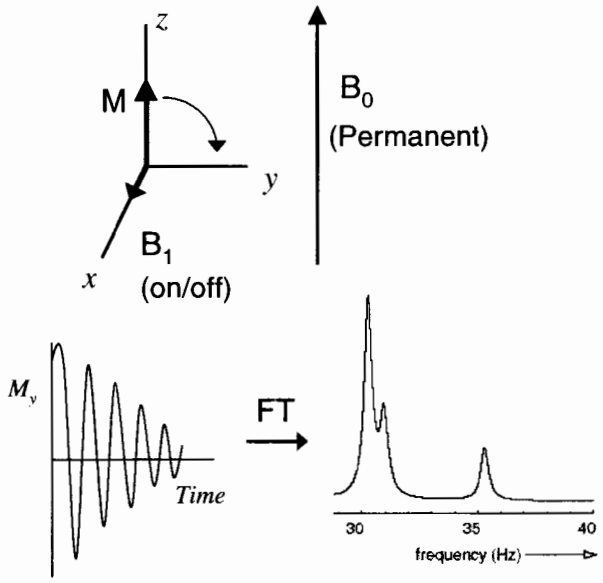

Figure 1. Effects of external magnetic fields on the proton, free-induction decay (FID) and frequency spectrum.

Definition of water activity

For our work it is necessary to clearly define the state of water saturation in a miscible hexane-water phase (single phase). The thermodynamic activity $\hat{a}_i$ shall be introduced here [9].

$$\hat{a}_i = \frac{\hat{f}_i}{f_i^{\circ}} \approx \frac{\hat{p}_i}{p_i^{\circ}} \qquad 1)$$

where $\hat{f}_i$ is the fugacity of component i in the mixture and f_i° is the fugacity of component i at a standard state. For low pressure and a perfect gas mixture the fugacity of a component in a liquid mixture is equal to its partial pressure. $\hat{p}_i$ is the partial pressure of component i in a mixture and p_i° is the partial pressure of component i at a standard state. The activity of water in hexane a_W will be used to quantify the dissolved water in hexane. One major advantage of a_W is that it is comparable for all solvents [10]. Another advantage is that in a multiphase system a_W is identical in all phases at equilibrium. That means if a_W is known for the solvent, a_W is known for the whole system at equilibrium [10].

Materials and Methods

Materials

Chemicals obtained from Fisher Scientific, Pittsburgh, PA, were hexane optima grade and hexane-d14 99.5% deuterated (termed hexane-d14). $CDCl_3$ 99.8% deuterated was obtained from Cambridge Isotope Laboratories, Andover, MA. Na_2HPO_4 (anhydrous) (≥99% pure) and $Na_2HPO_4 \cdot 2H_2O$ (≥99% pure) were obtained from Fluka, Buchs, Switzerland. The salt mixture of Na_2HPO_4 (anhydrous) and $Na_2HPO_4 \cdot 2H_2O$ is reported to result in a water activity of 0.163 at 25°C [11]. Hexane 99%+ pure was obtained from Sigma Aldrich, Milwaukee, WI. NMR indicated that cyclohexane was present in significant amounts. *n*-Hexane is the majority component. Span 60 from Sigma is an ester compound with a mixture of about 50% stearic (C18) and about 50% palmitic (C16) acid. Hydranal Coulomat AC, Hydranal Coulomat GC, and chloroform were obtained from Riedel-de Häen. Deionized water was used. It was prepared by reverse osmosis (Kenmore, reverse osmosis water filtration system, ULTRA Filter 300).

The chromatographically purified and not immobilized enzyme *C. antarctica* lipase B (CALB) batch 2003-25737 (about 100 mg) was a gift from Novozymes A/S, Bagsvaerd, Denmark. The enzyme was received as a frozen solution in about 40 ml aqueous buffer. As measured by the manufacturer it contained an activity of 1700 LU/ml (hydrolysis of tributyrin in aqueous solution at 30°C).

Instruments and glassware

Coulometric Karl Fischer titration was carried out with a titration module from Denver Instruments (Model 275KF titration module, Model 270 controller) [12]. The Karl Fischer anode solution was enriched with 10~20 vol% of chloroform (Riedel-de Haën) as recommended by Denver Instruments to solubilize the hexane in the samples [12]. Pasteur pipettes and NMR tubes (Standard NMR tube, 500 MHz, 3 mm O.D., length 7") were obtained from Wilmad-LabGlass, Buena, NJ. Screw-cap vials (4 ml, glass with plastic cap), microcentrifuge tubes (1.5 ml, polypropylene), a desiccator (Pyrex Brand Desiccator, I.D. 140 mm), a stir bar (Nalgene floating magnetic stir bar, $2\frac{1}{8}$ x $1\frac{1}{8}$"), and gastight sample-lock syringes (10 ml, Hamilton) were obtained from Fisher Scientific.

The as-received frozen lipase *C. antarctica* lipase B solution was taken from the –20°C freezer to –45°C in the freeze-drying chamber (VirTis 10-MR-TR, Gardiner, NY). To reach about –45°C the lipase was kept in the chamber for 30 min. Then the vacuum pump was turned

on. Overnight the lipase was dried at –45°C and about 160 mtorr. Then the lipase was heated to 25°C. The final conditions were 25°C and 160 mtorr. Overall, the freeze-drying procedures took at least 24 h.

CALB was solubilized as described elsewhere [13] and this solubilized CALB ($CALB_{sol}$) was used here without further treatment. This solubilization results in clusters of about 1200 lipase molecules solubilized by Span 60 (a nonionic surfactant).

^{1}H-NMR sample preparation

$CALB_{sol}$ and Span 60 in hexane-d14, a_W = 0.82. Hexane-d14 was saturated by adding excess deionized water into a screw cap vial. The vial was shaken for about 10 seconds and stored at room temperature T = 22 ± 2°C [12]. The samples (0.8 or 2.1 mg $CALB_{sol}$ or 1 mg Span 60 where weighed into a microcentrifuge tube or in a screw-cap glass vial. 300 □l hexane-d14 saturated with water were added with a micropipette. The mixture was transferred to a NMR tube with the Pasteur pipette. The tube was capped with a plastic cap and additionally with parafilm. The ^{1}H-NMR measurements were carried out at 40°C.

To calculate the thermodynamic water activity a_W for the NMR samples at 40°C, the saturation concentration for hexane is needed. Hexane optima grade can be used here as an indicator because this chemical is already described [12]. The average saturation concentration for hexane optima grade at 25°C is 87.9 ppm [12]. It is also reported that the water saturation concentration in hexane optima grade increases about 1.3 ppm/°C [12]. Therefore, a saturation concentration for water in hexane optima grade at 40°C can be calculated to be 107.4 ppm. The water activity for the procedure above would yield saturation at about 25°C (87.9 ppm) divided by saturation for 40°C (107.4 ppm). This results in a_W = 0.82. The saturation at 40°C is chosen as the standard state of the system. a_W will be always calculated as measured water content at about 25°C, divided by the saturation at 40°C.

$CALB_{sol}$ in hexane-d14 a_W < 1. Samples for measurements at a water activity < 1 were incubated in the setup shown in Figure 2. Samples were treated in this setup, either fresh-prepared by weighing 0.8 mg $CALB_{sol}$ into a screw-cap glass vial, adding 300–400 □l as-received hexane-d14 and mixing and transferring it with a Pasteur pipette into a NMR tube. Alternatively, the sample from the measurement for a_W = 0.82 was incubated in the desiccator after adding hexane-d14 to make up for evaporation.

The desiccator also contained 20 g Na_2HPO_4 (anhydrous) and 20 g $Na_2HPO_4 \cdot 2H_2O$ in the bottom part. The gas phase in the desiccator was agitated with a stir bar in the bottom. For reference there was also a vial (70–90 ml) with nondeuterated hexane in the desiccator. The hexane in this vial was of optima grade and was used as received. To monitor the change in water content in the hexane optima grade, coulometric Karl Fischer titration was carried out. The water content was measured on a daily basis until no change in the water content over 24 h could be observed.. Equilibrium was usually reached after about six days. After the NMR tubes were taken out of the desiccator, they were immediately capped with a septum (rubber, I.D. 3 mm). ^{1}H-NMR measure-

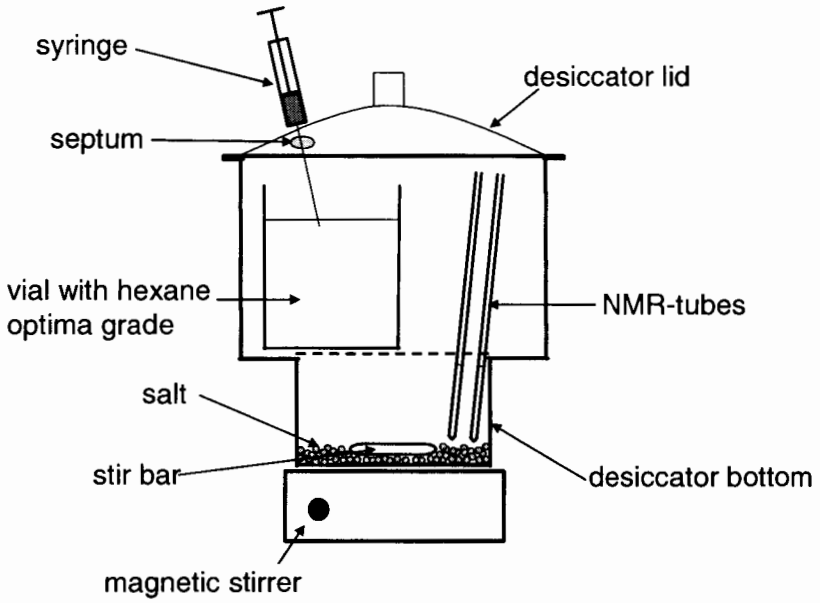

Figure 2. Setup for adjusting water activity in NMR samples, desiccator with stirrer, salt hydrates, a vial with hexane and NMR tubes in the bottom. Through the septum samples of hexane optima grade can be taken with a syringe to monitor the water content with Karl Fischer titration.

ments were carried out at 40°C.

NMR measurements

All high-resolution one- and two-dimensional ^{1}H-NMR experimental data were acquired with an 11.75 T Varian UNITYplus spectrometer (Varian, Palo Alto, CA), operating at 499.96 MHz for ^{1}H, with a 3-mm triple-resonance inverse detection probe. Using the above-described samples, spectra were recorded, processed and analyzed with Varian software VNMR6.1b on a Silicon Graphics (Mountain View, CA) Indigo^2 XZ workstation. After inserting the NMR tube containing the sample, the system needed to be tuned using tuning rods and locked via software to the frequency of the deuterated liquid. To get a clean ^{1}H-NMR spectrum the magnetic field around the sample is shimmed. In this step the inhomogeneous magnetic field is adapted to the sample to obtain a homogeneous magnetic field. After the shimming the parameters for the measurement (acquisition time, pulse width, relaxation delay) are set and the spectrum is acquired. The resulting spectrum is Fourier-transformed, phased (adjust zero-line), referenced (to a known chemical shift, i.e. $CDCl_3$ at 7.27 ppm) and the peaks are assigned to H-atoms that are present in the sample. The resulting spectrum can be processed either with the Varian software or with Mest-Rec Beta version 3.7.1 (Universidade de Santiago de Compostela, Santiago de Compostela, Coruna, Spain).

Results and Discussion

^{1}H-NMR spectra in organic solvents

Hexane in $CDCl_3$. To have a reference for all hexane-d14 spectra, a ^{1}H-NMR spectrum of

hexane 99%+ in $CDCl_3$ was taken. The spectrum was referenced to the solvent peak for proton-exchanged $CDCl_3$ at 7.27 ppm. The two $-CH_3$ groups of *n*-hexane can be assigned to a peak at 0.91 ppm (*n*-hexane at 20°C 0.89 ppm [14]), the four $-CH_2-$ groups to 1.31 ppm (1.28 ppm *n*-hexane at 20°C [14]). Due to a temperature change of 20°C the peak positions changed slightly for all hexane peaks.

Span 60 in hexane-d14. The next step towards a spectrum of solubilized CALB in hexane-d14 is a spectrum of just the surfactant in hexane-d14 (Figure 3). The spectrum shows again the characteristic peaks for *n*-hexane at 0.91 and 1.31 ppm, besides the peak intensity of those two peaks matches the ratio seen before of *n*-hexane in $CDCl_3$. Additionally there are peaks that can be assigned to Span 60. A book of 13C and 1H FT NMR spectra [14] shows peaks for sorbitan monostearate (component 1 in Figure 3) at 0.88, 1.25, 1.62, 2.33 and a lot of small peaks between 3.5 and 5.5 ppm. Peaks that need to be assigned have a chemical shift of 0.97, 1.39, 1.71, and 2.33 ppm and peaks between 3.5 and 5.5 ppm. Obviously some peaks drifted up to 0.14 ppm from their reported position. Other chemical shifts remain the same. Indeed the pattern of peak splitting and peak intensity appear very similar compared to the spectrum in the reference [14]. So, that it should be possible to assign the peaks as done above. Figure 4 emphasizes the region with peaks from 3.53 to 5.19 ppm. This region includes peaks for –OH, –COH, and $-CH_2-$ cyclic groups from Span 60. It shows that for $a_W = 0.82$ in hexane-d14 major peaks are at 3.73 and 4.24 ppm.

$CALB_{sol}$ in hexane-d14. For ^{1}H-NMR spectrum of $CALB_{sol}$ in hexane-d14 at a_w comparable to Figure 4, hexane-d14 was saturated with water (at about 22°C). This procedure was repeated two more times with different samples. The spectrum for $CALB_{sol}$ in hexane-d14 agrees with the Span 60 spectrum in hexane-d14. All large peaks for n-hexane and Span 60 match. The magnified spectrum (Figure 6) compared to the Span 60 spectrum shows more peaks for the $CALB_{sol}$ spectrum between 2.88 and 7.43 ppm. The appearance of more peaks and different positions can be easily attributed to a big variety of peaks that are visible in the aqueous CALB spectra (not shown here). Interestingly there is just one major peak in the region between 3.5 and 5.5 ppm, at 4.08 ppm (Figure 6). This peak can be found in the aqueous CALB spectra and is the main Cαpeak (structure in Figure 5). Another interesting fact is that now peaks are visible in the high-field frequency range above 5.5 ppm. These peaks do not interfere with any of the peaks of surfactant or solvent. The peak at 7.00 ppm does well correspond to the aqueous CALB spectra. Peaks between 6.0 and 8.0 ppm are assigned as amide peaks because the spectrum is taken in a fully deuterated solvent and the long collection time makes it less possible that here $-NH_3$ groups (labile protons) can be seen.

To collect ^{1}H-NMR spectra with $a_W << 1$, samples were incubated in a desiccator setup (described above). Figure 7 shows the ^{1}H-NMR spectrum that was taken after incubation of the samples in the desiccator (instead of salt the desiccator contained water to equilibrate to saturation). The hexane optima grade in the desiccator had a water content of 64.5 ppm (measured by Karl Fischer titration). For the measurement at 40°C, $a_W = 0.60$. In the ^{1}H-NMR spectrum of $CALB_{sol}$ in hexane-d14 (Figure 7), characteristic peaks for Span 60 disappear and the peak pattern for the solvent is altered (0 to 2.0 ppm). Between 2.27 and 6.18 ppm a significant number of very small peaks is visible. A strong peak at a chemical shift value of 2.27 ppm can be seen. This peak does not fit into the Span 60 pattern, but does fit into the pattern for CALB in aqueous sol-

ution (2.28 ppm, not shown here). Other peaks at 2.56, 4.08 (C_α main peak for CALB), 4.29, and 6.18 ppm could also be assigned to lipase peaks. In Figure 7 is no obvious evidence for existence of Span 60 in the ^{1}H-NMR spectrum.

Conclusions

NMR on the solubilized enzyme lipase B from *C. antarctica* appears to be a promising tool to investigate the interaction of enzymes with non-aqueous solvents. Molecular-level information

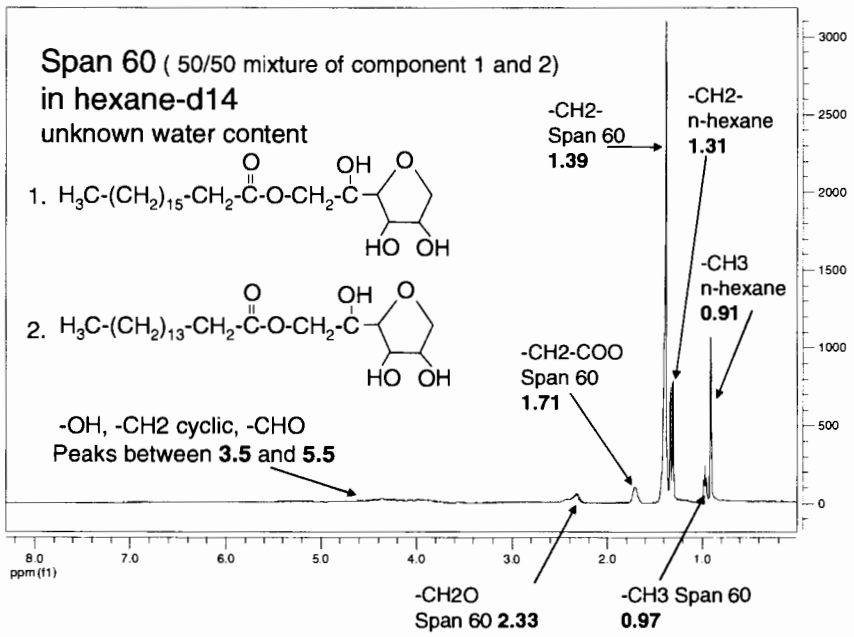

Figure 3. ^{1}H-NMR spectrum of Span 60 in hexane-d14 at 40°C. a_W is not controlled. Hexane-d14 was used as received.

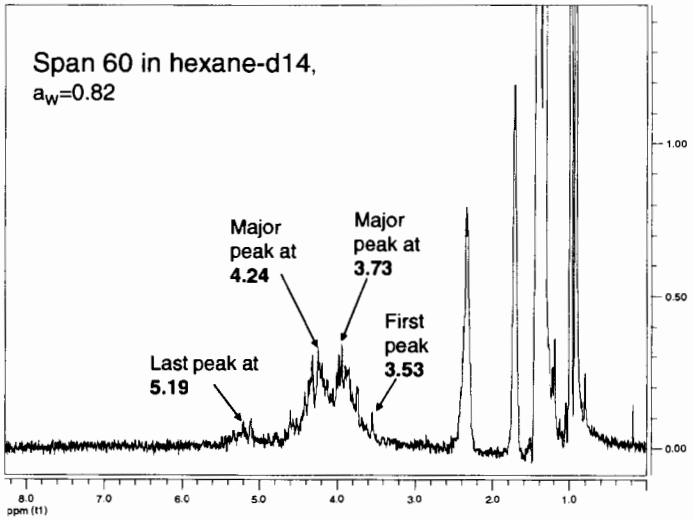

Figure 4. ^{1}H-NMR spectrum of Span 60 in hexane-d14 at 40°C, a_W = 0.82. Collection time 30 s.

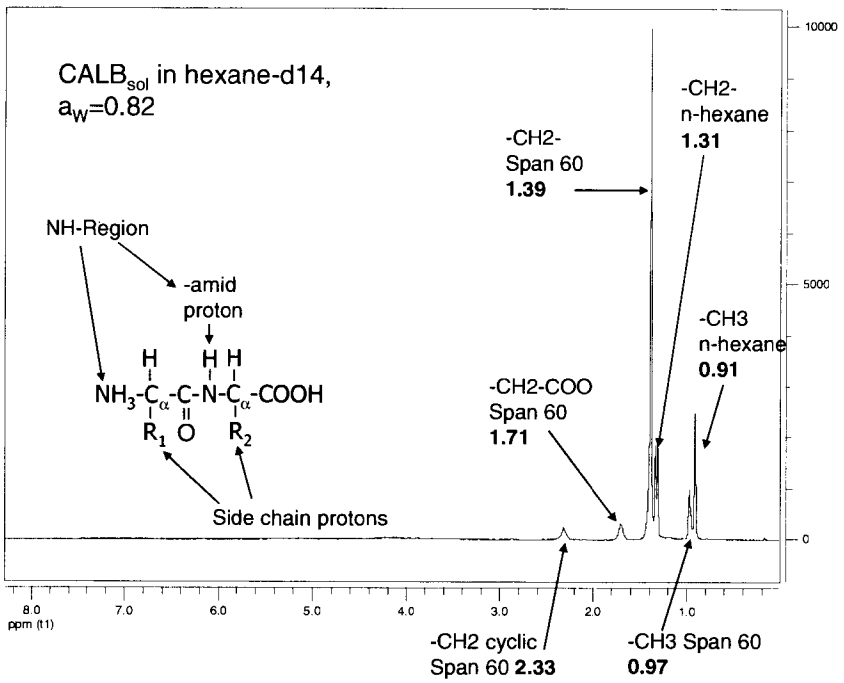

Figure 5. ^{1}H-NMR spectrum of CALB$_{sol}$ in hexane-d14 at 40°C, a_W = 0.82. The collection time was about 15 h.

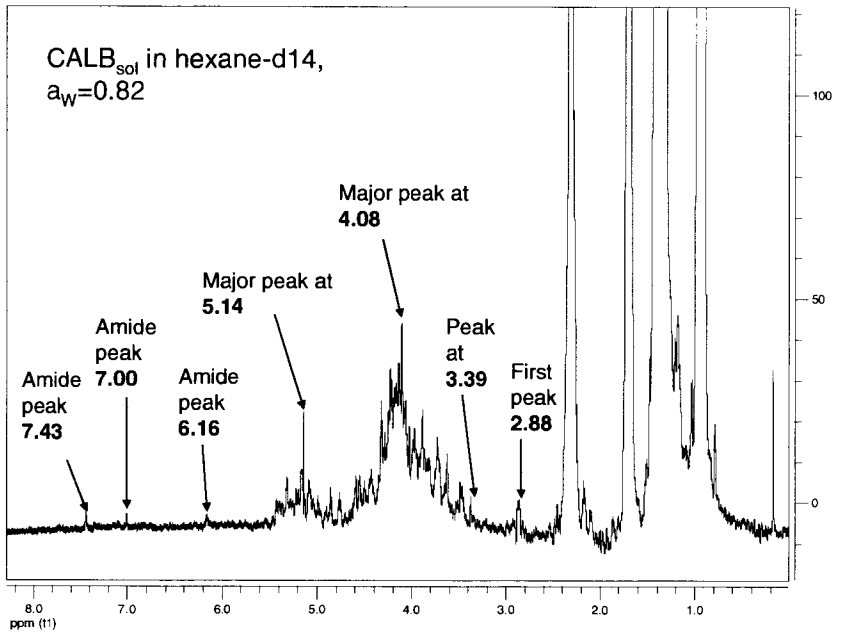

Figure 6. ^{1}H-NMR spectrum of CALB$_{sol}$ in hexane-d14 at 40°C, a_W = 0.82. Magnified ordinate of Figure 5.

from NMR could lead to an explanation of the strong dependence of enzyme kinetics on the thermodynamic water activity in the solvent. However, it seems necessary to perform future experiments with more advanced and more sensitive NMR hardware to obtain two-dimensional spectra of regions of the enzyme that directly take part in catalysis.

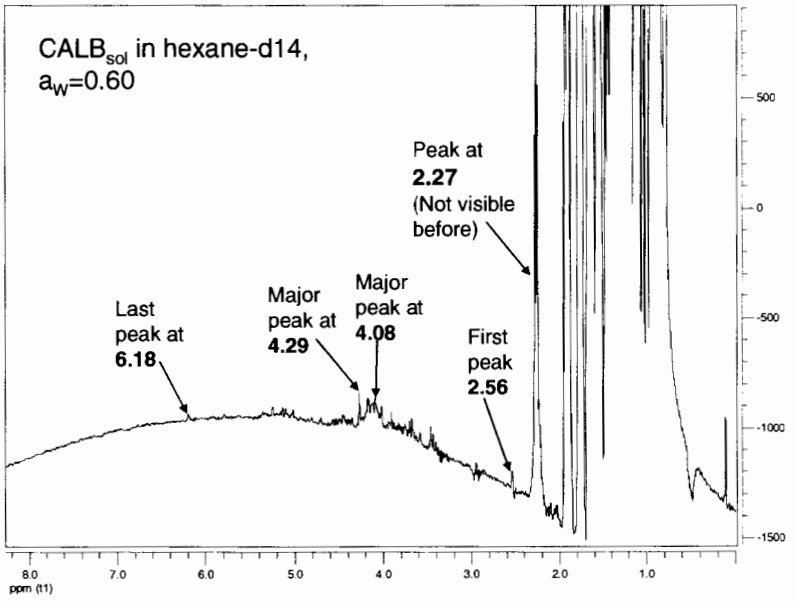

Figure 7. ^{1}H-NMR spectrum of CALB$_{sol}$ in hexane-d14 at 40°C, a_W = 0.60. The collection time was 8.5 h (experiment date 06/03/04).

References

1. Zaks, A. and A.M. Klibanov, The effect of water on enzyme action in organic media. J. Biol. Chem., 1988. 263: 8017–8021.
2. Ducret, A., M. Trani, and R. Lortie, Lipase-catalyzed entantioselective esterification of ibuprofen in organic solvents under controlled water activity. Enzyme Microb. Technol., 1998. 22: 212–216.
3. Kang, I.-J., P.H. Pfromm, and M.E. Rezac, Initial reaction rate of Novozym 435 depending on the water activity of the hexane reaction system. 2004, Data to be published.
4. Wangikar, P.P., P.C. Michels, D.C. Clark, and J.S. Dordick, structure and function of subtilisin BPN' solubilized in organic solvents. J. Am. Chem. Soc., 1997. 119: 70–76.
5. Lee, S.C., M.T. Ru, M. Haake, J.S. Dordick, J.A. Reimer, and D.S. Clark, Multinuclear NMR study of enzyme hydration in an organic solvent. Biotechnol. Bioeng., 1997. 57: 686–693.
6. Parker, M.C., B.D. Moore, and A.J. Blacker, Measuring enzyme hydration in nonpolar organic solvents using NMR. Biotechnol. Bioeng., 1995. 46: 452–458.
7. Hutcheon, G.A., M.C. Parker, and B.D. Moore, Measuring enzyme motility in organic media using novel h-d exchange methodology. Biotechnol. Bioeng., 2000. 70: 262–269.
8. Wüthrich, K., NMR of Proteins and Nucleic Acids. 1986, New York: Wiley.
9. Kyle, B.G., Chemical and Process Thermodynamics. Vol. 3. 1999, Upper Saddle River, NJ: Prentice-Hall.

10. Halling, P.J., Thermodynamic predictions for biocatalysis in nonconventional media: Theory, tests, and recommendations foe experimental design and analysis. Enzyme Microb. Technol., 1994. 16: 178–206.
11. Halling, P.J., Salt hydrates for water activity control with biocatalysts in organic media. biotechnol. techniques., 1992. 6: 271–276.
12. Kang, I.-J., M.E. Rezac, and P.H. Pfromm, Membrane permeation based sensing for dissolved water in organic micro-aqueous media. J. Membrane Sci., 2004, in press.
13. Hoffmann, Y. T., ^{1}H-NMR study of the structure of solubilized *C. antarctica* Lipase B in hexane-water mixtures, Diploma Thesis, 2004, University of Applied Sciences Giessen: Giessen, Germany.
14. Pouchert, C. and J. Behnke, Aldrich library of 13C and 1H FT NMR spectra. 1993, Milwaukee, WI: Aldrich Chemical Co.

Remediation Of Sites Contaminated By Oil Refinery Operations

S. Khaitan[1], S. Kalainesan[1], L. E. Erickson[1], P. Kulakow[2], S. Martin[3], R. Karthikeyan[4], S. L. L. Hutchinson[4], and L. C. Davis[5], Department of Chemical Engineering[1], Department of Agronomy[2], Center for Hazardous Substance Research[3], Department of Biological and Agricultural Engineering[4], and Department of Biochemistry[5], Kansas State University, Manhattan, KS 66506

Abstract

Around the world, the oil industry contributes to contamination of groundwater and aquifers beneath refineries and oil terminals. The successful remediation of a contaminated site requires understanding of the hydrogeology and the nature and extent of contamination. The physico-chemical and biological mechanisms that govern contaminant release, transport and fate in soils, sediments, and associated fluid phases must be understood and quantified. The available technologies and risk assessment to remediate former oil refinery sites contaminated by NAPLs are described in this paper. Emphasis is given to the most promising remediation techniques such as pump-and-treat, in situ soil washing, on site bioremediation and thermal-based technologies, such as steam-enhanced extraction. Further some of the alternative schemes suggested as enhancements to pump-and-treat techniques such as solvent flushing, polymer-enhanced flushing, and air stripping, are also discussed. Finally, important risk-based cleanup criteria associated with contaminated soil at refineries are presented.

Introduction

Some of the challenges faced during oil refinery site remediation are the inability to pump a significant fraction of the crude oil to the surface, low solubility of NAPLs in water forming a separate hydrocarbon phase, low hydraulic conductivity, and the need for early remediation considering economic viability. The purpose of this review is to provide a practical guide and listing of useful literature for those with petroleum-contaminated sites that need remediation.

A review of the published literature (1–46) has been completed to identify possible techniques to remediate oil refinery sites and spill sites. Remediation of a site contaminated by an oil refinery involves mainly the remediation of the zone contaminated by nonaqueous-phase liquids (NAPLs), including LNAPLs, nonaqueous-phase solids (NAPs), and DNAPLs. Petroleum refinery products and wastes such as gasoline, diesel, and jet fuels are some of the chemicals that fall into the category of NAPLs (21). Pools of NAPLs remain trapped in the subsurface and act as long-term sources of groundwater contamination (26). Several processes such as pump-and-treat, containment, and other groundwater flow modification processes, *in situ* biodegradation, phytoremediation, soil washing, air stripping, and thermal processes have been applied for the remediation of NAPL-contaminated sites (33,40). Soil vapor extraction and surface mobilization have been found to be effective for LNAPL remediation (8,14) while cosolvent and surfactant flushing have been considered in the case of DNAPL contamination (25).

Remediation Processes

In situ soil washing

This process is also termed flushing or flooding and involves the use of alkaline agents, hydrophilic cosolvents, viscosifiers and surfactants to enhance the removal of NAPL and its dissolved contaminants. NAPL flow may be enhanced by altering viscosity or by increasing solubil-

ity. Addition of water-soluble polymers increases the viscosity of the water phase. Addition of surfactants and certain other solvents increases the solubility of NAPLs in the water phase and often decreases the viscosity of the NAPL phase. Alkali agents, hydrophilic cosolvents and surfactants are some of the chemical compounds added to increase the mobility of NAPLs. The type of chemical agent added to improve the mobility of the front depends on the nature and composition of the NAPL. High-pH alkaline agents tend to saponify carboxylic acids, phenols, and asphaltenes contained within heavy oils and certain NAPLs into natural surfactants, which lowers interfacial tension, thereby increasing mobilization of NAPL. Alkaline addition alters wettability and disrupts adsorption, precipitation and ion exchange processes that contribute to the high surfactant losses. Hence alkaline addition also serves as a complement to surfactant flooding (40). Addition of hydrophilic cosolvents (short-chain alcohols, ethers, and ketones) reduces interfacial forces. A major concern with DNAPL remediation by cosolvent flooding is the mobilization of DNAPL, causing it to sink and contaminate deeper aquifer units. The use of low-density cosolvents, which preferentially partition into DNAPL and cause reversal of density differences between the DNAPL and aqueous phases, is a potential answer to this concern (40).

Water flooding and pump-and-treat

Pump-and-treat and water flooding are options generally considered when considerable volume of NAPL is present in the subsurface (40). Pump-and-treat technology attempts to keep the plume from spreading and to remove the contaminants by physical processes (32). In this method pumps are commonly used to bring polluted ground water to the surface where it can be treated more easily. To remove polluted water an extraction system with one or more wells or trenches equipped with pumps is built. Polluted water is pumped out through the extraction wells and is sent to a treatment scheme before the water is discharged (38). The use of pump-and-treat with interceptor trenches helps to lower the water table, to enhance flushing, to control the flow, and to enhance biodegradation by having more oxygen delivered through gas-phase diffusion in the enlarged vadose zone. Some of the common methods used for treating the extracted water include phase separation, aerobic biodegradation, air stripping, and liquid-phase granular activated charcoal adsorption (42). Useful product recovery can pay for the initial operation of the extraction system. The well design, pumping system, and treatment depend on the site characteristics and contaminant required. The wells may be screened at different levels to maximize effectiveness. Generally a monitoring program is set up to determine the effectiveness of pumping, and hence to decide when and how to turn off and turn on wells and also make adjustments to the system in response to changes in subsurface conditions (46).

In situ biodegradation

In situ biodegradation involves the partial or complete degradation of aqueous phase compounds by microorganisms in the subsurface. It requires adequate aquifer permeability (hydraulic conductivity, $>10^{-6}$ m/s), a suitable microbial population, sufficient hydrodynamic control of the plume, and delivery of required oxygenates and nutrients (17).

One of the factors limiting the process of bioremediation is the availability of nitrogen and phosphorus in soil. The addition of nitrogen fertilizer enhances the bioremediation of hydrocarbon contamination in soil environments (31, 19). A site must be optimally fertilized to support plant growth and to maximize an active microbial population capable of degrading the contaminants. As reported, nutrients are generally added in a carbon:nitrogen: phosphorus mass ratio of 100:10:1 (20).

In situ biodegradation has the following disadvantages: Degradation rates usually decrease

with decreasing compound concentration so complete biodegradation of contaminants is potentially unattainable. Extensive site heterogeneities may also affect the efficiency of this process (13). Though biodegradation is a potentially powerful process, its performance evaluation is rather difficult. Inherent uncertainties created by aquifer and contaminant heterogeneities, inaccessibility for observation, expense of sampling and limitations of some measurements make evaluation challenging and controversial (36).

Phytoremediation

Phytoremediation is an effective method for the remediation of petroleum hydrocarbons (4,19,33). This technology is most suitable for sites with shallow contamination of organic, nutrient, or metal pollutants that are amenable to transformation, stabilization, extraction or filtration by plants or their root systems (11,37). Several studies have shown that phytoremediation requires several years to achieve the desired reductions in many applications (27,33). A positive feature of phytoremediation is that the planted vegetation may act to contain the contaminants within the region where they are found by evapotranspiring any precipitation, which infiltrates the soil (11). In addition, contaminants released to the atmosphere are frequently transformed to acceptable end-products in the atmosphere (28,45). The only disadvantage of phytoremediation is that it requires a long-term management for significant reductions in contaminant concentrations, but otherwise phytoremediation is an inexpensive, esthetically pleasing, and effective alternative for the remediation of petroleum contaminants (4,19,37,42).

Steam-enhanced extraction

Soil heating is also a promising technique for NAPL remediation (15). The advantages of thermal processing are modest cost and simple equipment requirements (22). Some of the *in situ* thermal remediation methods currently prevalent are steam injection, hot water injection, and electrical heating (10). A major risk associated with steam or hot water injection is that the contaminant may be displaced by the injected fluid to areas other than the recovery points; for instance, DNAPL may be mobilized downwards due to steam injection. Nevertheless steam-enhanced extraction has been very effective in laboratory studies and in field demonstration for the remediation of toxic compounds from soil and groundwater (41). Steam-enhanced extraction involves steam injection in a cyclic manner after the soils reach steam temperatures. Cyclic steam injection enhances mass transfer and accelerates cleanup (41). This is analogous to the oil industry practice of using steam for enhanced oil recovery. Turning the steam off allows soil pressure to decrease, allowing vapors to dissipate. A dramatic increase in hydrocarbon recovery following steam shutdown has been observed (1). A review of the literature reveals that steam-enhanced extraction, though still in the experimental stage, appears to be a promising technique for the remediation of NAPL-contaminated sites.

Enhancements to Pump-dnd-Treat Process

Polymer-enhanced flushing

Injecting hydrophilic polymers (cationic and anionic polyacrylamide) is especially suited for the flushing of NAPL or dissolved components from low-permeability zones. Polymer injection leads to the modification of permeability to obtain a more effective flushing process. In heterogeneous aquifers, the permeability of water is high in the high-permeability zones and low in the low-permeability zones. When a small quantity of polymer is injected into the aquifer, it penetrates to a greater extent into the high-permeability zones than into the low-permeability zones.

This would mean that pumped water can flush NAPL more effectively and that the NAPL-water contact time is also increased, increasing the dissolution of NAPL constituents (9).

Air stripping

Another remediation technology to use with pump-and-treat is air stripping. In this method, the contaminated water is often passed through preheater heat exchangers and then through an air stripper (18), where vapors containing petrochemicals are separated from water. The treated water may be passed through charcoal filters for further purification. The petrochemical vapors are often combusted using natural gas, and then passed through scrubbers to remove compounds such as hydrogen chloride, before being exhausted into the atmosphere. This process is powerful and practically removes all volatile petrochemicals. Further it is economical for high flow rates and high concentrations (12).

Other processes

Pump-and-treat processes often are combined with other processes including air sparging (34,35), bioslurping (43,44), bioremediation (35), and photoremediation (27,33). Air sparging is used to provide oxygen to the saturated zone to increase the rate of *in situ* biodegradation (34, 35). It can also be used to move volatile compounds into the gas phase so that they can be removed from the aquifer (16). Bioslurping (43,44) combines bioventing, soil vapor extraction and vacuum-enhanced free product recovery in an integrated operational process.

Remediation End Points

There has been significant progress with respect to the acceptable endpoints associated with petroleum-contaminated soil and water. There are drinking water maximal contaminant levels for specific organic compounds; for the U.S. Safe Drinking Water Act, benzene is 0.005 mg/L; toluene is 1 mg/L; ethylbenzene is 0.7 mg/L; and total xylenes are 10 mg/L, for example (2). Releases of groundwater from a contaminated site must meet the water quality requirements associated with the site. The regulatory requirement may vary from state to state and from country to country; however, there is a movement toward risk-based standards as well as a movement toward standards for specific compounds rather than standards for total petroleum hydrocarbons (2,3,7).

Risk assessment is an attempt to quantify the likelihood and severity of potential hazards to human health. It includes hazard identification, exposure assessment, dose-response assessment, and risk characterization (7). The U.S. Environmental Protection Agency and many state governments have implemented risk assessment frameworks and standards for risk-based corrective action for petroleum releases to soil and water based on procedures developed by ASTM (2,3,7). In this process the contaminants associated with the soil as well as those in the water phase are considered. For soil the pathways "soil to human being", "soil to plant", and "soil to groundwater" are often considered (33). The soil should be restored such that it can function effectively for a useful application that is appropriate for the site. If it is to be used for agronomic activities, the physical and chemical properties should be restored to conditions such that useful crops with acceptable chemical profiles are produced (19). For petroleum compounds in soil and water, the BTEX compounds and the polynuclear aromatic hydrocarbons (PAHs) are generally included in any risk-based analysis of acceptable end points (2). While the solubility of PAH compounds in water is quite low, the drinking water standards for these compounds are also very low. For example, the U.S. Safe Drinking Water concentration for benzo(a)pyrene is 0.0002 mg/L or 200 ng/L (2). When surfactants and/or other petroleum compounds are present, the solubility in water

and the bioavailability of PAH compounds are altered (19, 33, 27).

Case Studies

There are a number of field studies where petroleum-contaminated soil and/or aquifers are being remediated (4,6,19). For closed oil refinery sites, pump-and-treat often yields sufficient quantities of hydrocarbon products to pay for a recovery process consisting of recovery wells and interceptor trenches with pump-and-treat for plume control. Physical separation of the oil phase followed by biological treatment of the water phase is commonly found at these sites. The interceptor trenches and pumping lowers the water table and provides a good environment for biodegradation in the unsaturated zone. Vegetation has been established on closed refinery sites to have nature help with the pump-and-treat process (34,39). Field tests of phytoremediation of petroleum hydrocarbons in surface soil were conducted at 13 locations in North America under the Remediation Technologies Development Forum (5,23,24). Petroleum-contaminated surface soil at the refinery sites in the RTDF program were the most heterogeneous sites in the RTDF program and included soil samples with up to 10% hydrocarbons. After three years of monitoring of the RTDF field trials at refineries, it was usually not possible to conclude there were significant reductions in hydrocarbon concentrations due to phytoremediation treatment. In two RTDF field tests that had initial hydrocarbon contaminants with high bioavailability, short-term phytoremediation treatment was promising. Use of vegetation at many refinery locations may be most useful for establishing vegetative cover and stabilizing soils without expectations of short-term reductions in hydrocarbons. Forensic analyses of hydrocarbon concentrations at industrial sites suggest that vegetation may facilitate slow biodegradation over a period of decades (29, 30).

Remediation of a closed petroleum refinery site – A case study

A site adjacent to a major river in the Midwest was used for petroleum refining until about 1980. A hydrocarbon and groundwater recovery system has recovered approximately 1.7 million gallons of petroleum products in more than 15 years of operation. The recovery operation has provided plume containment at the site. In the recovery process, the oil is separated from the water and the water is aerated and biologically treated in an 850,000-gallon aeration tank and a 150,000-gallon polishing tank.

In 1998, natural vegetation at the site was evaluated, and a plot of hybrid poplar trees was planted. One of the purposes of the trees is to help with the pump-and-treat process. The quantity of water removed by pumping from the start of recovery operations in 1984 through the end of 1996 was 7.24 billion gallons (6). This is about 0.6 billion gallons/year or about 7 ft^3/ft^2 per year for the 270-acre site. This pumping rate exceeds the annual precipitation of approximately 37 inches per year because of the desire to contain the contaminants on the property. The contaminants of concern at this site include benzene and PAH compounds. Under natural groundwater flow, water from the site flows into the large river. For benzene, there is rapid aerobic biodegradation when aerobic conditions are present and concentrations of inorganic nutrients are sufficient. Models can be used to estimate the benzene concentration as a function of position for the conditions that would result when the pump-and-treat system is turned off and the trees are used to reduce the flow toward the river.

Biodegradation is one of the processes that are continuing at this site. The groundwater pump-and-treat process is also removing some contaminants from the site. The vegetation and the pumping help to remove water and lower the water table, which enhances oxygen transfer to the unsaturated zone. This should enhance the rate of biodegradation in the unsaturated zone.

Conclusion

A review of literature reveals significant progress in the technologies available for the remediation of NAPL contaminated sites. Site heterogeneities, contaminant type and the extent of contamination make it necessary for each remediation scheme to be designed specifically for the contaminated site chosen for remediation. A thorough study of the contaminated site may go a long way in helping to identify the appropriate combination of remediation techniques. Remediation technologies such as cosolvent flushing, especially *in situ* alcohol flushing and steam-enhanced extraction, appear to be promising techniques for the remediation of NAPL-contaminated sites. Application of a combination of techniques such as a physical process with bioremediation and phytoremediation may also offer a better remediation solution. Though current technologies offer a range of remediation options that are sufficient for the cleanup of a contaminated site, the efficiency of these processes is affected by site conditions, financial limitations, and time duration available for cleanup. Further research in this field is needed to identify technologies that offer cost-effective solutions that can be implemented. Further research on acceptable endpoints is also needed.

References

1. Adams, T. V., and G. J. Smith, "DNAPL/LNAPL Remediation In Clay Till Using Steam Enhanced Extraction," Physical, Chemical and Thermal Technologies: Remediation of Chlorinated and Recalcitrant Compounds, G. E. Wickramanayake and R. E. Hinchee, Eds., Battelle Press, Columbus, OH, pp. 103–108 (1998).
2. American Society for Testing Materials (ASTM), Standard Guide for Risk-Based Corrective Action Applied at Petroleum Release Sites, ASTM Designation E 1739-95, Pleasanton, CA (1995).
3. American Society for Testing Materials (ASTM), Standard Guide for Risk-Based Corrective Action, ASTM Designation E 2081-00, Pleasanton, CA (2000).
4. Banks, M. K., P. Schwab, B. Liu., P. Kulakow, J. S. Smith, and R. Kim, "The Effect of Plants on the Degradation and Toxicity of Petroleum Contaminants in Soil: A Field Assessment," Advances in Biochemical Engineering Biotechnology, T. Scheper and D. T. Tsao., Eds., Springer-Verlag, New York, pp. 75–96 (2003).
5. Camp, H., P. Kulakow, D. R. Smart, and K. O'Reilly. 2003. Application of Chemical Tools to Evaluate Phytoremediation of Weathered Hydrocarbons. Proceedings of the Twenty-Fifth Arctic and Marine Oilspill Program Technical Seminar, Environment Canada, Calgary, AB.
6. CH2MHill, Comprehensive Investigation Report, Former Phillips Petroleum Refinery, Kansas City, Kansas, May 1997.
7. Chen, K. F., L. C. Wu, C. M. Kao, and C. C. G. Yang, "Application of Health Risk Assessment to Derive Cleanup Levels at a Fuel-Oil Spill Site, *Practice Period. Hazard. Tox. Radioact. Waste Management*, **8**, 99–104 (2004).
8. Chevalier, L. R., Wallace, B. R., Wiggert, D. C., Shabana, M. D., "2-D Experimental Investigation of Surfactant Mobilization of Non Aqueous Phase Liquid," Non-Aqueous Phase Liquids (NAPLs) in Subsurface Environment: Assessment and Remediation, L. N. Reddi, Ed., American Society of Civil Engineers, New York, p. 357 (1996).
9. Darwish, M. I. M., J. E. McCray, P. K. Currie, and P. L. J. Zitha, "Polymer-Enhanced DNAPL Flushing from Low-Permeability Media: An Experimental Study," *Ground Water Monit. Remed.*, **23**, 92–101 (2003).
10. Davis, E. L., and G. Heron, "Research Issues For Thermal Remediation," Physical, Chemical

and Thermal Technologies: Remediation of Chlorinated and Recalcitrant Compounds, G. E. Wickramanayake and R. E. Hinchee, Eds., Battelle Press, Columbus, OH, pp. 49–55 (1998).
11. Davis, L. C., S. Castro-Diaz, Q. Zhang, and L. E. Erickson, "Benefits of Vegetation for Soils with Organic Contaminants," Crit. Rev. Plant Sci., **21**, 457–491 (2002).
12. Elgal, G. M., "Petrochemical Removal From Contaminated Wells," Physical, Chemical and Thermal Technologies: Remediation of Chlorinated and Recalcitrant Compounds, G. E. Wickramanayake and R. E. Hinchee, Eds., Battelle Press, Columbus, OH, pp. 187–198 (1998).
13. Früchtenicht, H., and T. Held, "Microbiological *In Situ* Remediation of an Aquifer Contaminated with Waste Oil from a Refinery," Groundwater Quality: Remediation and Protection (Proceedings of the Prague Conference, May 1995). IAHS Publ. No. 225, 1995.
14. Haimann, R., K. Schoen, M. Underwood, J. Munic, and J. Hartley, "Designing SVE to Remove Volatile LNAPLs," Non-Aqueous Phase Liquids (NAPLs) in Subsurface Environment: Assessment and Remediation, L. N. Reddi, Ed., American Society of Civil Engineers, New York, p. 431 (1996).
15. Heron, G., T. H. Christensen, M. Van Zutphen, and C. G. Enfield, "Soil Heating For Remediation Of Dissolved Trichloroethylene In Low-Permeable Soil," Physical, Chemical and Thermal Technologies: Remediation of Chlorinated and Recalcitrant Compounds, G. E. Wickramanayake and R. E. Hinchee, Eds., Battelle Press, Columbus, OH, pp. 37–42 (1998).
16. Hinchee, R. E., Air Sparging for Site Remediation, CRC Press, Boca Raton, FL (1994).
17. Hinchee, R. E., J. A. Kittel, and J. H. Reisinger, Applied Bioremediation of Petroleum Hydrocarbons, Battelle Press, Columbus, OH (1995).
18. Hoffman, A. H., "Pump-and-Treat May Be the Solution," Physical, Chemical and Thermal Technologies: Remediation of Chlorinated and Recalcitrant Compounds, G. E. Wickramanayake and R. E. Hinchee, Eds., Battelle Press, Columbus, OH, pp. 181–186 (1998).
19. Hutchinson, S. L., A. P. Schwab, and M. K. Banks, "Biodegradation of Petroleum Hydrocarbons in the Rhizosphere," Phytoremediation Transformation and Control of Contaminants, S. C. McCutcheon and J. L. Schnoor, Eds., Wiley, Hoboken, NJ, pp. 355–386 (2003).
20. Hutchinson, S. L., M. K. Banks, and A. P. Schwab, "Phytoremediation of Petroleum Sludge: Impact of Inorganic Fertilizer," *J. Environ. Qual.*, **30**, 395–403 (2001).
21. Illangasekare, T. H., "Non-Aqueous-Phase Fluids in Heterogeneous Aquifers–Experimental Study," *J. Environ. Eng.*, **121**, 571–579 (1995).
22. Kawala, Z., and T. Atamanczuk, "Soil Vapor Extraction Enhanced By Microwave Energy," Physical, Chemical and Thermal Technologies: Remediation of Chlorinated and Recalcitrant Compounds, G. E. Wickramanayake and R. E. Hinchee, Eds., Battelle Press, Columbus, OH pp. 43–48 (1998).
23. Kulakow, P. 2000. Annual Report of the RTDF Phytoremediation Action Team TPH Subgroup Cooperative Field Trials, Remedial Technologies Development Forum, 132 pages, URL: http://www.engg.ksu.edu/HSRC/RTDFtphrp1.html.
24. Kulakow, P. A., L. E. Erickson, and B. A. Leven, "A Nationwide Field Test of Phytoremediation for Petroleum Contaminated Soils," Proceedings of the Seventh International Petroleum Environmental Conference, K. L. Sublette, Ed., University of Tulsa, Tulsa, OK, pp. 720–733 (2000).
25. Kulasooriya, I., K. Soga, D. Dai, and T. H. Illangasekare, "Effect of Flow Direction on Surfactant Enhanced Remediation of DNAPL," *Environ. Geotech.*, **4**, 829–834 (2002).
26. Manivannan, I., Powers, S. E., and G. W. Curry, Jr., "Dissolution Of NAPLs Entrapped in

Heterogenous Porous Media," Non-Aqueous Phase Liquids (NAPLs) in Subsurface Environment: Assessment and Remediation, L. N. Reddi, Ed., American Society of Civil Engineers, New York, p. 563 (1996).
27. McCutcheon, S. C., and J. L. Schnoor, Eds., Phytoremediation: Transformation and Control of Contaminants, Wiley, New York (2003).
28. Narayanan, M., L. E. Erickson, and L. C. Davis, "Simple Plant Based Design Strategies for Volatile Organic Pollutants," *Environ. Prog.*, **18**, 231–242 (1999).
29. Olson, P. E., and J. S. Fletcher, "Ecological Recovery of Vegetation at a Former Industrial Sludge Basin and Its Implication to Phytoremediation," *Environ. Sci. Pollut. Res.*, **7**, 195–204 (2000).
30. Olson, P. E., J. S. Fletcher, and P. R. Philip, "Natural Attenuation/Phytoremediation in the Vadose Zone of a Former Industrial Sludge Basin," *Environ. Sci. Pollut. Res.*, **8**, 243–249 (2001).
31. Rasiah, V., R. P. Voroney, and R. G. Kachanoski, "Biodegradation of an Oily Waste as Influenced by Nitrogen Forms and Sources," *Water Air Soil Pollut.*, **65**, 143–151 (1992).
32. Ratnam, S., Culligan-Hensley, P.J., Germaine, J.T., "Modeling the Behavior of LNAPLs Under Hydraulic Flushing," Non-Aqueous Phase Liquids (NAPLs) in Subsurface Environment: Assessment and Remediation, L. N. Reddi, Ed., American Society of Civil Engineers, New York, p. 595 (1996).
33. Reible, D., and K. Demnerova, Innovative Approaches to the On-Site Assessment and Remediation of Contaminated Sites, Kluwer, Boston, 2002.
34. Retec Group, Inc. Biosparging and MNA Sampling for the Phase I Norledge Area Technical Memorandum, BP Products North America, Sugar Creek, MO, 2004.
35. Retec Group, Inc. Norledge Area Corrective Measures Study Addendum Phase 2 Area Redesign, BP Products North America, Sugar Creek, MO, 2002.
36. Seagren, E. A., D. A. Stahl, and B. E. Rittmann, "Innovative Evaluation Methods for Bioremediation," Non-Aqueous Phase Liquids (NAPLs) in Subsurface Environment: Assessment and Remediation, L. N. Reddi, Ed., American Society of Civil Engineers, New York, p. 381 (1996).
37. Stehmeier, L. G., S. Leong., M. Salam, F. VanDelft, J. Kuhwald, and M. McD. Francis, "Phytoremediation of Oil-Contaminated Soil for Landfarm Sustainability," Phytoremediation, Wetlands, and Sediments, A. Leeson, E. A. Foote, M. K. Banks, and V. S. Magar, Eds., Battelle Press, Columbus, OH, pp. 53–60 (2001).
38. Theis, T. L., D. M. O'Carroll, D. C. Vogel, A. B. Lane, and K. Collins, "Systems Analysis of Pump-and-Treat Groundwater Remediation," *Practice Period. Hazard. Tox. Radioact. Waste Management*, **7**, 177–181 (2003).
39. Tritechnics Corporation. RCRA Facility Investigation Report Amoco Sugar Creek Former Refinery, Amoco Corporation, Sugar Creek, MO, 1995.
40. Udell, K. S., D. G. Grubb, and N. Sitar, "Technologies For In Situ Cleanup of Contaminated Sites," *Cent. Eur. J. Public Health*, **3**, 67–76 (1995).
41. Udell, K. S., and R. L. McCarter, "Steam Enhanced Extraction Of Wood Treatment Chemicals From Soils," Physical, Chemical and Thermal Technologies: Remediation of Chlorinated and Recalcitrant Compounds, Eds: G. E. Wickramanayake and R. E. Hinchee, Eds., Battelle Press, Columbus, OH, pp. 121–126 (1998).
42. Winnike-McMillan, S. K., Q. Zhang, L. C. Davis, L. E. Erickson, and J. L. Schnoor, "Phytoremediation of Methyl Tertiary-Butyl Ether, " Phytoremediation Transformation and Control

of Contaminants, S. C. McCutcheon and J. L. Schnoor, Eds., Wiley, Hoboken, NJ, pp. 805–828 (2003).
43. Yen, H. K., and N. B. Chang, "Bioslurping Model for Assessing Light Hydrocarbon Recovery in Contaminated Unconfined Aquifer: I. Simulations Analysis," *Practice Period. Hazard. Tox. Radioact. Waste Management*, **7**, 114–130 (2003).
44. Yen, H. K., and N. B. Chang, "Bioslurping Model for Assessing Light Hydrocarbon Recovery in Contaminated Unconfined Aquifer: II. Optimization Analysis," *Practice Period. Hazard. Tox. Radioact. Waste Management*, **7**, 131–138 (2003).
45. Zhang, Q., L. C. Davis, and L. E. Erickson, "Transport of Methyl *tert*-Butyl Ether through Alfalfa Plants," *Env. Sci. Technol.*, **35**, 725–731 (2001).
46. http://www.clu-in.org/download/citizens/pump_and_treat.pdf.

Biodegradation of Tertiary Butyl Mercaptan in Soil under Aerobic Conditions

S. Kalainesan[1], L.E. Erickson[1], S. L. L. Hutchinson[2] and R. Karthikeyan[2]
Departments of Chemical Engineering[1] and Biological and Agricultural Engineering[2], Kansas State University, Manhattan, KS 66506

Abstract

Tertiary butyl mercaptan (TBM) is a malodorant that is added to natural gas in small quantities to aid in its detection. The objective of this study is to investigate the biodegradation of TBM in soil water system under aerobic conditions. To study the biodegradation of TBM, simple microcosms were set up with 10 g agricultural soil, 10 mL water and 10 µL TBM in 160-mL serum bottles. The headspace in the microcosm was calculated to be sufficient for complete biodegradation of TBM under aerobic conditions. The biodegradation of TBM was studied by monitoring the reduction of TBM in the headspace. Carbon dioxide in the microcosms was also measured to determine if TBM reduction is mainly due to mineralization. Treatments, controls and carbon dioxide controls were set up for the study. Treatments contained TBM, water and soil as mentioned above; controls contained sterilized soil, TBM, and water; carbon dioxide controls contained soil and water. No TBM was added to the carbon dioxide controls. The treatments were set up for a 62-day period. Gas chromatography was used to measure TBM and carbon dioxide concentration in the headspace. It was seen that TBM concentration decreased to a greater extent in the treatments compared to the controls. Also there was more carbon dioxide in the treatments than in the sterilized soil. These results are indicative of biodegradation of TBM. Further, a di-*tert*-butyl disulfide peak was present in the TBM chromatogram. From reviewing TBM chemistry, it appears that di-*tert*-butyl disulfide may be an intermediate product of biodegradation. It was found that in general more di-*tert*-butyl disulfide was formed in the case of treatments than the sterilized controls. This is another fact that supports biodegradation of TBM. The results of this study showed significant biodegradation of TBM in a soil-water system.

Introduction

A review of the published literature was made to determine the biodegradation characteristics of tertiary butyl mercaptan (TBM). As no experimental studies were found, a biodegradation study was conducted following the methods that have been used in other studies (Knox et al., 1993; Eweis et al., 1998; Cookson, 1995).

Experimental

Treatments–Treatments were set up to monitor the reduction of *tert*-butyl mercaptan (TBM) in soil water system due to biodegradation. The treatments consist of 160-mL serum bottles sealed with a Teflon-lined septum, containing 10 g Fort Riley agricultural soil and 10 mL water. After the bottle was closed with the septum and crimped, 10 µL TBM was injected through the septum. The treatments were set up on "Day 0" on Sep 22, 2003. Three replicates of each treatment were set up for days 1, 4, 6, 8, 12, 16, 20, 26 and 33. Treatments set up for day 1 were sampled on days 0, 1, and 49. The remaining sets of bottles were sampled only once on one of the days mentioned above.

Controls–Controls help to establish the fact that reduction in TBM is due to biodegradation. In the absence of microorganisms there should be no significant reduction in the level of TBM. The

controls consist of the same Fort Riley agricultural soil as treatments, but in this case it was sterilized. Sterilization of soil was done as follows: the required amount of soil was packed in an aluminum foil and placed in an autoclave at 250 °F for 50 min. The soil packed in the aluminum foil was allowed to cool. It was then incubated at 30°C for 2 h. Then the soil was again autoclaved as before. This process was repeated three times to ensure maximum destruction of microorganisms. Sterilized serum bottles were used for these controls and any instrument used for setting up the controls such as spatula, pipettes, beakers etc., were also sterilized. The controls were set up using 10 g sterilized soil (sterilized as mentioned above), 10 mL deionized water, and a 10-μL TBM in 160 mL serum bottle. The deionized water was not sterilized before adding to the controls. Controls were setup and sampled on the same days as treatments.

CO_2 Controls–The carbon dioxide controls were set up to see the extent of microbial activity in the absence of TBM. They help to identify if TBM helps to increase or decrease microbial activity. The controls consist of 10 g Fort Riley agricultural soil and 10 mL water in 160-mL serum bottle. No TBM was added to these CO_2 controls, which were set up for analysis on days 4, 12, 26, and 62.

Analytical Methods–TBM was analyzed using a Hewlett Packard 5890 Series II gas chromatograph with a flame ionization detector. An HP1 megabore column of of 30 m length, 0.53 mm internal diameter, and 5 μm film thickness was used. TBM was analyzed by injecting 10 μL of headspace gas from the serum bottle manually using a gas-tight Hamilton syringe. The chromatogram obtained showed a TBM peak appearing at about 2 min and a disulfide peak around 12 min. The peak areas were obtained through automatic integration.

CO_2 was measured using a Shimadzu gas chromatograph with a thermal conductivity detector. A sample containing 0.5 mL of gas phase was injected and the carbon dioxide peak appeared around 0.6 min. The peak area was calculated automatically.

Results and Discussion

The concentration of TBM in the treatments decreased more rapidly than that in the controls. Figure 1 shows the behavior of TBM during a 62-day period for the controls and treatments. It may be seen that TBM reduction in the treatments is much higher than the controls, which had sterilized soil. This demonstrates that TBM reduction is taking place due to biodegradation. The controls have sterilized soil and hence ideally there should be no reduction in TBM in the control. But the graph shows that some reduction did occur. This may be due to the fact that the contents might not have been sterilized completely. There might have some form of bacterial contamination that led to the reduction in TBM in the controls. Nevertheless, reduction of TBM is more in the case of treatments than in the controls. There was no evidence of a lag period for the biodegradation of TBM in the unsterilized soil. For these treatments more than 99% of the TBM disappeared during the first 33 days of the experiment.

The production of CO_2 in the controls and treatments also provide evidence in favor of biodegradation of TBM. Figure 2 shows carbon dioxide production in treatments, controls and carbon dioxide controls from day 0 to day 62.

Figure 2 shows that there is significantly more carbon dioxide produced in the treatments than in the sterilized controls. It appears that treatments have more microorganisms and were more effective in reducing TBM and producing CO_2 than the controls, which were sterilized.

Another observation that further supports biodegradation of TBM is disulfide production in

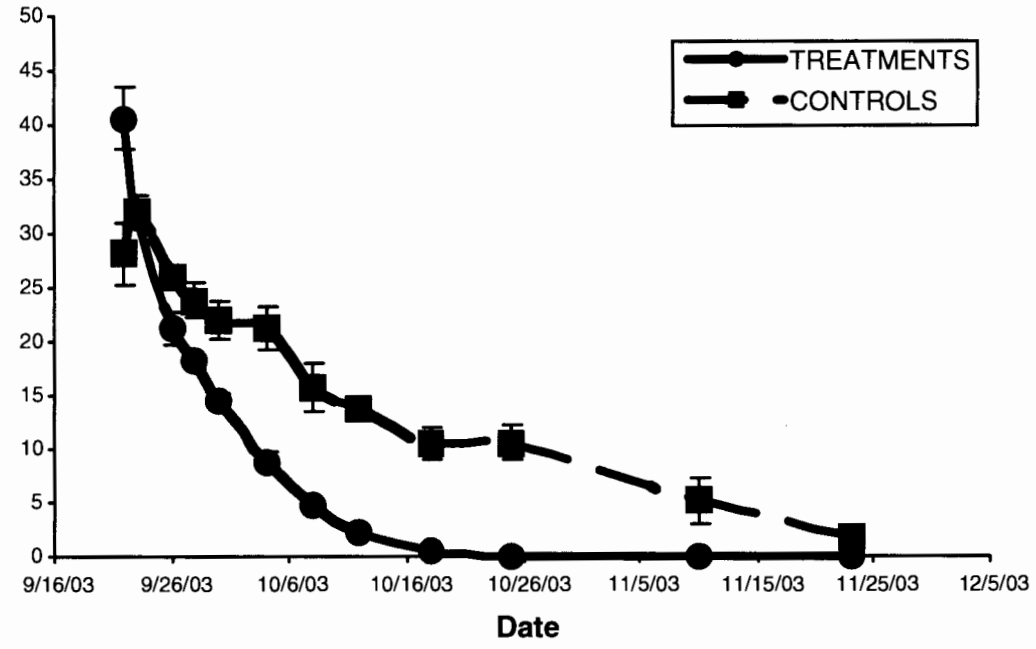

Figure 1. Gas-phase concentration in the headspace for the treatments and the controls.

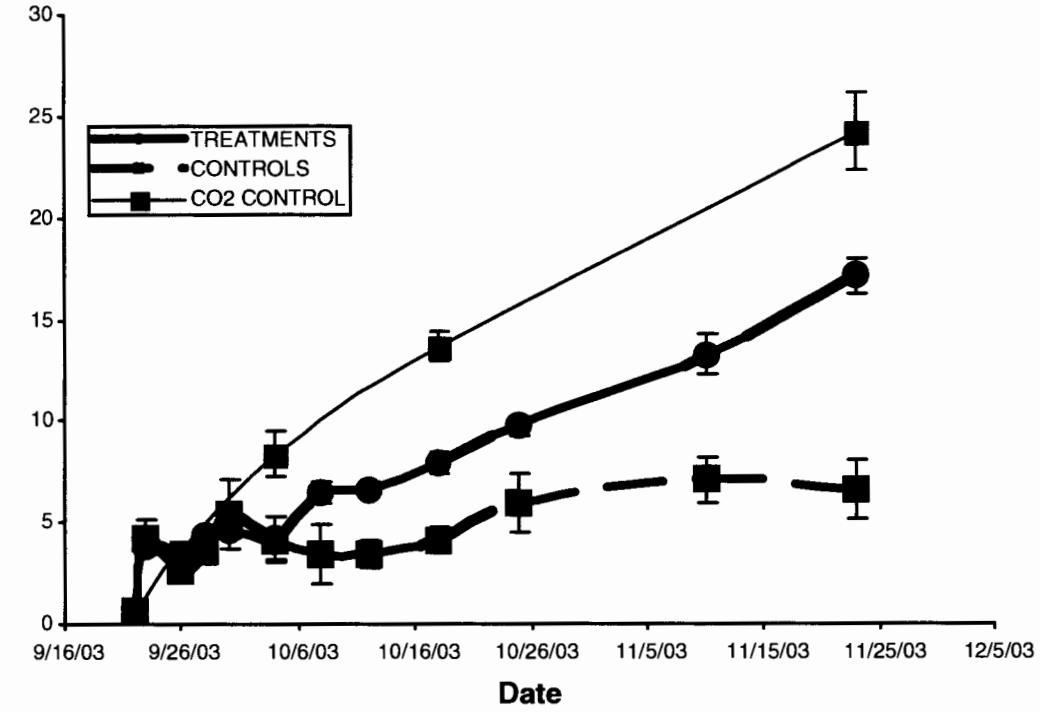

Figure 2. Gas-phase concentrations of CO_2 in the head space of the treatments, controls (sterilized soil), and CO_2 controls (controls without TBM).

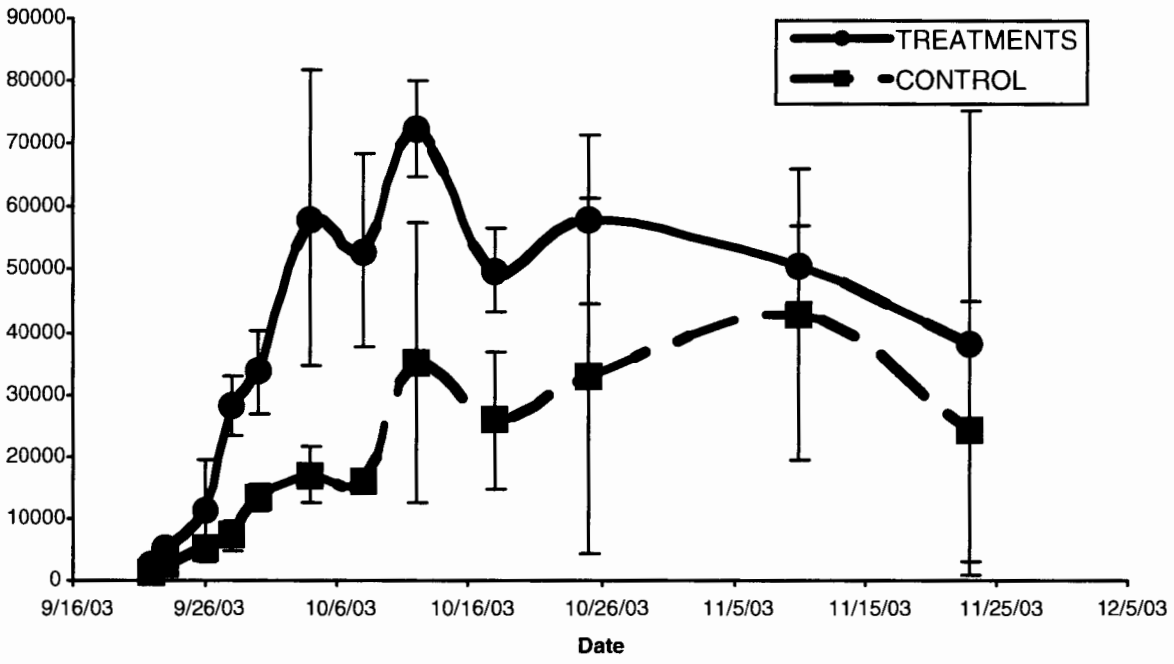

Figure 3. Gas-phase concentration of di*tert*-butyl disulfide produced from TBM for the treatments and the controls.

the treatments and controls (Figure 3). It may be seen that there is more disulfide production in the treatments than in the sterilized controls.

For the treatments the highest disulfide concentration occurs when the TBM concentration in Figure 1 is about 2 μg/mL. During the last 30 days of the study disulfide concentration decreased and CO_2 concentration increased. This indicates there is some disulfide biodegradation.

It was seen earlier by testing that the Teflon lined-septum could withstand multiple punctures with negligible leakage. Also, the treatments, sterilized controls, and CO_2 controls were placed in dark locations away from any light. Hence the reduction in TBM due to photodegradation or leakage is negligible. Since there is greater reduction of TBM in the treatments than in the sterilized controls, we have evidence that the TBM is being biodegraded by the bacterial population in the agricultural soil.

Error Bars–Three replicates (each from a different microcosm set up at the same time) were made for each set of treatment, control, and CO_2 control sampled on a particular day. The average values of the three replicates are plotted in Figures 1–3. The error bars show the standard deviation of the replicate values in the positive and negative direction from the average value.

TBM Chemistry–tert-Butyl mercaptan is one of the materials added to natural gas to produce the characteristic odor that signals a gas leak. It is called a thiol or mercaptan as it incorporates a C-S-H functional group. The IUPAC name for tertiary butyl mercaptan is 2-methyl-2-propanethiol. Mercaptans on prolonged exposure to air oxidize to their corresponding disulfides. Primary mercaptans oxidize more readily than secondary mercaptans, and tertiary mercaptans oxidize least readily. Tertiary butyl mercaptan oxidizes to di-*tert*-butyl disulfide by the following reaction:

$$2(CH_3)_3CSH + 1/2O_2 \rightarrow (CH_3)_3CSSC(CH_3)_3 + H_2O$$

Conclusions

tert-Butyl mercaptan disappeared in approximately one month in soil microcosms. Two biodegradation products, carbon dioxide and di-*tert*-butyl disulfide, were measured in the headspace gas.

Acknowledgment

This work was partially supported by the Department of Navy, Naval Surface Warfare Center, Dahlgren Laboratory. The content of the information does not reflect the position or policy of the government, and no official endorsement should be inferred.

References

Cookson, J. T., *Bioremediation Engineering*, McGraw-Hill, New York (1995).

Eweis, J. B., S. J. Ergas., D. P. Y. Chang and E. D. Schroeder., *Bioremediation Principles,* WCB/McGraw-Hill, New York (1998).

Knox, R. C., D. A. Sabatini and L. W. Canter., *Subsurface Transport and Fate Process*, Lewis Publishers, Florida (1993).

Probing the Substrate Specificity of *Streptomyces* Phospholipase D by Automated Docking

Patrick D. McMullen, Christopher L. Aikens, and Peter J. Reilly
Department of Chemical Engineering, Iowa State University, Ames, IA 50011

Abstract

Alkylphosphocholines, alkylcarboxycholines, dialkylphosphates, and phospholipids with nonnatural head groups, the first three with varying alkyl chain lengths, were computationally docked by AutoDock into the active site of *Streptomyces* sp. PMF phospholipase D. This work supplements earlier dockings of naturally occurring phospholipids. Ligands were more easily docked and have progressively more negative binding energies as chain length increases. Binding energies of ligand of the same chain length decrease in the order alkylcarboxycholines > alkylphosphocholines > dialkylphosphates (which have two chains rather than one) > phospholipids (which have in addition a glycerol moiety and a head group). Although dialkylphosphates can be docked, they are not hydrolyzed by phospholipase D. Relative hydrolysis rates of phospholipids are roughly predicted by binding energies and by octanol-water partition coefficients of their head-group alcohols. Further studies will establish whether more recent enzyme crystal structures will yield similar docking results.

Introduction

Phospholipase D (E.C. 3.1.4.4, phosphatidylcholine phosphatidohydrolase, PLD) catalyzes reactions that are important in membrane construction, signaling, and transport. The natural substrates of this enzyme are phosphatidyl esters, most commonly phospholipids (PLs), which are comprised of a glycerol moiety with fatty acid chains attached at the *sn*-1 and *sn*-2 positions and a polar head group attached at the *sn*-3 position via a phosphodiester linkage. PLD hydrolyzes the bond between the phosphorus atom and the head group (Fig. 1). Transesterification reactions also occur in the presence of alcoholic nucleophiles.

PLD has two HKD (histidine-lysine-aspartic acid) motifs containing catalytic histidine residues.[1,2] The reaction occurs via a ping-pong mechanism with an enzyme-substrate covalent intermediate.[3] One histidine residue catalyzes nucleophilic attack upon the substrate phosphorus atom, forming the intermediate as the head group is protonated by the other histidine residue. The intermediate undergoes either hydrolysis, yielding a phosphatic acid, or alcoholysis, yielding another PL (Fig. 1).[4–7]

PLD-catalyzed reactions take place *in vivo* at the membrane bilayer.[8] Experimentally, the reaction is commonly performed in a two-phase emulsion system. It can occur either at the organic-aqueous boundary or in reverse micelles, occurring in the organic phase.[9]

Structural data obtained from the crystallization of *Streptomyces* sp. PMF PLD with an inorganic phosphate ion support the proposed mechanism.[10] Although these data located the cleavage site and confirmed the role of the HKD motif, they provided little knowledge about any enzyme-substrate interactions beyond those involving the phosphate group. New crystallographic data describe the enzyme in a number of complexed forms, including PLD with bound dibutyrylphosphatidic acid.[11] This form contains one catalytic histidine residue in a position to coordinate with the phosphate group of the substrate. The same residue in the phosphate-bound crystal is bent in a manner that inhibits catalytic activity.

The activity of *Streptomyces* PLD ranges beyond hydrolysis of natural PLs, as it can trans-

phosphatidylate them to many products.[12] Furthermore, it hydrolyzes a number of nonnatural PLs (PLs with head groups not commonly found *in vivo*), as well as alkylphosphocholines (APCs) and alkylcarboxycholines (ACCs), but not dialkylphosphates (DAPs), suggesting that substrate recognition may be a function of alkyl chain interactions as well as those with glycerol, phosphate, and head groups.[13]

Computation has provided further insight into the PLD catalytic mechanism. Naturally occurring PLs (phosphatidylcholine, phosphatidylethanolamine, phosphatidylglycerol, phosphatidylinositol, phosphatidylserine, and their cleavage product, phosphatidic acid) were subjected to computational docking into the *Streptomyces* sp. PMF PLD active site using AutoDock (Scripps Research Institute, La Jolla, CA).[14] PLs dock in predictable patterns, similar across the substrates tested.[15] Head groups reside in a small pocket near the catalytic histidine residues and the alkyl chains dock along one of three negative or hydrophobic surfaces. Substrate docking is affected substantially by the length of the alkyl chain and the identity of the head group, likely due to favorable hydrophobic interactions between the alkyl chains and hydrophobic residues in the active site.

We have used AutoDock to probe the binding and catalytic mechanisms of a number of proteins, such as glucoamylase,[16] α-amylase,[17] mannose binding protein C,[18] and α-1,2-mannosidase,[19] in addition to the work previously done with PLD.

This project extends previous computational work with PLD by using AutoDock to dock members of the four classes of substrates mentioned above into the PLD active site. It is hoped that the information gained from this project, in conjunction with existing crystallographic and kinetic data, will help to further elucidate the mechanism of PLD.

Methods

AutoDock Suite 3.06[14] was used to computationally dock APCs of chain length n = 4, 6, 8, 12, 14, and 16, ACCs of n = 4, 6, 8, 10, 12, 14, and 16, DAPs with two equal-length chains of n = 6, 8, 10, and 12, and PLs with various nonnatural head groups of n = 8 (Fig. 2) into the crystal structure of *Streptomyces* sp. PMF PLD (Protein Data Bank code 1F0I). The enzyme was previously prepared[15] by adding hydrogen atoms to the crystal-structure heavy atoms and by adding partial charges by the Amber_95 all-atom partial charge scheme.[20] Grid energies were established previously.[15] PCModel (Serena Software, Bloomington, Ind.) was used to generate the ligand molecules, and GAMESS was used to calculate their partial charges.[21] Parameters for these programs were more completely described by Aikens *et al.*[15]

Each docking simulation began by placing the ligand roughly in the active site by superimposing its phosphate group or corresponding ACC carboxyl group over the crystal-structure phosphate group. AutoDock uses a Lamarkian genetic algorithm (LGA) to search for a substrate position, yielding an energy minimum. One hundred such minima were collected from the initial docking attempt, and the best of these (those with phosphorus atoms or ACC carboxyl carbon atoms closest to the crystal-structure phosphorus atom), were used as starting positions for following attempts. The dockings were repeated until either the ligand was successfully docked or until ten successive attempts resulted in failure. The structure was considered docked if it possessed the lowest energy in the simulation and if its phosphorus atom or ACC carboxyl carbon atom was 1.0 Å or less from the crystal-structure phosphorus atom.

Octanol-water partition coefficients (K_{ow}) of the alcohol head groups were used to estimate the relative distribution of the substrates across the organic-aqueous phase boundary. For many of these alcohols, suitable experimental information could not be found, and their partition co-

efficients were estimated by a fragment constant method.[22] This method is based on the assumption that partition coefficients are the result of the sum of contributions of individual chemical groups. In some instances, interactions between these groups also contribute factors to the coefficient. When appropriate, structural analogues of the alcohols were used as starting points for group calculations. This method is supported well by experimentally derived properties.[23] In four cases these estimates were compared with experimental values of head-group alcohols, yielding K_{ow} values of 1.70 and 1.51 for 1,2-cyclohexane, 0.49 and 0.468 for ethanol, 0.0027 and 0.0144 for glycerol, and 17.8 and 19.5 for 2-pentanol, experimental values preceding estimated values. The fragment constant method behaves poorly with polyhydroxyl compounds such as glycerol.[23] Experimental values, when available, were used instead of estimated values.

Results

The APCs are examples of non-PL substrates hydrolyzed at significant rates by PLD. Ligands of n = 4, 6, 8, 12, 14, and 16 all docked with relative ease. In every instance, the aliphatic tail curled along the same negatively-charged pocket and the choline head group fit in the same pocket (Fig. 3) as did the tail and head group in prior studies of phosphatidylcholines.[15] Also, similar to previous findings, docking energy was negatively correlated with n (Table I).

ACCs vary from APCs only in having a carboxyl group rather than a phosphate group. ACCs of n = 4, 6, 8, and 10 could not be docked, while those of n = 12, 14, and 16 were successfully docked. Head groups and hydrophobic tails each were bound in positions analogous to those of APCs for $n \leq 14$, but at n = 16 the tail was bound along a hydrophobic surface (Fig. 4) as is common with long-chain PLs.[15] Binding energies become more negative with increasing n, but are less than those of APCs of the same n (Table I).

DAPs, with a phosphate group like APCs, but having a second alkyl chain rather than a head group, docked with one chain curled along the negatively-charged pocket, while the other at sufficiently high values of n started to curl up out of the head-group space and onto a negatively-charged surface (Fig. 5). DAPs exhibit more negative energies at the same values of n than do APCs and ACCs, but much less than all PLs that were docked (Tables I and II).

PLs with nonnatural head groups docked in the PLD active site where other ligand classes had docked, with its head groups docked where choline usually is located and with its chains lying in the negatively-charged pocket (Fig. 6). Only the PL with the 4-penten-1-ol head group deviated from this behavior, in having its long head group docked in the negatively-charged pocket with its fatty acid chains. Several of the head groups (1,2-cyclohexanediol, 2,2-dimethyl-1,3-dioxolane-4-methanol, glycerol, and 2-pentanol) have chiral centers when freestanding or only when part of PLs, and all forms were subjected to docking. Only one stereoisomer of each ligand, specifically those containing (1*S*,2*R*)-1,2-cyclohexanediol, (*R*)-2,2-dimethyl-1,3-dioxolane-4-methanol, (*R*)-glycerol, and (*R*)-2-pentanol, was successfully docked.

Discussion

This study provided a unique opportunity to compare hydrolysis data for various PLD substrates to automated docking results. A number of factors pertaining to automated docking can be considered: binding energy, nearness to the crystal-structure phosphorus atom, and number of simulations required for docking.

As we found previously[15] and as is shown here (Table I), substrates of higher n yield more negative binding energies, due to additional interactions between PLD and the hydrophobic tails of the ligands. In addition, binding energies at constant n decrease in the order ACCs > APCs >

DAPs > PLs. We can conclude from this that the phosphate groups in APCs, having two more oxygen atoms and a negative charge, are bound more firmly than the carboxyl groups in ACCs. Furthermore, the more negative binding energies of DAPs than APCs are likely due to the additional interactions with residues on the enzyme surface of the second alkyl chain of DAPs, specifically at longer lengths such as $n = 12$, compared to the smaller choline head group of APCs. In turn, PLs have more negative binding energies than DAPs of the same n because their two chains and glycerol, phosphate, and choline groups are bound more tightly than the two chains and phosphate group of DAPs (Tables I and II). Finally, phosphatidylcholine has a more negative binding energy than PLs with other head groups but of the same n because its choline head group is bound more tightly than any of the other head groups (Table II).

We hypothesized that binding energies could be good predictors of hydrolysis rates. A more negative binding energy could imply a more negative Gibbs free energy, which is directly related to the rate of hydrolysis. The relationship proves to be more complicated than this, as binding energies correspond only roughly with observed rate data (Tables I and II).[15]

In a two-phase enzymatic system such as the one employed in PLD experimentation, it is important to consider the phase characteristics of the substrate. The reaction, which can occur at a considerable rate at the organic-aqueous interface, requires that substantial concentrations of the substrate be present there. Natural PLs (characterized by a polar head and a hydrophobic tail region) are present at such an interface. If the head group is significantly hydrophobic, the substrate may exist almost entirely in the organic phase. To demonstrate this, partition coefficients of head-group alcohols of nonnatural PLs are correlated with relative rates in Fig. 7. There is a general negative relationship between the two, a confirmation that hydrolysis rates decrease with increasing head-group hydrophobicity, as previously found experimentally.[13]

Binding energies do not reflect this phase problem, and within it lays a possible explanation for the lack of activity of DAPs, not only the one of $n = 8$ but also all others of unspecified n that were tested.[13] These substrates, which are quite nonpolar, are likely almost nonexistent at the interface, certainly at high values of n.

Failure to dock a number of PL stereoisomers suggests a form of selectivity that was unexpected. PLD transphosphatidylates phosphatidylcholine in the presence of a number of racemic alcohols without bias.[24] This finding indicates that some of the ligands that did not dock may be active substrates of PLD. In fact Bossi *et al.*[13] may have used PLs with 1,2-cyclohexanediol, glycerol, and 2-pentanol head groups of mixed stereoisomerism in their hydrolysis experiments, leading to the possibility that the rates they measured might be from two or more distinct substrates. The presence of false negatives is likely a result of the random nature of the LGA search mechanism, and can probably be resolved through more computationally time-intensive procedures (i.e. more generations, larger populations, larger crossover rates).[14]

In addition to the proximity of the substrate phosphorus (or carboxyl carbon) atom to the crystal-structure phosphorus atom, the position of the substrates relative to each other is also of interest. Since proximity of the substrate to the crystal-structure phosphorus atom was a condition for docking, this information is less important than binding energies. However, some interesting trends among the four groups emerged. The APCs docked with phosphorus atoms an average of 0.62 Å from the crystal-structure phosphorus atom, but only 0.28 Å from the mean position of that atom in all docked APCs. The other substrates demonstrated similar behavior: ACCs, DAPs, and nonnatural head-group PLs docked a mean distance of 0.71 Å, 0.35 Å, and 0.60 Å, respectively, from the crystal-structure phosphorus atom but with distances of 0.41 Å, 0.28 Å, and 0.23 Å from their respective mean phosphorus atom positions. The average distance

from the crystal-structure phosphorus atom for all substrates was 0.59 Å, with a distance of 0.34 Å from their mean positions in the docked substrates. This indicates docking homology within and across the four classes considered.

The most qualitative of the evaluation criteria is the ease at which docking occurred. We hypothesized that those ligands bound strongly by PLD would exhibit more negative binding energies, which are more easily isolated by the LGA from other local minima. This corresponds to a lower number of simulations required to solve the energy equation. However, the number of simulations required could not be correlated well with either experimental kinetics or computationally derived binding energies.

It has been recently discovered that the conformation of the PLD active site in the presence of a PL substrate is different than that in the presence of the phosphate ion.[11] The phosphate ion, a PLD inhibitor, causes one HKD histidine residue to fold away from the scissile bond, impeding catalysis. At the time these simulations were run, only PLD-phosphate crystallography data were available. The difference in active-site topography between the phosphate-bound crystal structure and the more recent crystal structures with dibutyrylphosphatidic acid and other ligands bound in the active site could be a source of error in this study.

The LGA employed by AutoDock is subject to a number of limitations typical of computational systems. Solving the energy equation must be a compromise between computational time and system complexity. AutoDock handles this issue by treating the enzyme as a rigid body and allowing the ligand to find its lowest-energy conformation, intramolecular as well as intermolecular, in the active site. This is likely the source of some error in the docking computations.

It is hoped that this use of computation in an attempt to explain experimental data will further the understanding of the action of PLD with a wide range of substrates.

Acknowledgments

The authors are grateful for the advice of Anthony Hill in general computational techniques, and for the financial assistance of the U.S. Department of Agriculture through the Biotechnology Byproducts Consortium.

References

1. Hammond SM, Altshuller YM, Sung T-C, Rudge SA, Rose K, Engebrecht J, Morris AJ, Frohman MA. Human ADP-ribosylation factor-activated phosphatidylcholine-specific phospholipase D defines a new and highly conserved gene family. J Biol Chem 1995;270:29640–29643.
2. Ponting CP, Kerr ID. A novel family of phospholipase D homologues that includes phospholipid synthases and putative endonucleases. Identification of duplicated repeats and potential active site residues. Protein Sci 1996;5:914–922.
3. Stanacev NZ, Stuhne-Sekalec L. On the mechanism of enzymatic phosphatidylation: Biosynthesis of cardiolipin catalyzed by phospholipase D. Biochim Biophys Acta 1970;210:350–352.
4. Gottlin EB, Rudolph AE, Zhao Y, Matthews HR, Dixon JE. Catalytic mechanism of the phospholipase D superfamily proceeds via a covalent phosphohistidine intermediate. Proc Nat Acad Sci USA 1998;95:9202–9207.
5. Rudolph AE, Stuckey JA, Zhao Y, Matthews HR, Patton WA, Moss J, Dixon JE. Expression, characterization, and mutagenesis of the *Yersinia pestis* murine toxin, a phospholipase D superfamily member. J. Biol Chem 1999;274:11824–11831.
6. Waite M. The PLD superfamily: Insights into catalysis. Biochim Biophys Acta 1999;1439:187–197.

7. Yang H, Roberts MF. Phosphohydrolase and transphosphatidylation reactions of two *Streptomyces* phospholipase D enzymes: Covalent versus noncovalent catalysis. Protein Sci 2003;12:2087–2098.
8. Estrela-Lopis I, Brezesinski G, Mohwald H. Influence of model membrane structure on phospholipase D activity. Phys Chem Chem Phys 2000;20:4600–4604.
9. Hirche F, Ulbrich-Hofmann R. The interfacial pressure is an important parameter for the rate of phospholipase D catalyzed reactions in emulsion systems. Biochim Biophys Acta 1999;1436:383–389.
10. Leiros I, Secundo F, Zambonelli C, Servi S, Hough E. The first crystal structure of a phospholipase D. Structure 2000;8:655–667.
11. Leiros I, McSweeney S, Hough E. The reaction mechanism of phospholipase D from *Streptomyces* sp. strain PMF. Snapshots along the reaction pathway reveal a pentacoordinate reaction intermediate and an unexpected final product. J Mol Biol 2004;339:805–820.
12. D'Arrigo P, de Ferra L, Piergianni V, Selva A, Servi S, Strini A. Preparative transformation of natural phospholipids catalysed by phospholipase D from *Streptomyces*. J Chem Soc Perkin Trans 1 1996;2651–2656.
13. Bossi L, D'Arrigo P, Pedrocchi-Fantoni G, Mele A, Servi S, Leiros I. The substrate requirements of phospholipase D. J Mol Catal B 2001;11:433–438.
14. Morris GM, Goodsell DS, Halliday RS, Huey R, Hart WE, Belew RK, Olson AJ. Automated docking using a Lamarckian genetic algorithm and an empirical binding free energy function. J Comput Chem 1998;19:1639–1662.
15. Aikens CL, Laederach A, Reilly PJ. Visualizing complexes of phospholipids with *Streptomyces* phospholipase D by automated docking. Proteins, in press.
16. Coutinho PM, Dowd MK, Reilly PJ. Automated docking of monosaccharide substrates and analogues and methyl α-acarviosinide in the glucoamylase active site. Proteins 1997;27:235–248.
17. Rockey WM, Laederach A, Reilly PJ. Automated docking of α-1,4- and α-1,6-linked glucosyl trisaccharides and maltopentaose into the soybean β-amylase active site. Proteins 2000;40:299–309.
18. Allen MJ, Laederach A, Reilly PJ, Mason RJ. Polysaccharide recognition by surfactant protein D: Novel interactions of a C-type lectin with nonterminal glucosyl residues. Biochemistry 2001;40:7789–7798.
19. Mulakala C, Reilly PJ. Understanding protein structure-function relationships in Family 47 α-1,2-mannosidases through computational docking of ligands. Proteins 2002;49:125–134.
20. Cornell WD, Cieplak P, Bayly CI, Gould IR, Merz KM Jr., Ferguson DM, Spellmeyer DC, Fox T, Caldwell JW, Kollman PA. A second generation force field for the simulation of proteins, nucleic acids, and organic molecules. J Am Chem Soc 1995;117:5179–5197.
21. Schmidt MW, Baldridge KK, Boatz JA, Elbert ST, Gordon MS, Jensen JH, Koseki S, Matsunaga N, Nguyen KA, Su SJ, Windus TL, Dupuis M, Montgomery JA Jr. The general atomic and molecular electronic structure system. *J Comp Chem* 1993;14:1347–1363.
22. Hansch C, Leo A. Substituent Constants for Correlation Analysis in Chemistry and Biology. New York: Wiley; 1979. 339 pp.
23. Lyman W, Reehl W, Rosenblatt D. Handbook of Chemical Property Estimation Methods: Environmental Behavior of Organic Compounds. New York: McGraw-Hill; 1982.
24. D'Arrigo P, de Ferra L, Pedrocchi-Fantoni G, Scarcelli D, Servi S, Strini A. Enzyme-mediated synthesis of two diastereoisomeric forms of diphosphatidylglycerol (cardiolipin).

J Chem Soc Perkin Trans 1 1996;2657–2660.

TABLE I. Binding Energies, Phosphorus-Atom Distances[a] (Å), and Relative Hydrolysis Rates[b] of non-PL Ligands

n	APC		ACC		DAP	
	Binding energy (kcal/mol)	Rel. rate	Binding energy (kcal/mol)	Rel. rate	Binding energy (kcal/mol)	Rel. rate
4	–114.72 (0.53)	0.2	DND[c]	0.06	—	—
6	–129.97 (0.60)	0.4	DND	—	DND	—
8	–143.65 (0.66)	0.8	DND	—	–153.76 (0.38)	0.0
10	—	—	DND	—	–176.92 (0.40)	0.0
12	–159.44 (0.37)	—	–153.44 (0.66)	0.75	–192.72 (0.28)	0.0
14	–174.22 (0.86)	—	–167.53 (0.86)	—	—	—
16	–197.99 (0.72)	—	–174.93 (0.61)	—	—	—

[a]In parentheses.
[b]Data of Bossi *et al.*[13] based on phosphatidylcholine = 1.
[c]Did not dock.

TABLE II. Binding Energies, Phosphorus-Atom Distances[a] (Å), and Relative Hydrolysis Rates[b] of PLs of $n = 8$ with Various Head Groups

Head group	Binding energy (kcal/mol)	Relative rate
3-Butyn-1-ol	–196.67 (0.80)	0.1
Choline	–224.66 (0.33)	1
(1*S*,2*R*)-1,2-Cyclohexanediol	–199.83 (0.62)	0.09
1,3-Dihydroxy-2-propanone	DND[c]	0.7
(*R*)-2,2-Dimethyl-1,3-dioxolane-4-methanol[d]	–180.54 (0.77)	0.04
(*R*)-2,2-Dimethyl-1,3-dioxolane-4-methanol	DND	0.4
Ethanol	–189.28 (0.96)	0.04
(*R*)-Glycerol	–210.97 (1.19)	0.3
(*R*)-2-Pentanol	–203.07 (0.55)	0.03
4-Penten-1-ol	–200.43 (0.43)	0.03

[a]In parentheses.
[b]Data of Bossi *et al.*[13] based on phosphatidylcholine = 1.
[c]Did not dock.
[d]$n = 6$.

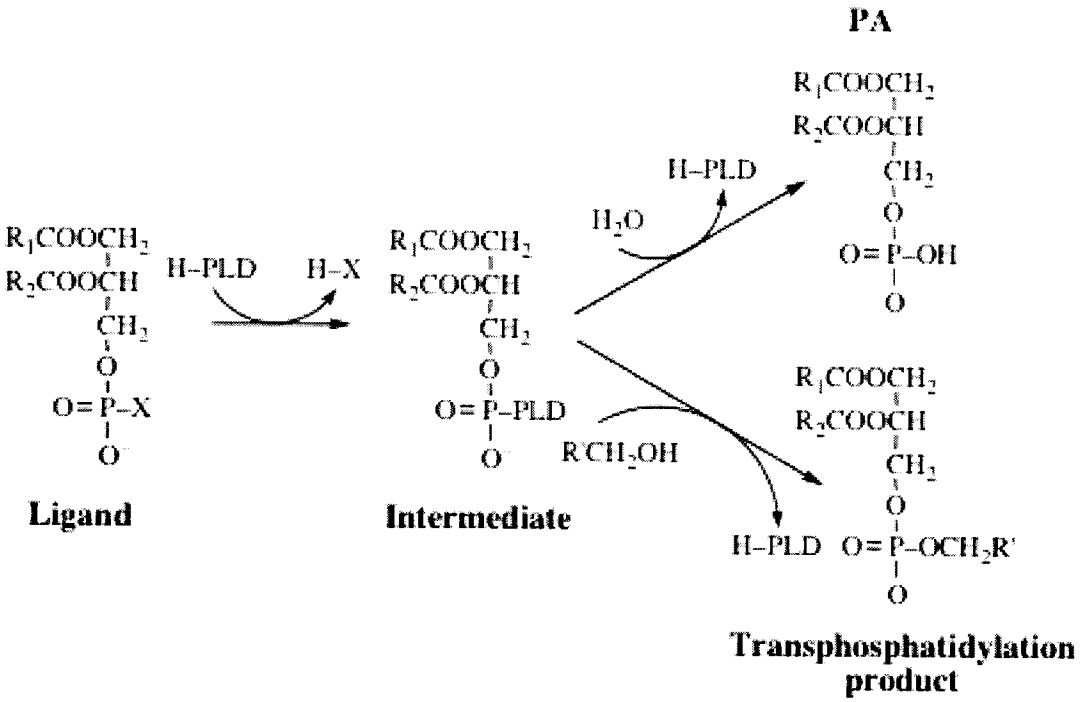

Fig. 1. Reactions catalyzed by PLD.

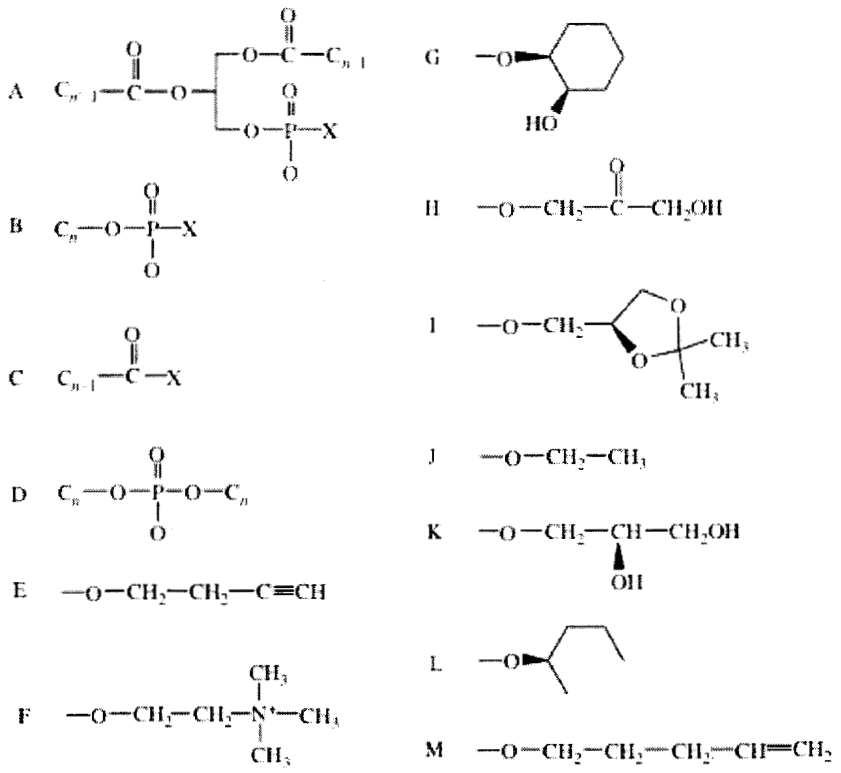

Fig. 2. Substrate structures. A) Phospholipid; B) alkylphospho moiety; C) alkylcarboxyl moiety; D) dialkylphosphate. Head groups (X): E) 3-butyn-1-ol; F) choline; G) (1*S*,2*R*)-1,2-cyclohexanediol; H) 1,3-dihydroxy-2-propanone; I) *R*-2,2-dimethyl-1,3-dioxolane-4-methanol; J) ethanol; K) *R*-glycerol, L) *R*-2-pentanol; M) 4-penten-1-ol. *n* = number of carbon atoms in chain.

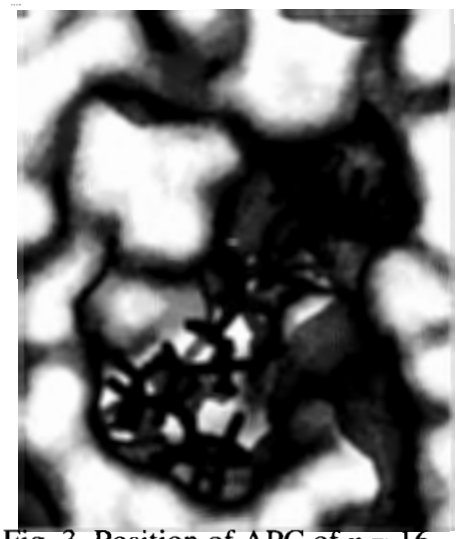

Fig. 3. Position of APC of *n* = 16 (hexadecylphosphocholine) in the PLD active site.

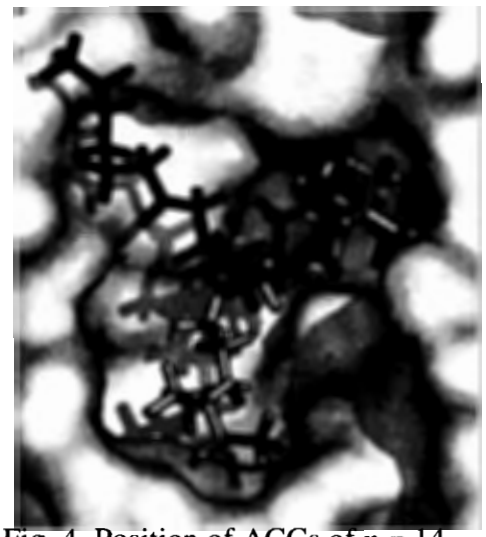

Fig. 4. Position of ACCs of *n* = 14 (tetradecylcarboxycholine, gray) and *n* = 16 (hexadecylcarboxycholine, black) in the PLD active site.

Fig. 5. Position of DAP of $n = 12$ (didodecyl phosphate) in the PLD active site.

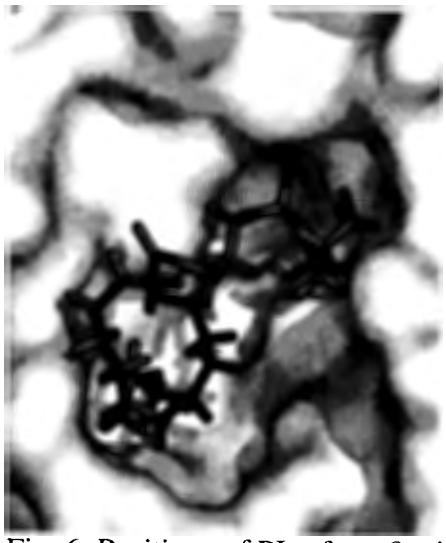

Fig. 6. Positions of PL of $n = 8$ with a (*R*)-2-pentanol head group (1,2-dioctanoyl-*sn*-glycero-3- phospho-(*R*)- 2-pentanol) in the PLD active site.

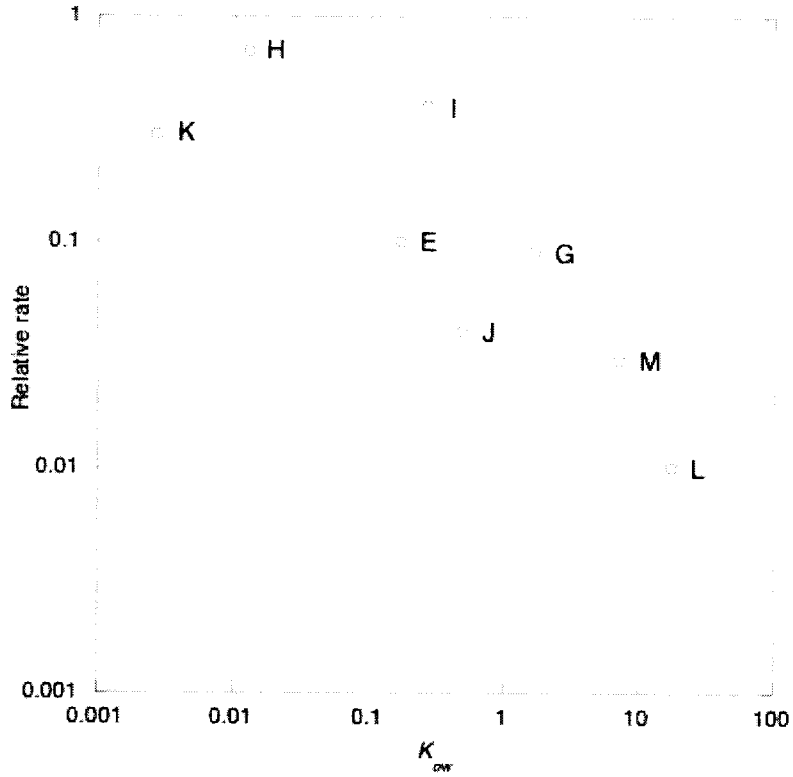

Fig. 7. Relative hydrolysis rates as a function of octanol-water partition coefficients of head-group alcohols. Identities as in Fig. 2.

On-Line Predictive Model for Cell Mass in *Pichia pastoris* Fermentation Using Neural Networks

Sreenivasula Ramireddy and Michael M. Meagher
Department of Chemical Engineering, University of Nebraska–Lincoln, Lincoln, NE 68588

Introduction

The success of control strategies to optimize protein production during the induction, the critical phase in *Pichia pastoris* fermentation, relies mainly on how accurately the cell mass in the fermentation vessel is predicted or measured. An on-line neural network model to predict cell growth based on the response variables – methanol consumption rate (MCR), CO_2 evolution rate (CER), and oxygen consumption rate (OCR) – is expected to capture the intrinsic relationship between the cell growth and other fermentation state variables such as pH, temperature, and strain type, which are either controlled or nearly fixed during a single fermentation run. The model under development will work as a soft sensor for cell mass since the response variables can be dynamically collected and processed through the neural network in real time. However analyzing the relationships between the state variables and the response variables; the cell mass and the response variables; and finally cell mass and protein production becomes the essential part of this research for two reasons. One, the soft sensor is based on the relationship between response variables and cell mass. Two, optimal protein production is the ultimate goal of a fermentation run rather than cell mass. The most useful immediate application for a successful soft sensor for cell mass is to develop a pseudo-feed forward feedback controller for feeding the inducer by allowing the calculation of the dynamic specific growth rate.

Recombinant protein production using *Pichia pastoris* as expression system

The methylotropic yeast *Pichia pastoris* has been widely used to express heterologous proteins because of its competitive features over other organisms. Some of its outstanding features include high cell density expression[11,23,24], strong and tightly controlled methanol-induced alcohol oxidase promoter (AOX)[25], absence of endotoxins, which allows the recombinant proteins to be used therapeutically[10], and the commercial availability of the *Pichia* expression system (Invitrogen Corporation, Carlsbad, CA). The AOX promoter responsible for protein induction is repressed in the presence of an excess amount of non C_1- substrates such as glycerol[6,23,26]. However, cell growth is very high in the presence of glycerol. Thus initially cells are grown on glycerol and after reaching the desired cell density, the substrate is changed to methanol. AOX is derepressed in the presence of methanol. Including a transition phase between glycerol and methanol growth stages not only reduces the adaptation time but also increases protein expression. Thus a typical *Pichia* fermentation involves four different phases, a glycerol batch phase, a glycerol-fed batch phase, a transition phase, and a methanol induction phase. Feeding glycerol at a constant rate during fed-batch operation allows the consumption of the toxic intermediates such as ethanol and hydrogen peroxide formed during the glycerol batch phase. During the transition phase, the glycerol feed rate is slowly reduced and a predefined amount of methanol is used for induction. The methanol induction phase is very critical for the entire fermentation run, as methanol is used for both cell growth and protein production.

Significance of an on-line model

In general, the fermentation process is monitored and controlled by measuring process vari-

ables such as temperature, pH, DO, agitation, consumption of the substrates, consumption of the nutrients, consumption of oxygen, and evolution of CO_2 to achieve the desired results. The probes are extensively in use for the online measurement of the above-specified variables. However, the variables used for control and monitoring may vary with the type of the microorganism used in the fermentation process and also with the product of interest. During the fermentation of the yeast *P. pastoris*, it has been observed and experimentally proved that the concentration of methanol in the fermentation vessel is critical to the survival of the yeast as well as for protein production. Methanol has to be fed at the rate it is consumed. In other words, excess amounts of methanol may lead to cell death. At the same time insufficient levels of methanol may lead to starvation of cells. The protein production can be optimized by growing the cells at different specific growth rates, which requires an estimate of the cell mass present in the bioreactor.

A number of offline methods are being practiced to measure the cell growth. The offline measurements are performed only at certain stages of the fermentation process. Frequent offline measurements involve intensive labor and use of equipment and supplies, and thus are not considered as a cost-effective approach. However, during model development it is required to measure cell mass as frequently as possible depending on how fast the cells grow. The results from offline measurements are in general either extrapolated or interpolated to predict cell mass. Several mathematical approaches to fit the offline data to a curve are highly prevalent in the industry and also in the research. Apart from the cost perspective, these approaches are prone to inaccurate predictions as they take into account only data from the previous experiments, while ignoring the dynamic conditions of the process for which predictions are applied. In other words, if any fault occurs in the process, for instance, an insufficient supply of oxygen, cell mass will be lower than the predicted. In such case, a pure mathematical model will result in feeding excess amounts of methanol, leading to cell death. A model or a sensor that can predict or measure the cell mass online, taking into consideration the existing conditions, is expected to yield the best results. Above all, the accuracy of the equipment is critical as most of the equipment has limited operating range.

Proposed model: The variables for the current model are selected on the basis of the available methanol metabolic pathway (Figures 1 and 2). However, the selection of the variables (methanol consumption, oxygen consumption, carbon dioxide evolution, and biomass concentration) is limited to their on-line measurable capabilities and their role in developing advanced control strategies for methanol.

Criterion for selection of the model variables: Alcohol oxidase is the first enzyme in the methanol pathway, converting methanol to formaldehyde. The product is then follows two different routes (equations 1 and 2); one route leads to the formation of biomass and the other is the respiratory pathway resulting in CO_2 evolution:

$$CH_3OH + 0.5\ O_2 \rightarrow HCHO + H_2O \quad 1)$$

$$HCHO + O_2 \rightarrow CO_2 + H_2O \quad 2)$$

As seen from reaction 1, 0.5 mole of oxygen is consumed per mole of methanol. In the second reaction, one mole of oxygen consumed results in one mole of CO_2.

The above two reactions explain the importance of including methanol consumption, CO_2 evolution, and O_2 consumption as model variables. The pathways in equations 1 and 2 leading to

cell mass signify the relationship among the biomass and the above three variables. The desired goal of any fermentation experiment is to maximize protein production. Including protein production in the model is also important as the methanol consumed for biomass conversion in most of the occasions is strongly affected by the amount of the protein produced. Under the assumption that the methanol flux for maintenance also includes protein production, biomass formation is lower under high maintenance than when protein production is higher[1] (Figure 6). However oxygen consumption is higher under high maintenance conditions. Thus by including oxygen consumption, we believe protein production may not necessarily be included as a model variable if the model has to be used for developing methanol feed strategy. To add to this argument, to our knowledge there is no evidence for direct on-line analysis of protein production. Protein analysis is a complex procedure and varies from protein to protein. In most occasions, it is possible to arrive at comparably low yields of targeted protein.

Neural networks as function approximator: The nonlinearity in the fermentation of *P. pastoris* can be obviously evidenced by looking at the Figures 3–6 from the research by Vijay P. Jain, a recent master's graduate in our group, whose work has not been published yet. The observations from the figures are not discussed here, as the main purpose of those figures is to show that the effects of the fermentation state variables on the model variables are nonlinear.

Neural networks alone[20] or in combination with fuzzy logic[14–16] or several other function approximators[13,17,19] have been applied to model the fermentation processes of various microorganisms such as *E. coli*[14], baker's yeast[13], *Saccharomyces cerivisiae*[15,16], and *Z. mobilis*[12]. The fermentation areas to which neural networks have been applied include but are not limited to process fault detection[21–22], state estimation, process control[14,16] and optimization[18–20] of the fermentation process of interest to the researchers.

The common limitations in the published models are:

- One step ahead predictions based on fermentation time as a model variable
- Including the fermentation state variables in the model, which are not varied in a single experiment
- Off-line predictions only due to the absence of proper data acquisition system and neural net processing system
- How different is the test data from the training data? Is questionable as not properly stated
- The data used for the modeling appears to be either from process simulations or from experiments with less understanding of the problem of focus
- The applicability of models to develop control strategies is questionable

Although the consequences of each of these limitations can be explained in detail, it is presumed to be beyond the scope of the proposal. The outstanding features of the proposed model are believed to address these limitations. To our knowledge, application of on-line neural networks to make real-time predictions of cell mass based on on-line measurable dynamic variables and the significance of the proposed model to develop control strategies for the fermentation of *P. pastoris* is considered as a novel research topic.

Materials and methods

Host strain: *P. pastoris* mut$^+$ expressing BotNT-E(Hc) or BotNT-C (Hc) or wild-type.

A shake flask containing 200 mL of the BMGY medium with the following ingredients: 1% yeast extract, 2% peptone, 100 mM potassium phosphate, pH 6.0, 1.34% yeast nitrogenous base

with ammonium sulfate and without amino acids, 0.00004% biotin, and 1% glycerol (all % are w/v) will be inoculated aseptically with 1 mL of the frozen culture from glycerol. The culture in the shake flask will be grown at 30°C at 200 rpm for about 24 h until the OD_{600} reaches 2–4.

Batch phase: The culture from the shake flask will be transferred aseptically to a 19-L capacity Bioengineering NLF type fermentor, containing 10 L of the basal salts medium (BSM) with 40.0 g glycerol, 26.7 mL of 85 % H_3PO_4, 0.93 g $CaSO_4$, 18.2 g K_2SO_4, 14.9 g $MgSO_4.7H_2O$, 4.13 g KOH, and 0.435% (v/v) PTM1, which consists of 6.0 g $CuSO_4.5H_2O$, 0.08 g NaI, 3.0 g $MnSO_4.H_2O$, 0.2 g $Na_2MoO_4.2H_2O$, 0.02 g H_3BO_3, 0.5 g $CoCl_2$, 20.0 g $ZnCl_2$, 65.0 g $FeSO_4.7H_2O$, 0.2 g biotin and 5.0 mL H_2SO_4. All units are per liter unless specified otherwise. The microorganism will be grown at 30°C, pH 5.0 maintained with NH_4OH, and an air flow rate of 10 L/min. DO will be maintained at 40 % saturation or more by adjusting the agitation from 200 to 1000 rpm with cascade control strategy between DO and agitation PLCs. Once the agitation reaches a maximal operational limit of 1000 rpm, cascade control will be turned off and agitation will be maintained there. The duration of the batch phase is typically 18–24 h. Depletion of the nutrients in the initial batch medium or the end of the batch phase will be recognized by a DO spike.

Fed-batch phase: Glycerol 50% (v/v) will be fed at a constant rate of 13.3 g/L/h over 1 h using a peristaltic pump. DO will be maintained at a minimum of 40 % by automatic adjustment of oxygen flow rate. Temperature and pH were maintained at 30°C and 5.0, respectively.

Induction phase: A 100 % methanol solution containing 12 mL/L PTM1 will be used as inducer. 2 mL of methanol + PTM1 solution per L of cell broth will be injected at the end of the glycerol fed-batch stage. Methanol concentration in the vapor space will be measured by analyzing the off-gases by ThermOnix Prima μB gas analyzer (mass spectroscope). Concomitantly glycerol will be ramped from 13.3 g/L-h to 0.0 g/L-hr over 3 h. Once the injected methanol is consumed, methanol solution (100%) + 12 mL/L PTM1 will be fed via a peristaltic pump either by exponential feed strategy or by constant residual methanol strategy, as discussed in the following sections. Induction phase will be normally continued for 9 h before harvesting.

Constant residual methanol feed strategy: Methanol will be fed in such a way that the methanol concentration in the vapor phase will be maintained at a level corresponding to the methanol vapor phase composition soon after the specified quantity (refer to induction phase description above) of methanol is injected to induce protein production. A methanol sensor will be used by Zhang et al.[5,8,9] to measure the methanol concentration. The concentration of methanol in the off-gases will be analyzed by mass spectroscope. There are several other methods[1,2,5,6] prevalent for analyzing methanol concentration.

Exponential feed strategy[5,8,9,27]: Methanol feed rate is given by $F = \alpha X_0 V_0 e^{\mu t}$ where F is the feed rate (g/h), α is the specific methanol consumption rate (h^{-1}), X_0 is the cell density (g/L) at the beginning of induction phase, V_0 is volume (L) at the start of induction phase, μ is the specific growth rate (h^{-1}), and t is induction time. α will be calculated by growing cells at their maximal specific growth rate using constant residual methanol feed strategy.

Cell concentration: The following methods will be used initially to measure the cell concentration. Calibration curves will be obtained to relate these methods. The appropriate method will be used for further analysis.

a. *Optical density (OD_{600}):* Optical density will be measured at a wavelength of 600 nm. Concentrated cell broth will be diluted so that the OD_{600} is linear.
b. *Wet cell weight (WCW)*: 10 mL cell broth in a pre-weighed 15-mL conical tube will be spun at speed of 8000–10000 rpm for 10–15 min. The supernatant will be decanted. WCW will be obtained from the difference between the cell pellet + conical tube and the initial weight of the tube.
c. *Dry cell weight (DCW):* The cell pellet obtained as described in the measurement of WCW will be washed with distilled water and dried to a constant weight at 80 °C.
d. *Viable cell counts:* Number of viable cells can be determined by counting the number of colonies on agar plates. Details of this procedure are to be obtained from molecular biology division of BPDF.
e. *Flow cytometry:* A Partec PAS flow cytometer (Partec GmbH, Munster, Germany)[7] equipped with a 488 nm argon laser can be used. Cell pellet from the samples will be diluted with PBS (0.16 M NaCl, 0.003 M KCl, 0.008 M Na_2HPO_4, and 0.001 M KH_2PO_4, pH 7.3). 25 µL of a stock solution containing 200 µg/mL propidium iodide (Sigma, P-4170) dissolved in water will be used for staining. This solution will be added to a 975 µL of diluted sample at room temperature. The Partec true volumetric absolute counting function will be utilized for concentration determination.

Protein concentration: The concentration of the total soluble protein will be analyzed by Brad Ford's assay method[4]. HPLC-based method for analyzing BotNT-E (Hc) is being developed by quality analysis group at BPDF. This method can be used for analyzing the specific protein concentration.

Methanol utilized for maintenance: During the methanol induction phase, methanol is fed at two different rates, y_1 and y_2 g/L of the cell broth. If wet cell weights corresponding to these feed rates are X_1 and X_2 g/L of the cell broth, respectively, linear fit of these values to equation y (methanol feed rate) = mX (wet cell weight) + c results in the methanol used for maintenance as the intercept of the linear graph, which is c.

Methanol consumption because of the additional burden of the expressed protein: This is the difference between the methanol utilized for maintenance incase of foreign protein strain and that in the wild stain.

CO_2 evolution rate (CER): ThermOnix Prima µB gas analyzer is used to analyze the amounts of CO_2 present in the inlet air and off gas.

Oxygen uptake rate (OUR): ThermOnix Prima µB gas analyzer is used to analyze the amounts of O_2 present in the inlet air and off gas.

Methanol consumption rate (MCR): Mettler-Toledo weighing scale provides the updates of the weight of the methanol feed on the scale.

Software: NOL Studio® is used to obtain neural network architecture and the weights. This information is fed to NOL® as a .CSV file. NOL is an on-line neural network processing tool embedded with in Batch Expert®, the software that is used to control the fermentation process and is interfaced with mass spectroscope, SQL server 2000 database and Nematron OPC server

using DDE, ODBC and OPC protocols. It is this data acquisition system that makes this research possible and outstanding. A great deal of time and resources were spent on establishing the data acquisition system (Figure 7).

Experimental design: The fermentation state variables include but not limited to pH, temperature, strain type, gene copy number, recombinant protein expressed, and medium type.

- The experimental system will be perturbed by varying only one variable from one experiment to the next. However, within any experiment, all the fermentation state variables including the methanol feed strategy are either fixed or controlled.
- Constant residual methanol feed strategy will be used to grow the cells at the maximal specific growth rate, while exponential feed strategy will be used to grow the cells at a given specific growth rate. A correction factor for biomass will be used to compensate for any deviation of the observed specific growth rate from the expected specific growth rate while using exponential feed strategy.
- Temperature can be varied from as low as 12°C to as high as 35°C.
- pH can be varied with in a range of 3–7.
- Strain types to be considered: *Pichia* mut$^+$/*Pichia* mut$^-$.
- Expressed foreign protein considered: BotNT-E (Hc)/BotNT-C (Hc)/No foreign protein.
- After each experiment, a neural network model is developed in NOL Studio and then the model will be utilized in NOL to make on-line predictions from second run itself. Error will be calculated. The applicability of all four types of neural networks: Back-propagation, auto-associative, radial basis and rho net will be tested. This strategy forms the best testing procedure as every new run will be under a different set of conditions. At this point it is hard to predict the number of runs required for the model development.

Investigation is required in the following areas:

- Determine the most suitable equivalent for each one of the on-line measurable dynamic variables in addition to the cell concentration
- Methanol feed strategy to be used for training data collection
- How far the actual specific growth rate deviates from the expected specific growth rate while feeding methanol using exponential feed strategy? Currently it is assumed that there is a significant difference between these two variables in a few cases at least.

References

1. Jahic, M., Rotticci-Mulder, J.C., Martinelle, M., Hult, K., and Enfors, S.-O. Modeling of growth and energy metabolism of *Pichia pastoris* producing a fusion protein, *Bioproc. Biosyst. Eng.* 2002, **24**, 385–393.
2. Inan, M., Chiruvolu, V., Eskridge, K.M., Vlasuk, G.P., Dickerson, K., Brown, S., and Meagher, M.M. Optimization of temperature-glycerol-pH conditions for a fed-batch fermentation process for recombinant hookworm (*Ancylostoma canium*) anticoagulant peptide (AcAP-5) production by *Pichia pastoris. Enz. Microb. Technol.* 1999, **24**, 438–445.
3. Trinh, L.B., Phue, J.N., and Shiloach, J. Effect of methanol feeding strategies on production and yield of recombinant mouse endostatin from *Pichia pastoris. Biotechnol. Bioeng.* 2003, **82**, 439–444.
4. Bradford, M.M. A rapid and sensitive method for the quantification of microorganism quantities of protein utilizing the principle of protein-dye binding. *Anal. Biochem.* 1972,

248–254.
5. Zhang, W.Z., Bevins, M.A., Plantz, B.A., Smith, L.A., and Meagher, M.M. Modeling *Pichia pastoris* growth on methanol and optimizing the production of a recombinant protein, the heavy-chain fragment C of Botulinum neurotoxin, serotype A. *Biotechnol. Bioeng.* 2000, **70**, 1–8.
6. Inan, M., and Meagher, M.M. Non-repressing carbon sources for alcohol oxidase (AOX1) promoter of *Pichia pastoris. J. Biosci. Bioeng.* 2001, **6**, 585–596.
7. Jahic, M., Wallberg, F., Bollok, M., Garcia, P. and Enfors, S.-O. Temperature limited fed-batch technique for control of proteolysis in *Pichia pastoris* bioreactor cultures. *Microbial cell factories* 2003, **2**, 1–6. http://www.microbialcellfactories.com/content/2/1/6.
8. Zhang, W.Z., Smith, L.A., Plantz, B.A., Schlegel, V.L., and Meagher, M.M. Design of methanol feed control in *Pichia pastoris* fermentation based upon a growth model.
9. Zhang, W.Z., Inan, M., and Meagher, M.M. Fermentation strategies for recombinant protein expression in the methylotropic yeast *Pichia pastoris. Biotechnol. Bioproc. Eng.* 2000, **5**, 275–280.
10. Ren, H.T., Yuan, J.Q., and Bellgardt, K.-H. Macrokinetic model methylotropic *Pichia pastoris* based on stoichiometric balance. *Journal of Biotechnology* 2003, **106**, 53–68.
11. Stratton, J., Chiruvolu, V. and Meagher, M. High cell-density fermentation in *Pichia protocols* (Higgins, D. R. and Cregg, J. M., eds.) 1998, 107–121, Humana Press, Totowa, NJ.
12. Karim, M.N.,Yoshida, T., Riviera, S.L., Saucedo, V.M., Eikens, B., and Oh, G.-S.. Global and local neural network models in biotechnology application to different cultivation processes. *J. Ferment. Bioeng.* 1997, **83**, 1–11.
13. Eikens, B., and Karim, M.N. Process identification with multiple neural network models. *Internat. J. Control* 1999, **72**, 576–590.
14. Kaiming, Y.E., Jin, S. and Shimizu, K. Fuzzy neural network for the control of high cell density cultivation of recombinant *E. coli. J. Ferment. Bioeng.* 1994, **77**, 663–673.
15. Jin, S., Shimizu, K., and Nikawa, J.. Application of artificial neural network and fuzzy control for fed-batch cultiation of recombinant *Sacchromyces cerevisiae. J. Ferment. Bioeng.* 1996, **81**, 412–421.
16. Yuan, Y.-J. Miao, Z.-Q., and Li, S.-Y. The fuzzy neural network controller in yeast fed-batch fermentation. *Chem. Eng. Comm.* 1999, **174**, 167–183.
17. Tholudur, A., Ramirez, W.F., and McMillan, J.D. Interpolated parameter functions for neural network models. *Comput. Chem. Eng.* 2000, **24**, 2545–2553.
18. Tholudur, A., and Ramirez, W. F. Neural-network modeling and optimization of induced foreign protein production. *AIChE J.* 1999, **45**, 1660–1670.
19. Tholudur, A., and Ramirez, W. F. Optimization of fed-batch bioreactors using neural network parameter function models. *Biotechnol. Prog.* 1996, **12**, 302–309.
20. Chaudhuri, B., and Modak, J.M. Optimization of fed-batch bioreactor using neural network model. *Bioproc. Eng.* 1998, **19,** 71–79.
21. Liu, W. An extended Kalman filter and neural network cascade fault diagnosis strategy for the glutamic acid fermentation process. *Artific. Intell. Eng.*1999, **13**, 131–140.
22. Shimizu, H., Yasuoka, K., Uchiyama, K., and Shioya, S. Bioprocess fault detection by nonlinear multivariate analysis: Application of an artificial autoassociative neural network and wavelet filter bank. *Biotechnol. Prog.* 1998, **14**, 79–87.
23. Brierley, R.A., Bussineau, C., Kosson, R., Melton, A. and Siegel, R.S. Fermentation development of recombinant *Pichia pastoris* expressing the heterologus gene: Bovine lysozyme.

Ann. N.Y. Acad. Sci. 1990, **589**, 350–362.
24. Cregg, J.M., and Higgins, D.R., Production of foreign proteins in the yeast *Pichia pastoris. Can. J. Bot.* 1995, **73**, 91–97.
25. Cregg, J.M., and Madden, K.R., Development of the methylotropic yeast, *Pichia pastoris,* as a host system for the production of foreign proteins. In: Peirce, G., ed.. *Devel. Indust. Microbiol.* 1988, **29**, 33–41.
26. Ellis, S.B., Brust, P.E., Koutz, P.J., Waters, A.E., Harpold, M.M., and Gingeras, T.R. Isolation of *alcohol oxidase* and two other methanol regulatable genes from the yeast *Pichia pastoris. Mol. Cellular Biol.* 1985, **5**, 1111–1121.
27. Sinha, J., Plantz, B.A., Zhang, W., Gouthro, M., Schlegel, V., Liu, C., and Meagher, M.M. Improved production of recombinant ovine interferon-τ by mut$^+$ strain of *Pichia pastoris* using an optimized methanol feed profile. *Biotechnol. Prog.* 2003, **19**, 794–802.

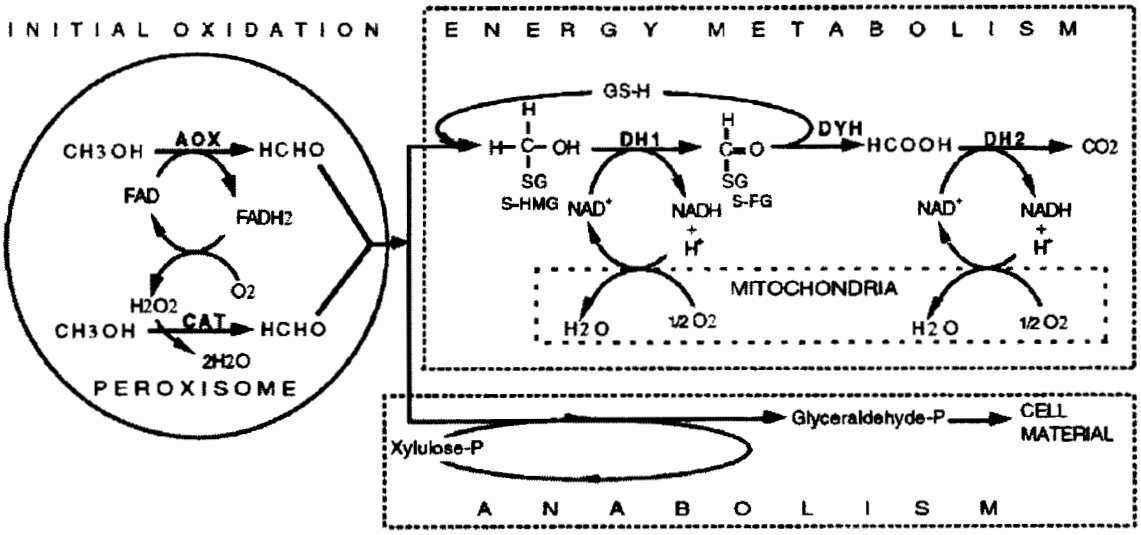

Figure 1. Metabolism of methanol by *P. pastoris*. AOX: alcohol oxidase; DH2: formaldehyde dehydrogenase; CAT: catalase; S-HMG: S-hydroxy-methylglutathione; DYH: S-formyl-glutathione-hydrolase; G-SH: reduced glutathione [1] (The above figure is reproduced from the cited journal article).

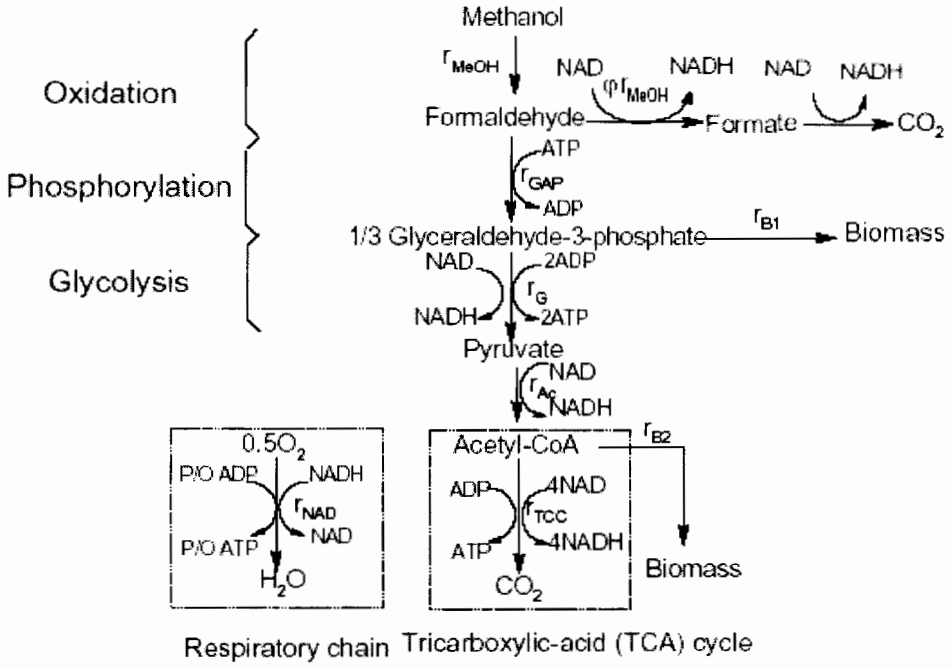

Figure 2. Metabolic pathways of methanol in *Pichia pastoris*[10] (The above figure is reproduced from the cited journal article).

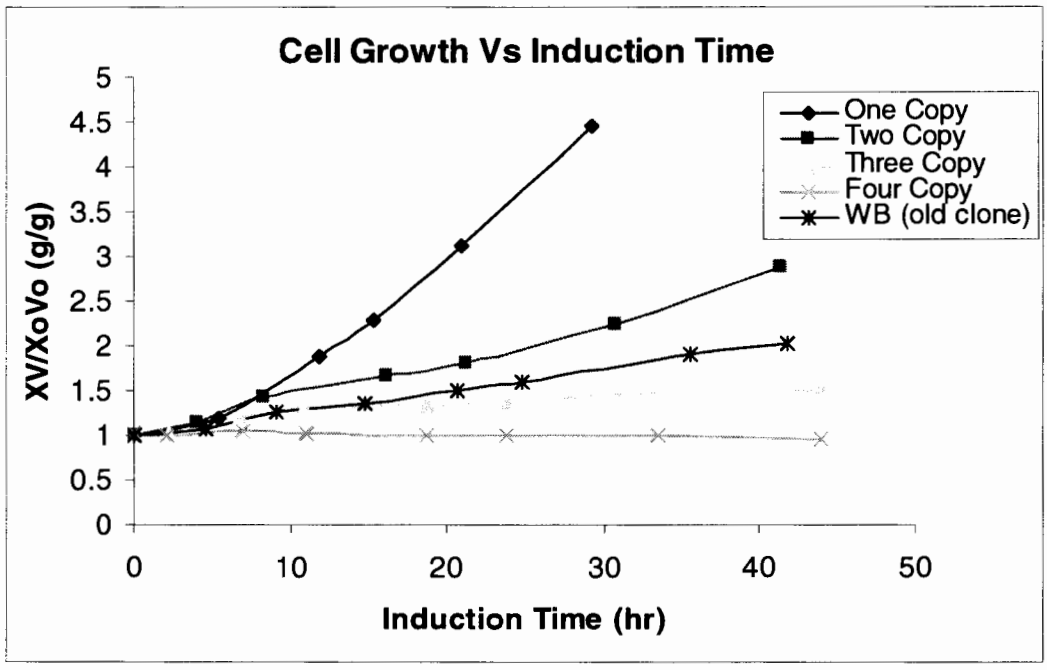

Figure 3. The effect of gene copy number on the cell growth.

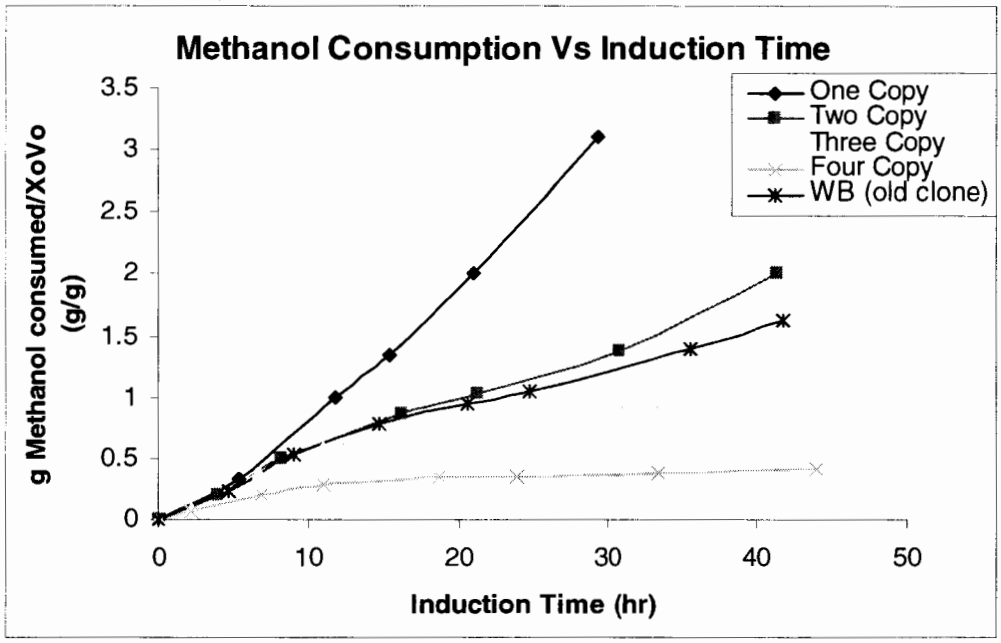

Figure 4. The effect of the gene copy number on the methanol consumption.

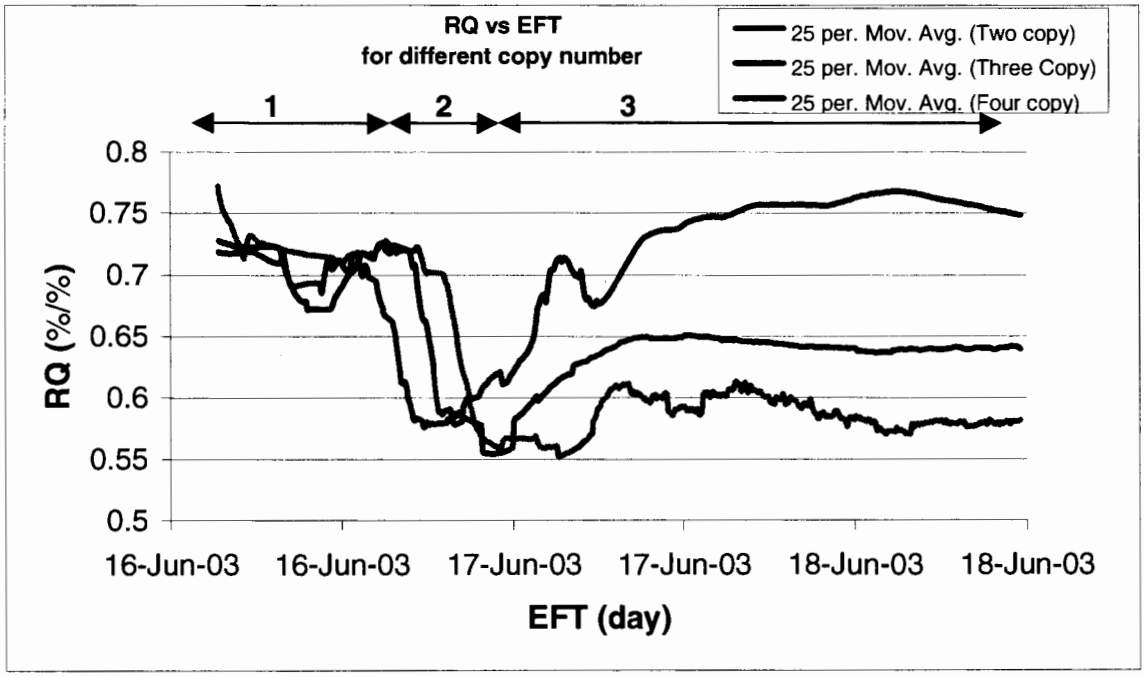

Figure 5. Effect of the gene copy number on the respiratory quotient (RQ). Area 3 in the figure represents induction phase.

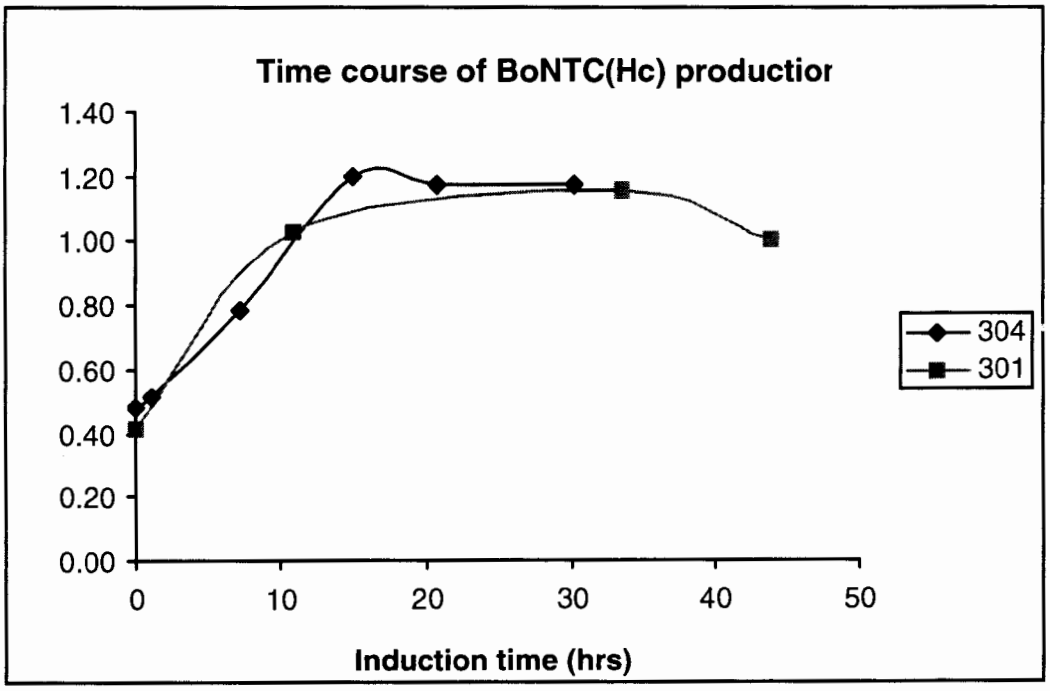

Figure 6. The nonlinearity of the protein production in run #s WZ- BotC-304 and 305.

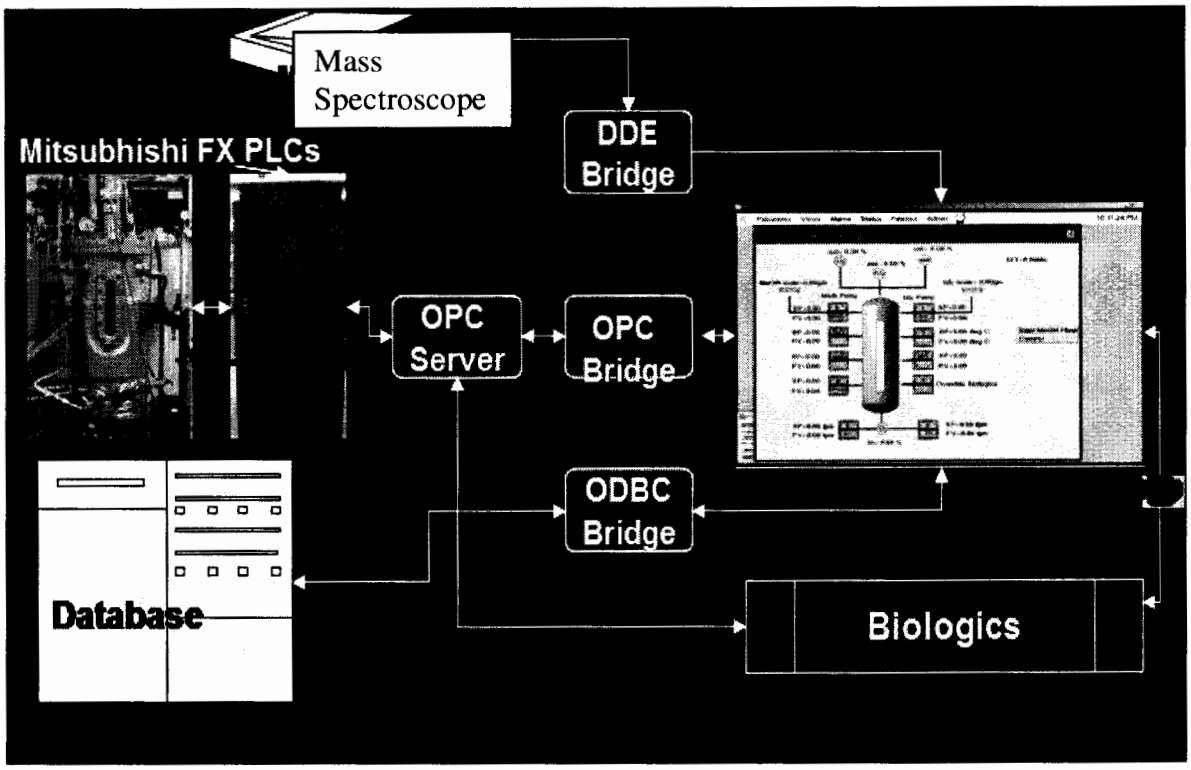

Figure 7. Data acquisition system for on-line neural network processing.

Toxicity of RDX on Germination of *Arabidopsis thaliana*

Sarah Rollo[1], Hangsik Moon[2], Murali Subramanian[1],
David J. Oliver[2], and Jacqueline V. Shanks[1]
Departments of Chemical Engineering[1] and Genetics, Development and Cell Biology[2],
Iowa State University, Ames, Iowa 50011

Abstract

Several ammunition manufacturing, packing, and testing sites have possible soil and groundwater contamination from energetic materials, such as RDX and TNT. Phytoremediation is an emerging technique that has the potential to remove energetic materials from soil and water, while being an inexpensive, self-sustaining, and environmentally friendly process. It is believed that RDX may be taken up by plants and stored as a parent compound. Currently, it is not understood what transformation pathway is used in the phytoremediation process or if any residue is returned to the soil or water. Before this technology can be applied, there must be a general understanding of how phytoremediation works. The goal of this research is to construct a genetic and biochemical knowledge base for the transformation pathway of RDX.

This study consists of evaluating the germination of *Arabidopsis thaliana* wild-type seeds in order to determine the toxicity level of RDX in solid media. The results of this work will be used to identify the concentration of RDX that should be used to screen mutant seeds. The concentration of seeds must also be determined by the assay. This study showed that future work should focus on using 1000 to 1500 mg/L RDX with 2000 seeds per plate. These conditions will be used to screen *A. thaliana* mutant seeds and select plants that perform better than the wild-type in the presence of high RDX concentrations. Selected mutants will be used to determine if there is a common gene that enhances remediation of RDX and/or limits the toxicity of RDX to the plant.

Introduction

The energetic materials RDX, TNT, HMX, and DNT have contaminated groundwater and surface soil at many Department of Defense training and testing sites. Phytoremediation can be used to continually reduce the level of energetic materials in the soil (1). Knowledge about the transformation pathways of RDX and other energetic materials would greatly increase our understanding of how phytoremediation occurs. With understanding of the transformation pathways, native plants could be selected by how well RDX is transformed, while mutant plants could be generated to enhance transformation. A well-defined pathway would also help identify what end products are formed by the remediation of RDX. In order to make the phytoremediation process more effective, a knowledge base of important genetic sequences and biochemical reaction pathways must be formed.

RDX (hexahydro-1,3,5-trinitro-1,3,5-triazine) is deposited on soil at ammunition manufacturing sites and testing sites. Once RDX has contaminated the soil, it can easily contaminate the groundwater, where it is particularly mobile (1). RDX is toxic to plants, animals, and humans, but can be taken up by some plants to reduce contamination of groundwater (2). RDX is thought to be incorporated into the biomass of the plant as a parent compound, since oxidation/reduction and conjugation occur less frequently than with other energetic materials (3).

The objective of our research is to use *Arabidopsis thaliana* mutants to determine if there are certain genes that promote RDX uptake and remediation, along with establishing a biochemical pathway in plants. *A. thaliana* is a useful model plant due to its small size, short life span and

relatively simple genome (4). The transformation pathway of RDX in plants is still unknown, which makes it especially important to study this energetic material in depth. Since little is known about the transformation pathway of RDX, it is unclear if or how RDX is trans-formed, as well as what the end products of phytoremediation are. It is also not known what genetic mutations enhance RDX uptake and metabolism.

By exploiting the fact that RDX is toxic to plants, we can screen *A. thaliana* mutant seeds for plants that can survive exposure to high levels of RDX. Studying these mutants will then allow us to examine if there are recurrent genes that are present. Since the *A. thaliana* genome has been fully sequenced, it will be possible to identify the genes responsible for the metabolism of RDX. Metabolic analysis can then be used to determine exactly what step of the metabolism is altered by the mutation. Once the metabolic outcome and the genetic mutation are known, the role of the gene in the transformation pathway can be determined.

Before *A. thaliana* mutants can be screened and studied, the toxicity level for *A. thaliana* wild-type plants must be determined. The toxicity of RDX to some plants has been documented, but there is currently no information in the literature on the toxicity of RDX on *A. thaliana* (2, 4). Initial concentrations of RDX to study were estimated from previous phytoremediation work (5, 6, 7). Various concentrations of RDX were tested to evaluate the toxicity effects that RDX has on the germination of *A. thaliana* wild-type seeds in solid media. The time of germination was recorded for each concentration of RDX. The size of the plants was monitored for several weeks to determine how wild-type plants respond to growing in media containing RDX.

Materials and Methods

Half-strength Murashige and Skoog (MS) medium was used for all experiments. Medium consisted of 2.2 g of MS salt mixture, 3 mL of a 6% potassium phosphate monobasic (KH_2PO_4) solution, 1 mL of Gamborg's vitamin B_5 solution, 20 g of sucrose, and 5 g of 99% MES (2-morpholinoethanesulfonic acid) hydrate added to 1 L of water. The pH was adjusted to 5.8 with NaOH. Phytagel was then added to the media (2.0 g/L media) and the media was autoclaved.

RDX was obtained in acetone from AccuStandard and in acetonitrile from ChemService. The MS salt mixture was purchased from Gibco BRL Life Technologies. Potassium phosphate monobasic was obtained in crystal form from Fisher Scientific. Gamborg's vitamin B_5 solution came from Sigma. Sucrose was purchased from Midwest Scientific. 99% MES hydrate was obtained from Acros Organics. Phytagel was obtained from Sigma.

Seeds were sterilized by one of two methods. The first method consists of applying 20% bleach to seeds for 15 min and then rinsing with sterile water three times. The second method sterilizes seeds by exposing seeds to chlorine gas for 3 h. The chlorine gas is formed by combining 200 mL bleach with 20 mL concentrated HCl in a closed container.

Medium was autoclaved and then cooled in a 65°C water bath. RDX and acetone were added to the medium which was then poured into sterile petri dishes. The petri dishes were then cooled to let the media solidify. Then sterilized seeds were plated on the media. Lids were placed on the petri dishes, which were sealed with Parafilm to prevent evaporation and reduce the risk of contaminating the plates. Plates were then placed in a cold room at 4°C. After three days, the plates were then moved to the growth room to germinate, where they were kept at 22°C with constant light. Seeds were monitored to record the time of germination and the size of the plants over several weeks. Some plants were then transferred to clean media, with no acetone or RDX, or to soil to observe if they would be able to fully mature after exposure to high RDX concentrations.

Wild-type seeds were grown in solid media containing various concentrations of RDX in

order to determine the toxicity of RDX on germination. Concentrations of RDX in the media ranged from 10 mg/L to 2000 mg/L. RDX was first obtained in a solution of acetonitrile (1000 μg/mL) from ChemService. Later, RDX was obtained in a more concentrated solution of acetone (50 mg/mL) from AccuStandard. Acetone concentrations were kept the same throughout a screening assay in order to compare the effect of the RDX only. Four replicates were used for each concentration of RDX studied. Two controls were used for the screening; one control consisted of media with no acetone or RDX added, while the other control consisted of media with acetone only. By using two controls, the toxic effects of RDX in acetone could be monitored by comparison with the first control and the toxic effects of RDX alone could be monitored by comparison with the second control. This allowed us to observe the effect of several concentrations of RDX on germination, by comparing those seeds to the controls. Various concentrations of seeds were also used to observe the effect that seed concentration had on RDX toxicity. Seed concentrations ranged from 75 to 2000 seeds per plate.

Results

RDX concentrations from 0 mg/L to 2000 mg/L were tested to determine the RDX level that will be used for mutant screening. Precipitation was first observed at 500 mg/L RDX and significant precipitation of RDX occurred at levels above 1000 mg/L RDX. Acetone concentrations remained at or below 40 mg/L. Seed concentrations ranged from 150 seeds per plate to 2000 seeds per plate. With higher concentrations of RDX, several toxic effects were observed, including stunted germination and plant growth. Although RDX stunted the germination of the seeds, all seeds eventually germinated at the RDX concentrations tested. This study determined that *A. thaliana* mutant seeds should be screened with an RDX concentration between 1000 and 1500 mg/L RDX with 2000 seeds per plate.

Several experiments with wild-type seeds were conducted to determine the concentration of RDX toxic to *A. thaliana* seed germination and the concentration of seeds to use to screen mutant seeds. An initial experiment with RDX in acetone compared plates with 50, 100, 150, 200, and 250 mg/L RDX. All of the plates had 100 seeds and 5 mL/L acetone. This experiment showed little toxic effect to seeds at any concentration, which demonstrated that the concentrations of RDX were too low and needed to be increased. The next experiment compared RDX concentrations of 500, 1000, 1500, and 2000 mg/L, with 40 mL/L acetone and 100 seeds per plate. The germination of the seeds at high RDX concentrations was severely delayed. Additional experiments were conducted between 1000 and 1500 mg/L RDX at various seed concentrations. The toxic effects on germination and plant growth of these RDX concentrations appeared to be fairly similar. Since the root length was severely stunted in these experiments, 24-day-old plants were transferred to media containing no RDX and to soil to determine if they would be able to develop to maturity. Developing to maturity is a requirement for selected mutants, since seeds need to be collected from the selected plants for future experiments. Plants that were transferred directly to soil had a hard time adjusting with their minimal root length. Plants transferred to media without RDX grew much more easily, which allowed for normal root growth. These plants could then be transferred to soil in order to fully develop. There was little difference between 1000 and 1500 mg/L RDX when observing germination and growth in RDX-containing media, but plants that were less stunted initially were able to develop much more rapidly when transferred to soil. Transplanting these plants to soil helped determine which RDX concentration and seed concentration to select for future work.

Discussion

The experiments demonstrated the toxic effects of high RDX concentrations, as well as showing the germination and growth of wild-type plants. Higher concentrations of RDX show more toxic effects on the germination and growth of the plants. Germination was delayed longer for seeds exposed to higher RDX levels. It should also be noted that the seeds that germinated first, matured first. Age of the plants was determined from the time the seeds were placed in the growth room.

RDX was originally purchased in acetonitrile (1000 μg/mL). One experiment was done to test concentrations of RDX from 0 mg/L to 40 mg/L. All of these plates had 40 ml/L of acetonitrile. Four replicates were used for each concentration. Out of the 20 plates tested, only two plates germinated. One plate was a control with 0 mg/L RDX, while the other plate had an RDX concentration of 30 mg/L. This experiment was inconclusive about the toxicity of RDX, but showed that acetonitrile was too toxic to be used as a solvent for screening studies. This experiment also demonstrated the need for two controls, one with no RDX and no solvent, and a second control with only solvent. Two controls are necessary in order to be able to observe the toxicity of the solvent, as well as the toxicity of RDX.

The results observed in this study can be summarized by three toxic effects. The first is that the concentration of RDX affected seed germination. With increasing concentrations of RDX, the toxic effects on germination also increased, which resulted in longer germination times. This study also showed that acetone was particularly toxic to root length, and these toxic effects also increased with increasing concentrations of acetone. The seed concentration is also an important factor to consider. Decreasing the concentration of seeds per plate increased the toxic effects of both RDX and acetone.

Acknowledgements

This research was supported in part by the U.S. Department of Defense through the Strategic Environmental Research and Development Program (SERDP), Project CU-1319.

References

1. Best, E.P.H., S.L. Sprecher, S.L. Larson, H.L. Fredrickson, and D.F. Bader. Environmental behavior of explosives in groundwater from the Milan Army Ammunition Plant in aquatic and wetland plant treatments: Uptake and fate of TNT and RDX in plants. *Chemosphere* **39**: 2057–2072 (1999).
2. Burken, J. G., J.V. Shanks, and P.L. Thompson. "Phytoremediation and Plant Metabolism of Explosives and Nitroaromatic Compounds," in *Biodegradation of Nitroaromatic Compounds and Explosives*. J. Spain, J. Hughes, and H. Knackmuss, Eds., CRC Press, Boca Raton, FL, 2000.
3. Pennington, J.C., and J.M. Brannon. Environmental fate of explosives. *Thermochim. Acta* **384**: 163–172 (2002).
4. Moon, H., M. Subramanian, S. Rollo, D.J. Oliver, and J.V. Shanks. Use of *Arabidopsis* as a Model System for Genetic and Biochemical Studies of TNT Transformation in Plants. Proceedings of the Batelle Conference on Sustainable Range Management, New Orleans, LA, 2004, in press.
5. Bhadra, R., D.G. Wayment, R.K. Williams, S.N. Barman, M.B. Stone, J.B. Hughes, and J.V. Shanks. Studies on plant-mediated fate of explosives RDX and HMX. *Chemosphere* **44**: 1259–1264 (2001).

6. Subramanian, M., and J.V. Shanks. "Role of plants in the transformation of explosives," in *Phytoremediation: Transformation and Control of Contaminants*. S.C. McCutcheon and J.L. Schnoor, Eds., Wiley, New York, 2003.
7. Shanks, J.V., D.J. Oliver, H. Moon, S. Rollo, and M. Subramanian. Genetic and Biochemical Basis for the Transformation of Energetic Materials (RDX, TNT, DNTs) by Plants. Proceedings of the Annual Meeting of the American Institute of Chemical Engineers, San Francisco, CA, 2003.

Biodegradation of Tetrachloroethylene (PCE) in Soil and Groundwater

S. Santharam[1], J. Ibbini[2], L.C. Davis[2], and L.E. Erickson[1]
Departments of Chemical Engineering[1] and Biochemistry[2], Kansas State University, Manhattan, KS 66506

Abstract

Dry-cleaning installations operating in Manhattan, Kansas have allowed solvents to seep into groundwater through soil. The solvent tetrachloroethylene (perchloroethene, PCE) is used in dry cleaning, and some of it has been found in the soil. This work deals with the PCE pollution caused by 30 years of operation of two dry cleaners in Manhattan, Kansas. PCE is a dense non-aqueous phase liquid and tends to settle down in groundwater; the soluble PCE moves with the groundwater, creating a contaminant plume. The public well supplies in Manhattan are located about 1.2 miles down-gradient of this site, and hence are at risk of contamination. Kansas State University and the Kansas Department of Health and Environment are collaborating in characterizing and remediating this site. Preliminary work conducted by the latter and contractors has revealed that PCE and its degradation compounds such as trichloroethene, *cis*-dichloroethene, and vinyl chloride are found significantly above their maximal contaminant levels at many places along the plume. Remediation feasibility studies are being conducted by mesocosm experiments; a chamber is divided into six channels and filled with soil, and plants are grown on top. Each channel is fed with water at the bottom and collected at the outlet, simulating groundwater flow conditions. PCE is introduced at 2 mg/L in three channels, two of them with alfalfa and the other with grass. After the system has attained steady state, the concentrations of PCE at inlet and outlet are monitored and the amount of PCE disappearing in the soil zone is studied. Efforts are being made to identify any degradation products and to measure their concentrations. Soil and water samples were taken from the site and treated with different amendments in the microcosms. Studies were carried out to determine if the native microorganisms could be stimulated by different treatments to enhance reductive dechlorination of PCE beyond *cis*-dichloroethene. The gas phase of these microcosms is analysed for biodegradation products. This investigation is in progress and preliminary results are presented.

Introduction

Dry-cleaning chlorinated solvents are the second most ubiquitous contaminant, next to petroleum hydrocarbons. The largest use for perchloroethene (PCE) or tetrachloroethene (Table 1) is in dry-cleaning and textile operations, accounting for an estimated 60% of all PCE use in the U.S. in 1991. If PCE is released to soil, it will be subject to evaporation into the atmosphere, leaching into the groundwater, and sorption to soil. Biodegradation may be an important process in anaerobic soils (Sirem Laboratories, 2004; Spectrum Laboratories, 2004). Some of the health hazards of PCE are respiratory tract irritation, skin irritation, eye irritation, central nervous system depression, and cancer in humans (Irwin, 1997).

The hydrogeologic environment significantly affects the fate and transport of chlorinated solvents in the subsurface. There are several physical, chemical, and biological mechanisms that affect the behavior of contaminants in the subsurface, and they can be either destructive or non-destructive. Non-destructive fate and transport mechanisms for PCE are advection, sorption, dispersion, dilution by recharge, and volatilization. Destructive mechanisms are biological (primary growth substrate utilization and cometabolism) and abiotic (reductive dechlorination). Bioremediation, both natural and enhanced has proven to be a powerful approach for remediating chlorin-

ated solvents, including PCE. In recent years, it has become apparent that biologically-mediated degradation mechanisms may be important for chlorinated solvents; for example, iron sulfide may reduce PCE to acetylene (Haas and Wiedemeier, 2004). An anaerobic bacterium, coccoid Strain 195, perfectly reduces the toxic pollutants PCE and trichloroethene (TCE) to nontoxic ethene gas (Maymo-Gatell *et al.*, 1997).

Table 1. Values of the physico-chemical properties of PCE (U.S. EPA, 1994).

Parameter	Value
Molecular weight	165.83
Vapor pressure (mm Hg)	18.47 at 25°C
Density (gm/cc)	1.6227
Dimensionless Henry's constant	0.72 at 25°C
Solubility in water	150 mg/L at 25°C
$\log K_{ow}$ and [$\log K_{oc}$]	3.4 and [2.2–2.7]
Maximum Contaminant Level (MCL) in water	5 µg/L

The Problem

PCE has been deposited in soil by dry-cleaning operations in Manhattan, Kansas; this contamination has been present for more than 30 years. Public water supply wells are located about one mile east of the contaminated zone and are at risk of contamination, since studies by Kansas Department of Health and Environment (KDHE) revealed a groundwater gradient from west to east. Several monitoring wells were installed along the plume to take water samples and to measure relevant parameters including depth to water and PCE concentration. PCE is primarily limited to the source areas; however, trichloroethylene (TCE), a degradation product of PCE, was also detected in the groundwater at concentrations exceeding its maximal contamination level (MCL) (5 µg/L), up to 0.75 mile east of the source. Concentrations of PCE from monitoring well samples were as high as 26 ppm at the source and 7.5 ppm down-gradient (Bruggeman, 2004). Using CPT probes and well cores, the soil to 45 ft below ground surface was clayey grading to sand.

Experimental Systems

Mesocosm: A chamber is divided into six channels with three channels used for this study (Figure 1). Each channel is 1.1 m long x 0.65 m high x 0.1 m wide. The channels are filled with soil; alfalfa is grown in channels 1 and 2 and grass is grown in channel 3. The inlet water, with PCE concentration of ~2 mg/L in the aqueous phase, is fed 5 cm above the bottom of the tank and collected at the outlet on the other side. The depth of saturated zone in the channel is controlled by position of outlet tube (25 cm from the bottom in this system).

Microcosm: Soil microcosms were prepared in 12-ml (nominal volume; actual volume is about 16.4 ml) sterile glass bottles. Five grams of site soil at a depth of 47.5 inches was used on a dry weight basis. Different treatments (Table 2) were then added and the final aqueous phase was brought to 12 ml using sterile distilled water, leaving 4.4 ml of head space in the bottle. The microcosms were then flushed with argon gas to displace the air and quickly sealed with mininert Teflon screw caps. PCE gas (0.5 ml) was then introduced to the system and allowed to partition

by gently shaking on a rotary shaker for 24 h.

Water microcosms were prepared in similar bottles, and the final volume of site water and treatments was 12 ml. Water samples from two monitoring wells, MW4 and MW8, were used in this study. Water from MW8 was taken from two adjacent wells of different depths: the deep well (MW8D) and the shallow well (MW8S). Microcosms were sampled at several time intervals, with 100 µl of headspace injected into the gas chromatograph at 100°C and run for 5 min.

Analytical Methods

Gas chromatography (HP 5890 Series II) with flame ionization detection (FID) using an HP-1 (dimethyl polysiloxane matrix) column was used for headspace analysis of PCE samples; sample volume was 100 µl. Ion chromatography (Dionex) was used for analyzing KBr samples, and the eluent solvent was 9 mM Na_2CO_3.

Table 2. Treatment combinations and concentrations used in soil and water microcosms.

Treatment	1	2	3	4	5	6	7	8	9	10	11
Glucose (0.05%)	-	+	+	+	-	-	-	-	-	-	-
Yeast extract (0.05%)	-	-	+	+	-	+	-	+	-	+	+
Soy oil methyl ester (5 µl)	-	-	-	+	+	+	-	-	-	-	-
Methanol (3 mM)	-	-	-	-	-	-	+	+	-	-	+
Lactate (3 mM)	-	-	-	-	-	-	-	-	+	+	+
PCE gas (3 mg/l in liquid)	+	+	+	+	+	+	+	+	+	+	+

+ indicates addition of the substrate
- indicates absence of the substrate

Results and Discussion

Mesocosm: A tracer study was conducted using KBr in six channels. A 150-ml KBr pulse at 100 mg/L was given to all the channels. Samples were collected from the outlet at intervals of 3 h, 6 h, 12 h, and 24 h on the first and second days. On third and fourth days samples at 5 h and 24 h were collected. From then on a sample was collected each day for 14 days and analyzed for KBr concentration. This study showed that the peak of KBr concentration in the outlet occurred between 1 to 1.5 days, except for channel 1 for which the peak occurred at three days. Channel 1 behavior was very different from other channels, as the KBr concentration reached a peak (smaller magnitude than other channels) at three days and then dropped to almost zero and then picked up and remained constant at about 0.5 ppm. From this study, it can be concluded that the contaminant should appear in the outlet in about 1.5 days. The ratio of outlet to inlet concentrations vs. time is shown for PCE in Figure 2. It can be seen that it takes about 20 days for the system to attain steady state. This is because the initial PCE fed was sorbed to soil; some PCE escapes into the atmosphere through the unsaturated soil region above.

Figures 3–5 show the inlet and outlet PCE concentrations for channels 1–3, respectively. After about 20 days, the inlet concentration was about 2 ppm (2 ± 0.25 ppm) and the outlet concentration was about 1.5 ppm (1.5 ± 0.25 ppm).

Microcosm: Results (Figure 6) showed that the highest degradation rate of PCE was achieved when water or soil was supplemented with yeast extract (YE). In the water microcosms the deep-well samples of MW8 showed better PCE degradation and formation of *cis*-DCE was observed in several treatments. The shallow well samples of MW8 showed low PCE degradation and accumulation of methane in the glucose + soy oil + YE treatment (No. 4 in Table 2). All the treatments of the MW4 samples resulted in large amounts of methane. A similar trend was found in the soil microcosms, except that PCE transformation was faster in water than in soil. This may be due to the fact that the nutrients are more homogenized in water and are readily available for microorganisms than in the soil.

Conclusions

Mesocosm Studies: It takes about 20 days for the system to attain steady state and the outlet concentration to reach a steady value.

Microcosm Studies: None of the treatments above was able to completely degrade PCE beyond *cis*-DCE. Ethene was not detected in these treatments; however, methane was generated. Therefore, further investigation needs to be done with the known bacterial consortium KB1 to determine how effective these treatments are.

Future work

The results from microcosm studies will be utilized to choose the treatment systems to be employed in the mesocosm experiments. The results from both studies will be used to design the remediation process in the site. At present, a 2% glucose solution was fed in channels 2 and 5 to make the bottom soil anaerobic. It is expected that the anaerobic soil will aid in the biological degradation of PCE to TCE and other degradation products. The headspace and soil samples of the channels will be monitored to determine if any degradation compounds are present.

Acknowledgment

The Kansas Department of Health and Environment and the Kansas Agricultural Experiment Station provided financial support.

References

Bruggeman, J.C. and K.C. Wallace, Source Investigation Report No. 01027118: Cinderella Cleaners, Prepared for KDHE, Bureau of Remediation, by Terracon Corp., 2004.

Haas, P.E. and Wiedemeier, T.H. Accelerated Bioremediation, A Training Course by National Groundwater Association, St. Paul, Minnesota, May 11–12, 2004.

Irwin, R.J., Environmental Contaminants Encyclopedia, Entry for Tetrachloroethylene, National Park Service, CO, 1997.

Maymó-Gatell, X, Y. Chien, J. M. Gossett, S. H. Zinder. Isolation of a Bacterium That Reductively Dechlorinates Tetrachloroethene to Ethene. *Science*, 276 (5318), 1568–1571 (1997).

Sirem Labs, Site Recovery and Management, Myths and Realities, 2004.http://www.siremlab. com/myths.asp

Spectrum Laboratories, Chemical Fact Sheet, Groundwater and Wastewater Analyses, 2004. http://www.speclab.com/compound/c127184.htm.

U.S. Environmental Protection Agency, Office of Pollution Prevention and Toxics. Chemical Summary for Perchloroethylene, August 1994. http://www.epa.gov/chemfact/s_perchl.txt.

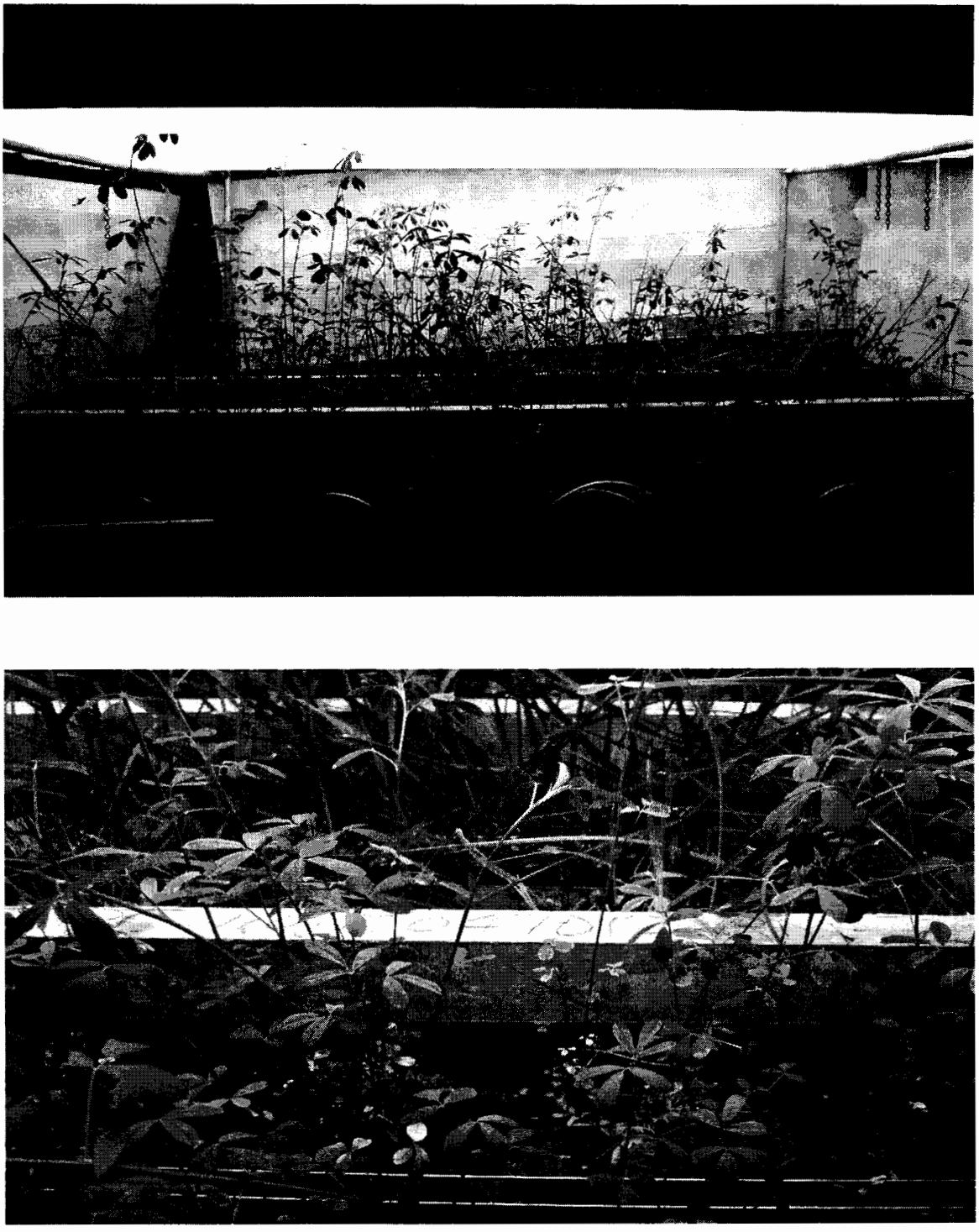

Figure 1: Side (picture above) and top (picture below) view of the channels: Channels 1 and 2 are alfalfa and channel 3 is grass. Lighting is provided by a pair of tube lights for each channel. PCE solution enters from a glass tank on the left side and is collected in a bottle on the right side.

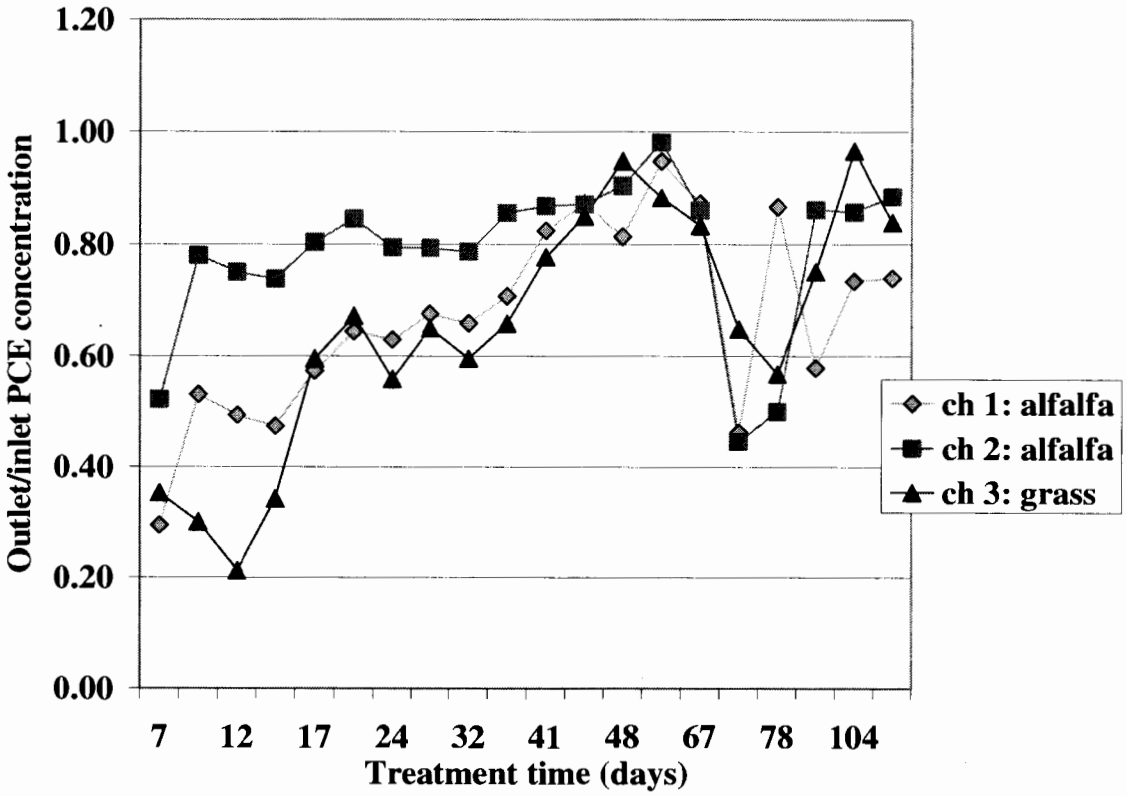

Figure 2. Ratio of outlet to inlet PCE concentrations for three channels described above. Water samples taken on indicated days after beginning exposure.

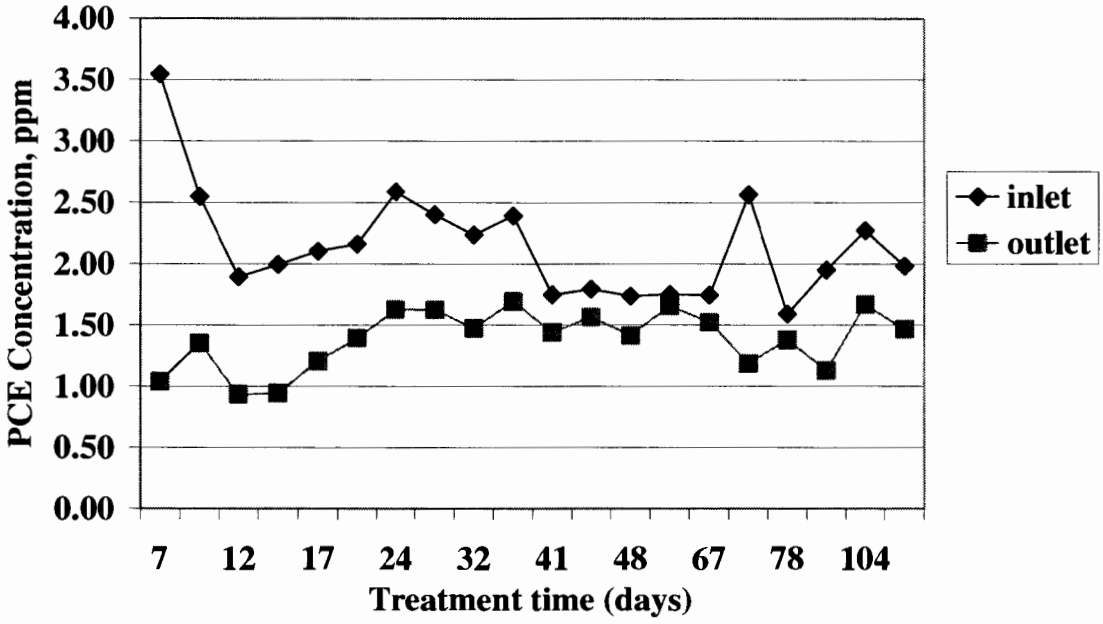

Figure 3. PCE concentrations in inlet and outlet of channel 1. Water samples taken on indicated days after beginning exposure.

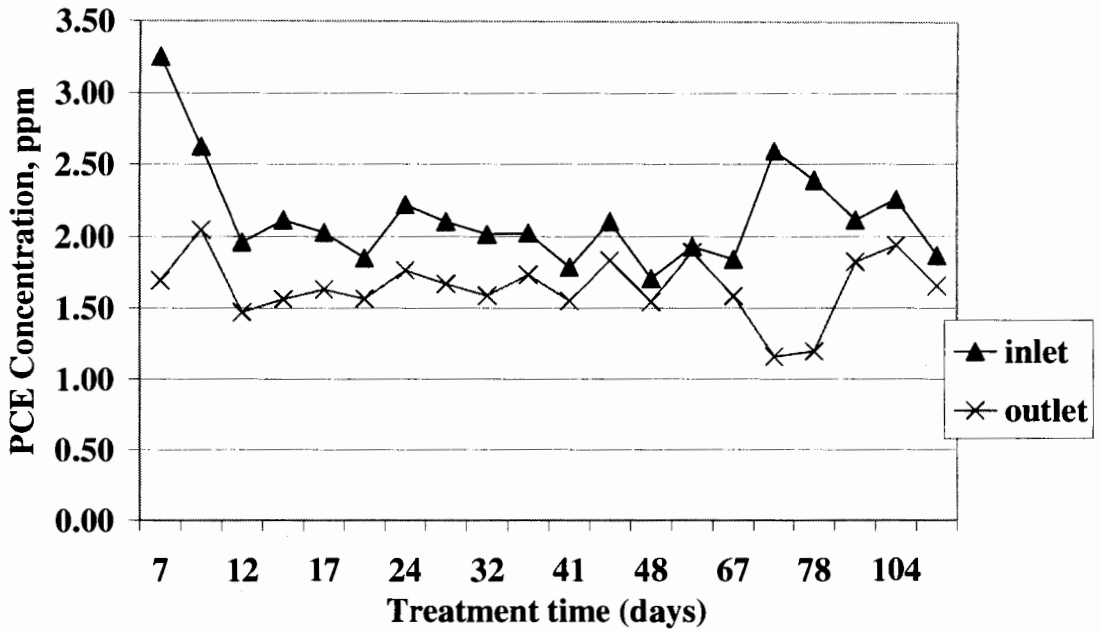

Figure 4. PCE concentrations in inlet and outlet of channel 2. Water samples taken on indicated days after beginning exposure.

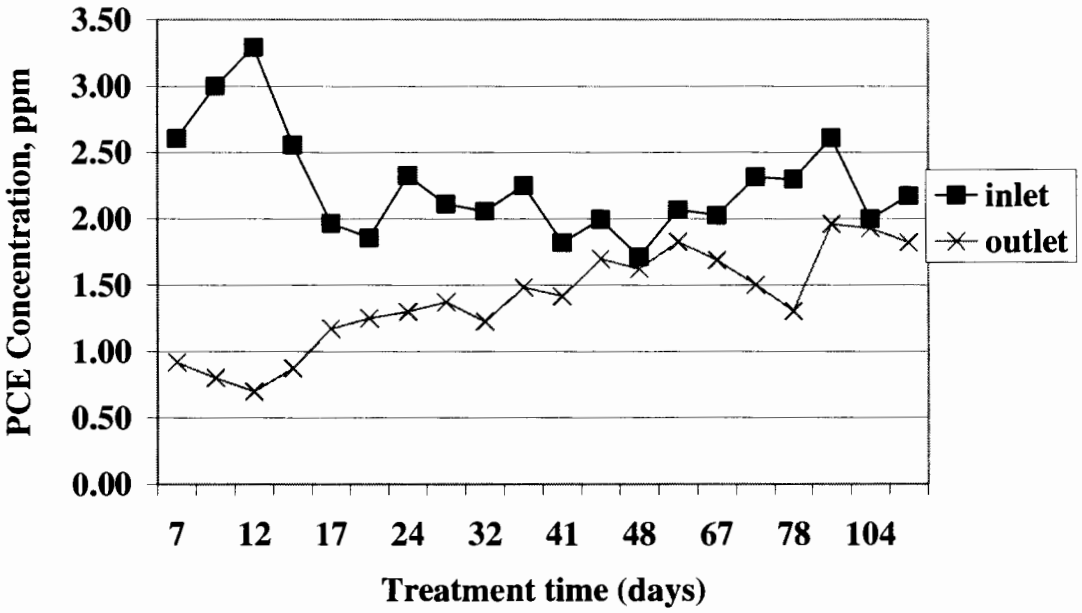

Figure 5. PCE concentrations in inlet and outlet of channel 3. Water samples taken on indicated days after beginning exposure.

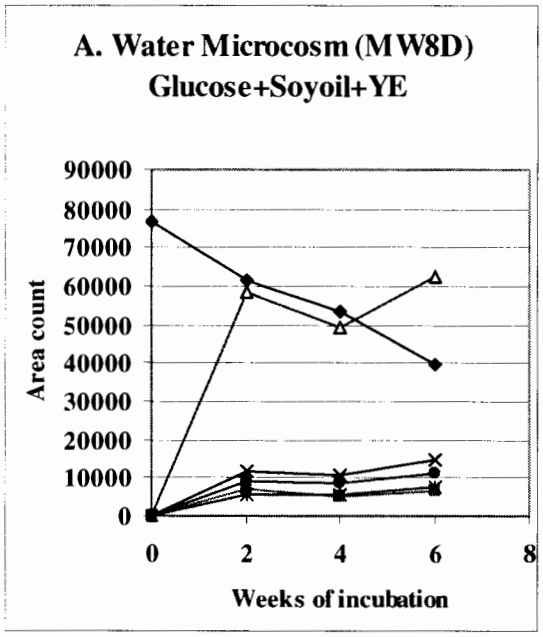
A. Water Microcosm (MW8D)
Glucose+Soyoil+YE
Area count
90000
80000
70000
60000
50000
40000
30000
20000
10000
0
0
2
4
6
8
Weeks of incubation

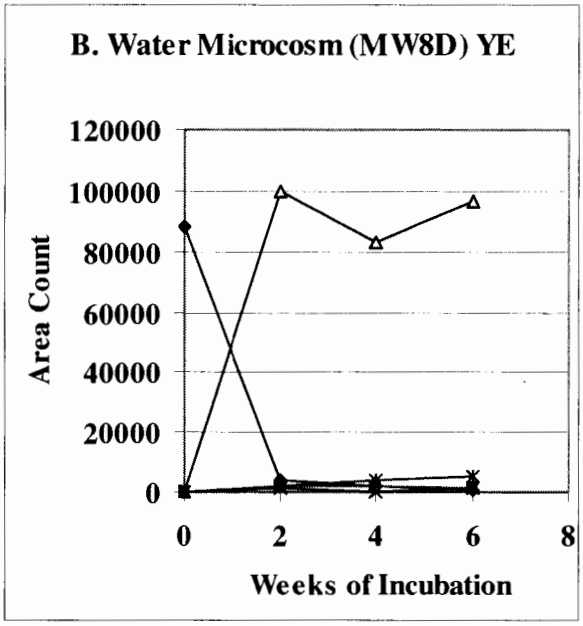
B. Water Microcosm (MW8D) YE
Area Count
120000
100000
80000
60000
40000
20000
0
0
2
4
6
8
Weeks of Incubation

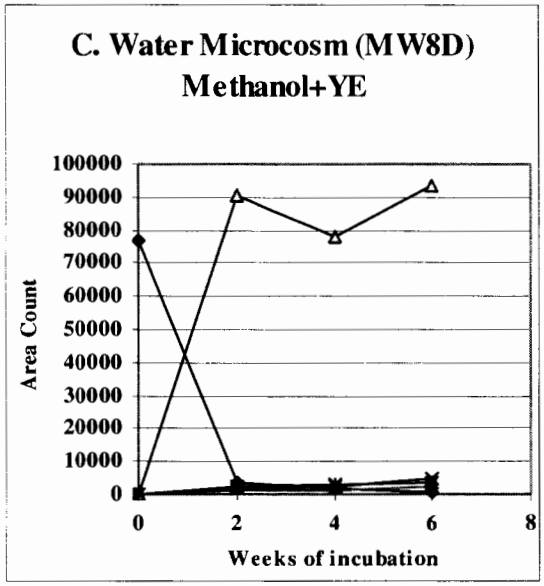
C. Water Microcosm (MW8D)
Methanol+YE
Area Count
100000
90000
80000
70000
60000
50000
40000
30000
20000
10000
0
0
2
4
6
8
Weeks of incubation

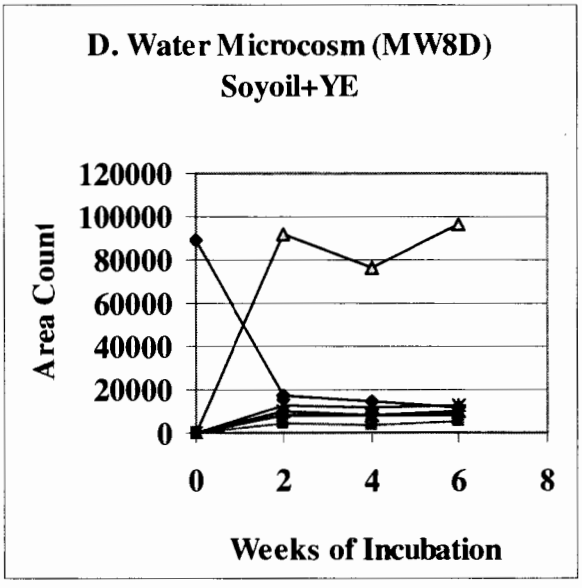
D. Water Microcosm (MW8D)
Soyoil+YE
Area Count
120000
100000
80000
60000
40000
20000
0
0
2
4
6
8
Weeks of Incubation

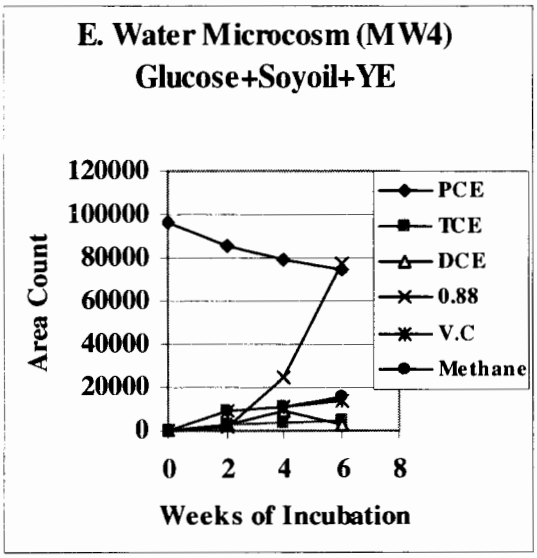

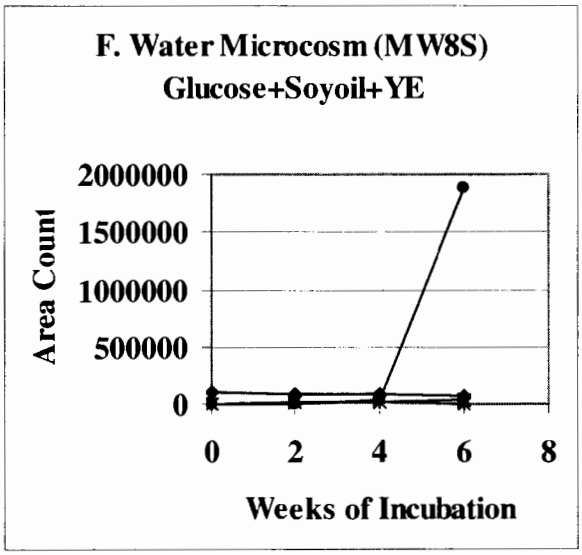

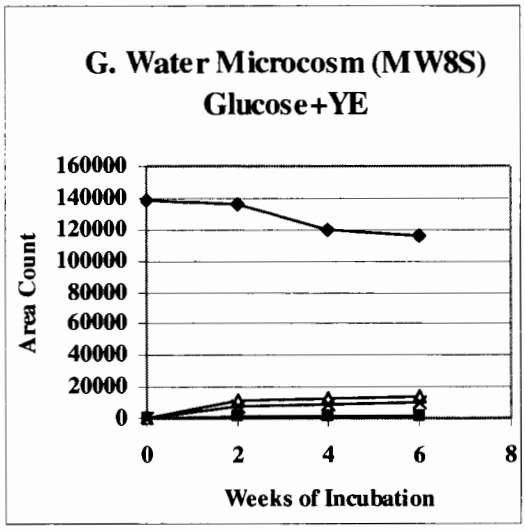

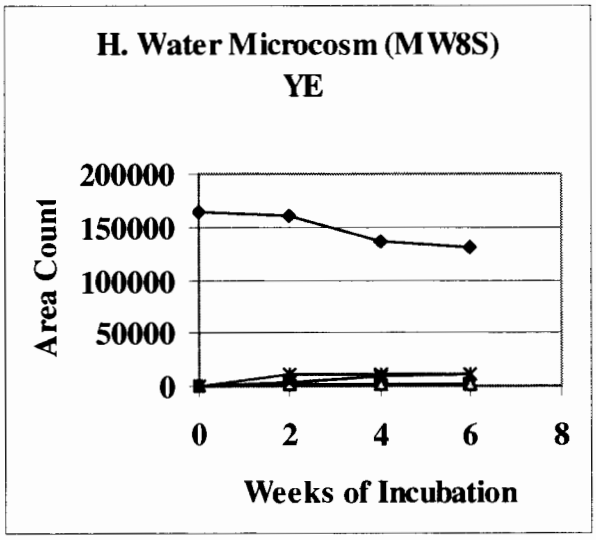

Figure 6 (A-H). Kinetics of PCE transformation to degradation compounds with different treatments for Monitoring Wells 4 and 8; See figure 6E for legend. An unknown compound elutes at 0.88 min in the gas chromatographic analysis.

Sorption of the Malodorant, Tertiary Butyl Mercaptan, to Interior Surfaces

Aruna Suravajjala[1], Stacy L. Hutchinson[2], Larry E. Erickson[3], and Alok Bhandari[1]
Departments of Civil Engineering[1], Biological and Agricultural Engineering[2], and Chemical Engineering[3], Kansas State University, Manhattan, KS 66506

Abstract

Tertiary butyl mercaptan (TBM) is widely used as an odorous tracer in natural gas. It is highly volatile and has a threshold odor of < 8 ppb_v. This study evaluated the sorption-desorption behavior of gaseous TBM with respect to indoor surfaces including carpet materials, wallpapers, and soil. TBM sorption on carpets and wallpapers was near-linear and sorption equilibrium was achieved in about 28 days. Desorption of TBM from solids into the gas phase occurred rapidly initially and was followed by a slow release over 20 h. Sorption-desorption investigations were also performed on granular activated carbon (GAC), a common adsorbent used for the removal of gaseous odors.

Introduction

A variety of indoor surfaces serve as potential sinks for volatile organic compounds that are characterized as indoor air pollutants. TBM (2-methyl-2-propanethiol) is one such compound that is widely used in small proportions as an odorous tracer in natural gas. Natural gas contains a blend of two or three compounds that odorize the gas, and the unpleasant odor resulting from leakages of natural gas is attributed to these malodorants.

Eberhardt et al. (2003) investigated adsorption of TBM to three types of Argentine soils and determined its kinetic and transport parameters. However, a thorough review of the technical literature revealed no published information on the fate of TBM in indoor environments. Therefore this study was conducted with the objective of evaluating sorption-desorption behavior of gaseous TBM on indoor surfaces including carpets, wallpapers and soil. Sorption-desorption investigations were also performed on granular activated carbon.

Materials and Methods

Carpets: Four types of carpets (blended fiber, nylon fiber, woolen fiber, and polyester fiber) were selected for this study. These carpets were obtained from Tri City Carpets, Manhattan, KS. The BF carpet consisted of a mixture of commercial textile materials and is widely used as an all-purpose, heavy-duty office carpeting material. All carpets had a stain-resistant coating and were used with their backing intact.

Wallpapers: Two types of wallpapers (plain vinyl (plain, no texture) and textured vinyl) were used in this study.

Activated Carbon: Activated carbon, 6–14 mesh, was purchased from Fisher Scientific.

Soil: A surface soil with 6.2% soil organic matter content (SOM), collected from a wooded area was selected for this study (Lesan, 2001). The soil was transported to the laboratory, air-dried, crushed, and sieved. The soil was sterilized by alternate autoclaving and incubation at 4°C.

Chemicals: TBM (99.99% purity) was purchased from Sigma Aldrich, St.Louis, MO. Table 1

summarizes various properties of TBM:

Table 1: Properties of TBM[1].

Physical State	Liquid
Appearance	Clear
Color	Colorless
Odor	Gassy odor
Chemical Formula	$C_4H_{10}S$
Chemical Name	2-Methyl-2-propanethiol
Molecular Weight	90.2
Specific Gravity	0.806 at 16°C
Density	6.70 lbs/gal at 16°C
Vapor Pressure	5.8 psia at 16°C
Relative Vapor Density (air = 1)	3.1
Freezing Point	1°C
Boiling Point	63.3 – 65.6 C
Water Solubility	Negligible at 20°C (1470 mg/L after 24 h)
Odor threshold	0.008 ppm
Evaporation Rate	1
Volatility	100%

[1]Reference Source - Natural Gas Odorizing MSDS

TBM Analysis: Analysis of TBM was conducted with a Varian Chrompack CP-3800 gas chromatograph. The injector temperature was 130°C. Chromatographic separation was achieved using a 25 m x 0.53 mm x 0.005 mm Varian Chrompack CP 7656 capillary column. The column was maintained at 100°C for 2 min, after which the oven temperature was ramped at 15°C/min to 150°C. The total run time for each analysis was 5.33 min. Sample detection was performed using a flame ionization detector (FID), maintained at a constant temperature of 250°C. Nitrogen was used as the carrier gas, with hydrogen as detector gas and air as the make up gas. The carrier gas flow in the column was set at 15 mL/min.

Standards: Gas-phase TBM standards were prepared in 160-mL serum bottles. Predetermined volumes of TBM were injected with a Hamilton syringe to obtain the target concentrations of approximately 25, 50, 100, 150, 200, 250, 500, 750, 900, and 1000 mg/m^3. The serum bottles were capped with Teflon-coated gray butyl rubber septa and aluminum crimp caps.

Sorption Experiments: Preliminary experiments were conducted to determine the appropriate mass of the sorbents to be used for sorption experiments. The experiments were conducted with 1.0, 1.5, 2.0, 2.5, and 3.0 g of each sorbent material in 60-mL batch reactors. The initial head-space TBM concentration in all the reactors was 100 mg/m^3. The study was conducted on four types of carpets (office, nylon, woolen, and polyester), two types of vinyl-based wallpapers, surface soil, and activated carbon.

Sorption experiments were conducted in 160 mL serum bottles used as batch reactors. The initial headspace concentrations of TBM chosen for the study were 1, 10, 100, and 1000 mg/m^3.

Three replicate reactors were prepared for each initial concentration and for each sorbent. Triplicate sets of sorbent free controls were also included in the experimental matrix to account for losses due to volatilization or adsorption to reactor components. The contact times chosen for these sorption experiments were 1, 7, 14, 21, 28, and 35 days.

Desorption Experiments: Desorption equilibrium experiments were conducted on reactors with initial headspace TBM concentration of 100 mg/m^3 during sorption experiments. The purpose of these experiments was to determine the time required for TBM to achieve desorption equilibrium. An air exchange system was designed to conduct desorption. Air changes were accomplished using two, 22-gauge syringe needles inserted through the septum as shown in Figure 1.

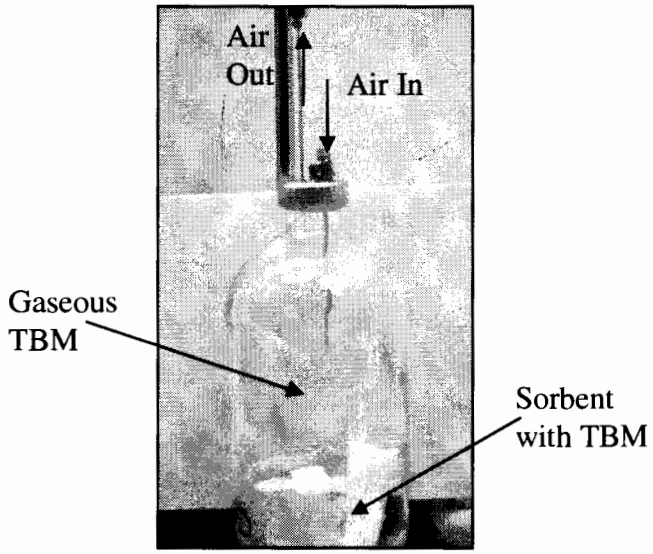

Figure 1: Desorption experimental set-up.

A 25-mL gas-tight syringe was used to introduce air into the reactor. Each air change consisted of replacing 100% of the reactor volume with TBM-free ambient air and resulted in removal of 61% of TBM from the reactor headspace. TBM desorption equilibrium time was determined by subjecting a triplicate set of serum bottle reactors obtained from the sorption experiment (C_o = 100 mg/m^3) to two air changes. This double air change resulted in approximately 85% TBM removal from the headspace. The headspace gas was allowed to exchange with the sorbed gas, and headspace concentrations were measured after 1, 2 3, 4, and 5 h.

Desorption rate experiments were conducted with a second triplicate set of reactors obtained from the sorption experiments (C_o = 1000 mg/m^3). Headspace concentrations in the batch reactors were measured before initiating the desorption rate experiment. Initially, a double air change was performed every hour and the headspace was analyzed for TBM. This was repeated six times. Thereafter, double air change was performed every 2 h for 14 h. Residual solid phase concentrations were estimated using simple mass balances.

Results and Analysis

Sorption: Sorption rate experiments showed that the BF and NF carpets sorbed significantly more TBM than other types of carpets. Hence they were chosen for the sorption experiments. All

wallpapers showed the same amount of sorption after 14 days of contact time, and two types of wallpapers, plain vinyl and textured vinyl, were chosen for further investigation. Based on the results of preliminary studies, 3.0 g of each sorbent were selected for the sorption experiments except for the GAC, for which 50 mg was chosen.

Equilibrium data obtained from sorption experiments were used to estimate the sorption equilibrium constants using the partitioning model

$$q = kC$$

where q is the sorbed concentration in mg/kg, C is the gas-phase concentration in mg/m^3, and k is the equilibrium constant in m^3/kg. Sorption of TBM to carpets and wallpapers was linear and reached equilibrium in approximately 28 days. Sorption to wallpaper was rapid compared to carpets, most of it occurring within 14 days. Sorption of TBM to soil was linear, while that on granular activated carbon was non-linear.

Table 2 gives the phase distribution constants and the mass of TBM sorbed to the various sorbents from a headspace containing 1000 mg/m^3 of TBM.

Table 2: Sorption Equilibrium Constants (Partitioning Model).

Sorbent	Distribution Constant, m^3/kg	TBM Sorbed (C_0 = 1000 ppb$_v$) mg/kg
Blended fiber carpet	0.042	24
Nylon fiber carpet	0.019	16
Plain vinyl wallpaper	0.077	31
Textured vinyl wallpaper	0.078	32
Surface soil	0.056	28
GAC	0.047	25

After exposure to an initial concentration of 1000 mg/m^3 TBM in the gas phase, the amount of solute present on the sorbents after 28 days ranged from 16 to 32 mg/kg. The blended fiber carpet sorbed more TBM (24 mg/kg) than the nylon fiber carpet (16 mg/kg). Sorption to both plain vinyl and textured wallpapers was almost the same, with 31 and 32 mg/kg respectively. However, the wallpapers adsorbed more TBM compared to other sorbents as reflected by their distribution constants of 0.077 and 0.078 respectively. Surface soil and GAC also adsorbed significant amounts of TBM. Although GAC is a highly effective sink for organic compounds, it demonstrated a relatively low distribution constant for TBM, indicating that the GAC used in this study may not necessarily be an effective sorbent for the remediation of indoor environments contaminated with TBM.

Desorption: Desorption equilibria experiments showed that TBM desorption equilibrium was achieved within 2 h for all the sorbents. Desorption of TBM occurred rapidly for the first 6 h and followed first-order kinetics. This was followed by a continued slow release of the solute for over 14 h that appeared to follow zero-order kinetics. The two desorption phases were clearly observed for all the sorbents. Nearly all the sorbed TBM was removed from the two carpets through desorption within 20 h. Table 3 summarizes the experimentally obtained desorption rate constants and % TBM removal for the various sorbents.

Table 3: Desorption Rate Constants.

Sorbent	TBM Sorbed (C_0 = 1000 ppb_v) mg/kg	Desorption Rate Constants		% sorbed TBM removed in 20 h (26 air changes)
		Rapid Phase [a] (d^{-1})	Slow Phase[b] (mg/kg-d)	
Blended fiber carpet	24	2.72	2.49	>99
Nylon fiber carpet	16	2.28	1.64	>99
Plain vinyl wallpaper	31	3.28	0.48	70
Textured vinyl wallpaper	32	4.21	0.16	79
Surface soil	28	0.40	0.71	36
GAC	25	1.80	0.45	88

[a] 0 to 6 h: first order
[b] 6 h to 20 h: zero order

Desorption experiments showed that > 99% of the sorbed TBM was removed from the carpets within 20 h. Between 62 and 67% of the sorbed TBM was removed from the carpets by 12 air changes performed for the first 6 h. The remaining TBM was removed by the 14 air changes conducted over 14 h. Nearly 70 to 79% of the total adsorbed TBM was removed from the wallpapers after 26 air exchanges conducted over a period of 20 h, of which 71% of the residual TBM was removed during the rapid phase. Desorption rate of the sorbed TBM was significantly lower for the soil as compared to those of carpets and wallpapers. Even after 20 h, most of the adsorbed TBM remained on the soil. Only 25% of the sorbed TBM was released from the soil during rapid phase, while an additional 11% of the sorbed malodorant desorbed during the slow phase. About 88% of the sorbed TBM removal was achieved for GAC, with the majority of it occurring in the first 6 h.

Conclusions

Sorption-desorption of TBM was investigated to determine its environmental fate in the indoor environment. TBM sorption to the selected indoor materials required 28 days to reach equilibrium. The concentration of TBM present in the sorbent materials ranged between 16 and 32 mg/kg (C_0 = 1000 ppb_v) after 28 days. Desorption equilibrium of TBM was reached within 2 h for all the selected sorbents. Nearly all the TBM present in the carpets was removed in 20 h. Based on the desorption studies conducted, it is estimated that the time required to remove TBM odor below the odor threshold of 8 ppb_v from indoor surfaces may be as short as 24 h. GAC did not appear to be an effective sorbent for TBM removal from indoor air.

Acknowledgments

- This research was partially supported by the Department of Navy, Naval Surface Warfare Center, Dahlgren Laboratory. The content of the information does not necessarily reflect the position or the policy of the government, and no official endorsement should be inferred.
- Tri City Carpets and Sherwin William Paints, Manhattan, KS, for providing the carpets and the wallpapers.

References

1. Eberhardt, A., Lopez, E., Bucala, V., and Damiani, D.E.; "Tertiary Butyl Mercaptan Adsorption in Soils. Determination of Kinetic Parameters from Experimental Data", *Intl. J. Chem. Reactor Eng.*, 1, A42, 2003.

2. Lesan, H.M; "Aging Effects on Atrizine Adsorption, Desorption and Distribution Among Organic Fractions in Two Hillsdale Basin (Kansas) Surface Soils", *MS Thesis*, Kansas State University, 2001.
3. Natural Gas Odorizing MSDS Number – M35759, Natural Gas Odorizing, 3601 Decker Drive, P.O. Box 1429, Baytown, TX 77522-1429, 2003.http://www.oxychem.com/products/msds/m35759.pdf